Differential Regulation of Core Transition Zone and Centriole Components Contributes to Ciliary Base Diversity

Swadhin Chandra Jana[1, †], Susana Mendonça[1], Pedro Machado[1, 5], Sascha Werner[1], Jaqueline Rocha[1, 6], António Pereira[2, 3], Helder Maiato[2, 3, 4], Mónica Bettencourt-Dias[1, †]

Affiliations

1- Instituto Gulbenkian de Ciência, Rua da Quinta Grande, nº 6, 2780-156 Oeiras, Portugal.
2- Instituto de Biologia Molecular e Celular, Universidade do Porto, Porto, Portugal.
3- Instituto de Investigação e Inovação em Saúde – i3S, Universidade do Porto, Porto, Portugal.
4- Department of Biomedicine, Faculdade de Medicina, Universidade do Porto, Porto, Portugal.
5- Present address: European Molecular Biology Laboratory, Electron Microscopy Core Facility, 69117 Heidelberg, Germany.
6- Present address: Centro de Biotecnologia e Química Fina, Universidade Católica Portuguesa/Porto, Portugal.

†- e-Mail address for correspondence

Swadhin Chandra Jana - swadhin1cal@gmail.com

Mónica Bettencourt-Dias - mdias@igc.gulbenkian.pt

Abstract

Cilia are evolutionarily conserved protrusions with many sensory and motility-related functions. The ciliary base, composed of the basal body and transition zone, is critical for the assembly and function of cilia, but it is not known how it contributes to cilia diversity. To investigate the extent and causes of ciliary base variation we generated a high-resolution structural and biochemical atlas of the ciliary base of four functionally distinct neuronal and sperm cilia types within an organism, *Drosophila melanogaster*. We uncovered both a common scaffold and diverse structures associated with different localisation of 15 evolutionarily conserved components. Furthermore, we show CEP290/NPHP6 forms highly diverse links in distinct transition zones. We also uncover that the cartwheel components, SAS6 and ANA2/STIL, have a novel role in basal body elongation, which depends on BLD10/CEP135. Differential expression of these cartwheel components contributes to diversity in basal body length. Our results offer a plausible explanation to how mutations in conserved ciliary base components lead to diseases in specific tissues.

Introduction

Cilia are microtubule (MT)-based cellular protrusions, which are critical for cellular motility, fluid flow and sensing [1, 2]. These organelles are present in all branches of the eukaryotic tree of life. A large group of molecules are needed for ciliary assembly and function, and their evolutionary conservation has been highlighted by several comparative genomic studies (reviewed in [3]).

In animals, ciliary functions relate to a plethora of developmental and physiological roles, such as defining left-right asymmetry in the body plan, olfaction, hearing and fertility, amongst many others [1]. The wide range of ciliary functions present in animals, contradicts the perceived evolutionary conservation of ciliary components, raising interest about possible diversification mechanisms. The cilium is roughly composed of two distinct regions: a base attached to the membrane, henceforth called “ciliary base”, and a “ciliary shaft” protruding from the base.

Most studies investigating ciliary diversity have focused on variations in the ciliary shaft, in particular its membrane composition and MT-based skeleton, i.e. the axoneme [4-7]. For example, while immotile cilia show nine radially arranged MT doublets (‘9 + 0’), motile cilia additionally have dynein arms on the MT doublets, which are often associated with a central pair of MT singlets (‘9 + 2’), both adaptations for ciliary movement (reviewed in [1, 2]). Differential expression of motility-associated genes, such as those coding for the dynein arms, contributes to the observed axoneme diversity [8, 9].

The ciliary base is composed of the basal body, a transition zone found between the basal body and the ciliary shaft, and accessory structures that link the basal body with the cytoskeleton and membranes [10, 11]. In most animal ciliated cells, basal bodies arise from the conversion of an evolutionarily conserved structure, the centriole. The centriole is a cylinder, consisting of nine radially symmetric MT triplets surrounding a lumen. In its proximal part, there is a cartwheel, a structure composed of stacks of nine-fold symmetric spokes that connect to the MT triplets, imprinting the conserved nine-fold symmetry of the centriole [2, 12]. Centrioles are normally found in a pair, within the centrosome, the major MT organising centre in cycling

cells. They are coated with the pericentriolar material (PCM), which allows them to nucleate MTs. Centrioles can convert to basal bodies and the eldest of the centrioles within the centrosome templates the transition zone and accessory structures, forming the ciliary base [13]. The ciliary base nucleates the formation of the ciliary shaft (axoneme and membrane), provides stability to the cilium, and mediates trafficking of components in and out of the cilium, controlling the composition and function of the organelle [14-16]. Given the described structural and biochemical conservation of the centriole and the transition zone in different eukaryotic species, the ciliary base is perceived to vary less in its structure than the ciliary shaft[6, 10, 11].

Recent evidence suggests that the ciliary base might be more diverse than it is currently appreciated. Mutations in evolutionarily conserved genes encoding for components of the ciliary base, such as OFD1, CEP290/NPHP6 and MKS, display cilia type-specific phenotypes, such as nephronophthisis (mainly affect kidney primary cilia), retinal degeneration (affect photoreceptor cilia), or sterility (affect primarily sperm flagella) (reviewed in [1, 17]). This evidence indicates that differences in the ciliary base structure, its composition and function contribute to cilia diversification in different tissues. However, a careful comparative analysis of the ultra-structure and composition of different types of ciliary bases within an organism was never conducted.

Here we investigate whether and how the ciliary base contributes to cilia diversification. To thoroughly assess the extent and causes of variation, we use an organism with diverse cilia types. *Drosophila melanogaster* is an ideal system as it relies on structurally distinct ciliated cells for many critical functions, such as olfaction, coordination, hearing, negative-geotaxis walking and fertility [18, 19]. Though many studies have investigated the assembly of ciliary bases of *Drosophila* neurons and sperm cells ([20-23] and reviewed in [24]), a high resolution analysis that compares those cilia is missing. This is critical, so that different cilia and components can be compared across different tissues, and causes of variation can be identified. Here we comprehensively compare the ciliary bases of four distinct *Drosophila* ciliated cell types, selected to represent different sensory and motility functions: immotile sensory cilia in olfactory neurons, motile sensory cilia in auditory neurons, immotile cilia in spermatocytes (sperm

precursor cells), and a long motile cilia in differentiating/elongating spermatids ([23, 25, 26], Figure S1A-D). Furthermore, the two types of sperm cells were chosen to represent different time points in the development of the same ciliary base, as it is the same base that nucleates the immotile cilia in the spermatocytes and later, after meiosis, motile cilia in the elongating spermatids (Figure S1E). Using high-resolution microscopy-based techniques, we found that ciliary bases show a common scaffold that is complemented by extensive structural and biochemical variation. By investigating and manipulating ciliary-base gene expression, we discovered that evolutionarily conserved components of the ciliary base are differentially present and/or localised to regulate the formation of diverse ciliary bases. Our work provides a framework to study how diverse ciliary functions are structurally encoded, as well as to better understand the genesis of tissue-specific ciliary diseases.

Results

To test whether the ciliary base is diverse, we built 3D structural and molecular models of the ciliary base of four different cilia types in adult *Drosophila*. Given that the sizes of those structures are close to the resolution limit of conventional light microscopy, we used a combination of the best high-resolution imaging tools available to date, such as transmission electron micrography (TEM) of serial sections, electron tomography (ET) and 3D-structured-illumination micrography (3D-SIM). While TEM of serial thin sections (~70-100 nm) helped us to develop a course 3D model of the ultrastructure of a region, electron tomography of the thicker sections (~120-150 nm) was used to model subtle features that generally remain buried within a section used for conventional TEM. The results obtained with those two tools were combined to model the nano-scale 3D ultrastructure of the ciliary base. We then used 3D-SIM to map molecules to the ultrastructure and assemble the nano-scale 3D molecular map of the ciliary base.

Micron-scale organisational map of the ciliary base shows diverse global organisation

We first focused on assembling a micron-scale organisational map of the ciliary base and its context in the cell, such as the number of basal bodies per cilium, basal bodies´ orientation and their size, accessory structures and the PCM coating of the basal bodies.

Organisation of basal bodies in different cell types

We used both TEM and ET of longitudinal sections of ciliary bases, and 3D-SIM of a common basal body marker, PACT (the C-terminal domain of pericentrin-like protein (PLP)) [27] to estimate the basal body size (length and diameter) independently, and obtained concordant results using these different imaging tools (Figure 1A-D, S2-4). We observed that the number, length and orientation of basal bodies are different in distinct cell types. In neurons, two small differently sized basal bodies (~120-260 nm) are linearly arranged at the ciliary base (Figure 1A, B and S2), and only the longer one (~200-260 nm), called distal basal body, is adjacent to the sensory cilium (Movie M1, 2). In contrast, in spermatocytes, two very long, equally sized basal bodies (~1300-1400 nm) are arranged orthogonally, an organisation similar to a centrosome in cycling cells. Both of the basal bodies grow cilia (Figure 1C, D; [20, 21, 28]). Later on, the same spermatocyte undergoes meiosis, and each daughter cell (spermatid) inherits one basal body that forms a flagellum (Figure 1D, E; [21, 29]).

Accessory structures and coating of the basal body

We then investigated the presence, morphology and composition of accessory structures and PCM in the different ciliary bases. Electron dense structures, such as rootlet, basal foot and connections to the plasma membrane, were considered accessory structures. Rootlets are composed of rootletin, and they are thought to link the basal bodies to other parts of the cell, providing stability to the cilium, and being essential for neuronal cilia function [30]. We observed that rootlets are distinct in different cilia: they link the two basal bodies in the different types of neurons, showing different features, such as length, striation and localisation (Figure 1A*i,ii*, B*i,ii* and S2A-C), and they are absent from both sperm cilia types (Figure 1C, D and S2C). In olfactory neurons, the short rootlet (~1-2 µm) encapsulates the proximal basal body and attaches to the wall of the distal basal body (Figure 1A*i,ii*, S2A and Movie M1). In auditory

neurons, the very long striated rootlet (~20-25 µm, length estimated from [30]) encapsulates the proximal basal body and connects to the inner wall and/or the lumen of the distal basal body (Figure 1B*i,ii*, S2B and Movie M2). Moreover, in the latter cell type, the rootlet is also connected to the cell membrane by electron-dense structures ([18] and Movie M2). These accessory structures may provide support for the mechanical stress that auditory cilia in the second antennal segment experience [26]. Interestingly, variations in length and striation of rootlets were also found in *C. elegans* and those long, striated rootlets were also proposed to provide support the mechanical stress that mechanosensory neurons experience [31]. Note that we could not find any basal foot (Figure 1 and S2), an accessory structure that arranges perpendicularly to the distal basal body and connects the basal body to cytoplasmic MTs, often observed in multiciliated cell types in other animals [32].

We then investigated basal body coating. Remarkably, similarly to centrioles in cycling cells, all basal bodies from different cilia types are surrounded by both electron dense material and cytoplasmic MTs (Figure 1A*i*-D*i* and S2A-C). Therefore, we examined whether basal bodies are embedded in the same PCM proteins that normally surround centrioles and associate to the electron-density around them. We focused on three critical conserved components, PLP/Pericentrin (PLP is a *Drosophila* orthologue of human Pericentrin), SPD2/CEP192 and γ-tubulin. PLP and SPD2 are required for PCM assembly and γ-tubulin recruitment, while the latter is required for MT nucleation [27, 33-35]. We observed that the PCM around the basal bodies is differentially organized in distinct cilia types: γ-tubulin and PLP localise to all basal bodies, while SPD2 is found around most basal bodies, except in the spermatid (Figure 1A*iii*-D*iii*, E and S3, 4). Intriguingly, distinct PCM components localise to different regions around the basal bodies and to different accessory structures (Figure 1E and S3, 4). Moreover, the data obtained from spermatocyte and spermatid, two stages of development of the sperm cell, show that the localisation of those components changes during sperm development and maturation (Figure 1C-E). Localisation of PCM and centriole components is then lost from the basal body of mature spermatids, as described before [36, 37].

To summarise, our analysis shows that all ciliary bases are composed of basal bodies that nucleate cilia, and are embedded in several PCM components (Figure 1 and S2-4). The presence of several PCM components in different basal body subdomains is intriguing, as components such as PLP and SPD2 are mainly known to be part of the centrosome in cycling cells to increase its MT-nucleating capacity. Though the importance of the localisation of PCM components in different basal body subdomains in different ciliated vertebrate cells is yet to be studied, some PCM components, such as Pericentrin and γ-tubulin, were previously found at the base of many ciliated cells in other organisms [38-41]. It is possible that these basal bodies are also microtubule organising centres (MTOC) as we observe cytoplasmic MTs surrounding the fly basal bodies (Figure S2C), and cytoplasmic MTs have been observed around basal bodies in other species [32, 42]. However, further investigation is needed to know whether those MTOCs are active and what is their role in cilia and cell homeostasis.

In conclusion, we showed distinct ciliary bases in the fly display many differences including: the number of basal bodies associated with each cilium, basal body length, their orientation, accessory structures and composition of PCM coating (summarised in Figure 8A).

Nano-scale organisational map of the ciliary base shows remarkable diversity

To identify mechanisms of ciliary base diversification, we then investigated the ultrastructure and composition of the basal bodies and the transition zone in more detail.

Basal body structure and composition vary between cell types

Our TEM and ET analyses of the basal body cross-sections show that all basal bodies are 9-fold symmetric (Figure 2A*i,ii*-D*i,ii*). As previously described, sperm cells display canonical basal bodies, which show both a cartwheel and MT triplets (Figure 1C*i,ii*, D*i,ii* and 2C*i,ii*, D*i,ii* ; [20]). In contrast, all neuronal basal bodies have no cartwheel and most show doublets instead of triplets (Figure 2A*i,ii*, B*i,ii* and S2D, E), with the proximal basal body of auditory neurons being composed of a mixture of nine MT singlets and doublets (Figure 2B*i,ii*, S2E and Movie M3-6). The number of singlets and the relative position of singlets and doublets in the proximal basal body varies between individual auditory neurons. The lumen of the spermatid basal body shows a MT singlet (Figure 1D*i,ii* and 2D*i,ii*), previously described to template the central pair

of MTs that is needed for flagellar motility [20]. Vesicles and MT singlets are also occasionally found in the lumen of basal bodies and between the proximal and distal basal bodies of olfactory neurons (Figure S2A and Movie M1), but were absent in our observations of auditory neuron basal bodies (for details see Figure S2A-B, Movie M2 and their legends). In summary, while all basal bodies show the conserved nine-fold symmetry in their MT arrangement, they can differ in many distinct features, including types of MTs the basal bodies are made of (e.g., singlet, doublet or triplet), presence of cartwheel, and presence of central MT singlets and vesicles in the basal body lumen.

To unravel the molecular mechanisms associated with the structural differences above described, we investigated the localisation of core conserved centriole components known to be part of those structures in many different eukaryotes: two components of the centriole wall (ANA1/CEP295 and SAS4/CENPJ), two components of the cartwheel (SAS6 and ANA2/STIL), and a linker between both structures (BLD10/CEP135) [37, 43, 44]. While all basal bodies show ANA1 along their walls and BLD10 in the lumen, SAS4 localises only in the proximal part of the basal body (ppBB) in sperm cells and protrudes out from the basal body wall onto the rootlet in both types of neurons (Figure 2A*iii*-D*iii*, E and S3, 4). Both cartwheel components, SAS6 and ANA2, are only present in sperm cells (Figure 2A*iii*-D*iii*), consistent with the presence of cartwheel observed by TEM only in those cells (Figure 1C*i,ii*, D*i,ii*).

Our data shows that all basal bodies present a nine-fold symmetric barrel-like structure, labelled by ANA1 and BLD10 (Figure 2A*iii*-D*iii*, E). However, several characteristics of the barrel change, including the presence of cartwheel and the types of MTs they are made of (e.g., singlet, doublet or triplet) (Figure 2A*i,ii*-D*i,ii*). Interestingly, also in human cycling cells, the cartwheel disappears from the centrioles at the end of mitosis, suggesting that basal bodies in a primary ciliated cell would also have no cartwheel [45]. The existence of the cartwheel correlates with the differential presence of the core, evolutionarily conserved proteins, SAS6 and ANA2, suggesting cell-type specific regulation (Figure 2A*i,iii*-D*i,iii*, E and summarised in Figure 8A).

Transition fibres, Transition zone and their composition in different cilia types

In a canonical eukaryotic cilium, the region between the basal body and axoneme consists of two structures: transition fibres and transition zone. The transition fibre, a nine-fold symmetric structure, tethers the distal tip of the basal body to the ciliary membrane [11]. Although, this structure is found in many vertebrate ciliated cells (reviewed in [10]), Doroquez *et. al.* could not find similar structures in *C. elegans* sensory cilia [31]. This structure is analogous to another nine-fold symmetric structure, the distal appendage, mostly found in mother centrioles of cycling cells [12]. The canonical eukaryotic transition zone consists of nine radially symmetric MT doublets and linkers that connect each doublet to the ciliary membrane. The later structure is called Y-linker, as its morphology in TEM is similar to a "Y". This region is thought to work as a gate that controls entry of molecules into the ciliary shaft (reviewed in [10, 11]). Therefore, to investigate whether the region between basal body and axoneme varies between different cell types in *Drosophila*, we examined its structure, including its length, the types of MTs the transition zone is made of (e.g., singlet, doublet or triplet), electron-dense regions in between adjacent MT doublets, and the connection between MTs and the ciliary membrane (Figure 3). Although the transition zone is conventionally defined to be the region between the basal body and the ciliary shaft, many transition zone components move to the tip of the flagellum in *Drosophila* spermatids [21, 29]. Here we focused on the area between the basal body and the axoneme in all cilia to allow for the comparison of the same region in different ciliary bases.

Given that mother centrioles in cycling cells do not have distal appendages in *Drosophila* (reviewed in [24, 46]), we investigated whether transition fibres, the analogous structure for basal bodies, are found in the ciliated cells. Unexpectedly, a detailed cross section analysis showed that all types of cilia, except the ones in elongating spermatids, have obvious transition fibres. These fibres connect the MT doublets or triplets to the ciliary membrane in neurons and spermatocytes, respectively (Figure 3A*i*-C*i* and S5A*ii*-D*ii*: the fibres are marked by white arrowheads). Transition fibres might be absent in the spermatid or alternatively the highly electron-dense materials around the basal body hinder the visualisation of any existing transition fibre-like structures (Figure 3D*i*).

We observed that the length of the transition zone varies greatly between different types of cells: the longest is found in auditory neurons (~750-1000 nm), while it is half of that size in both olfactory neurons (~450 nm) and spermatocytes (~500 nm) (Figure S5A*i*-D*i*). Furthermore, we observed that all transition zones are made of nine radially symmetric MT doublets and show electron dense structures in between adjacent MT doublets (here called "MT-MT linkers") and in between MTs and the ciliary membrane (here called "MT-membrane linkers": marked by arrows) (Figure 3A*i,ii*, B*i,ii*, C*i,* D*i*; to compare the different linkers see images in the insets of A*i*-D*i* and their corresponding schemes).

Linkers exhibit distinct features, such as their shape and the structure they connect to (Figure 3A*i,ii*, B*i,ii*, C*i*, D*i* and S5A*ii*-D*ii*). The shape of MT-MT linkers is different in distinct ciliary bases (Figure 3A*i*-D*i*). Moreover, linkers can also vary along the length of the transition zone in auditory neurons (Figure S5B*ii*). In neurons, we observed that MT-membrane linkers are similar to the Y-linkers previously described in other eukaryotes, such as *Chlamydomonas*, *C. elegans* and mouse [47-49]. Surprisingly, we observed that MT-membrane linkers originate from different structures in distinct cilia types. While in olfactory neurons they arise from the electron density around the A- tubule of the MT doublet, in auditory neurons they arise from the electron density around the B- tubule (Figure 3 A*i,ii*, B*i,ii* and Movie M7, 8). In sperm cells, the MT-membrane linker is different. In spermatocytes it is similar to a hook-like structure connected to the membrane by a light electron dense structure (Figure 3C*i*); later, in the elongating spermatid, the same hook is no longer connected to the membrane (Figure 3D*i*).

In summary, we observed that transition fibres are visible in all ciliated cell types, except in the spermatid, and that the transition zone is always composed of MT doublets and linkers (MT-MT and MT-membrane). However, the transition zones vary in their length, and the linker structures are remarkably different amongst different cell types (Figure 3A-D and S5).

We next investigated the origins of the diversity observed in the transition zone, focusing on previously identified and evolutionarily conserved components of those structures: the distal part of the centriole (UNC/OFD1), transition fibres/ distal appendages (Chibby), and other linker structures (MKS1, B9D1 and CEP290) [28, 29, 50].

We observed that all transition zones, with exception of the spermatid, showed all five components (Figure 3A*iii,* B*iii,* C*ii,* D*ii*, E and S6). However, the localisation of distinct components differed within each transition zone, and when comparing different types of cilia (Figure 3E). For example, while CEP290 localises close to the MT outer wall along most transition zones, all other components localise closer to the ciliary membranes, suggesting an existence of at least two sub-domains within the cross section of a transition zone (Figure 3E and S6A-C). Moreover, in neurons the transition zone has at least two longitudinal sub-domains: the proximal part is composed of all five components, while the distal one is composed of CEP290 (Figure 3A*iii*, *Biii,* E and S6A, B). Though all five components localise to the tip of the growing axoneme in spermatids [29], only UNC localises to the distal part of the basal body and the region between the basal body and axoneme (Figure 3D*ii*, E).

In summary, we found transition fibres linking the basal body to the membrane in all cilia types with the exception of spermatids, and transition zones with doublets and linkers in all cilia types. However, we observed remarkable variability in transition zone length and characteristics of linker structures (MT-MT and MT-membrane linkers) in between different cilia types (Figure 3A*i,ii*, B*i,ii*, C*i*, D*i* and S5A*ii*-D*ii*). Our results suggest that core transition zone proteins, together with other unidentified transition zone components, create multiple sub-domains within each type of transition zone (Figure 3E, summarised in Figure 8A) and thereby generate functionally diverse ciliary gates.

Multiple mechanisms of ciliary base diversification

Our data shows that the ciliary base is composed by a common structural and biochemical scaffold, complemented by a set of variable characteristics, specific to each cell type. To investigate the origin of such variability, we focused on three critical ciliary base structures with variable behaviour: the linkers in the transition zone, which show distinct electron-dense morphologies (Figure 3 and 8A), the cartwheel in the basal body, which shows a binary pattern (presence or absence) and the length of the basal body that varies between distinct cilia types (Figure 1, 2 and 8A).

CEP290 is required to form diverse linker structures in the transition zone of neurons and sperm

We first investigated the underlying mechanism for the assembly of diverse linkers found in the transition zone. We focused on linkers in the regions: i) between the adjacent MT doublets (MT-MT linkers) and ii) between the MT doublets and membranes (MT-membrane linkers). MT-membrane linker structures were described in several organisms, where they were called Y-linkers due to their shape, and given their ubiquitous presence are thus thought to be evolutionary conserved [10, 11, 51]. Although the disruption of several transition zone components affects Y-linkers, CEP290 is the only protein known to be implicated in Y-linkers formation [47, 52, 53]. In *Drosophila*, the *Cep290* gene produces only one protein isoform and the protein localises to transition zones of most cilia types, being required for cilia assembly (Figure 3E; [29]), suggesting it might be a core component of most transition zones. However, recently, CEP290 was also: i) implicated in central ring formation in the *C. elegans* transition zone [54], ii) found in the lumen of the proximal part of the transition zone in the primary cilia of human retinal pigmented epithelial (hRPE) cells [55] and iii) found to occupy an inner region of the transition zone overlapping with axonemal MTs [56, 57] in *Drosophila*, upon using C-terminally tagged CEP290. Altogether this evidence suggests CEP290 localises differently in different organisms. Therefore, we investigated the localization of CEP290 in different ciliated cells using tags labelling different termini, and asked whether CEP290 could be involved in forming the different types of MT-MT and MT-membrane links observed in the different cilia types.

To better investigate the localisation of CEP290, we first studied the localisation of both its N- and C- terminus, using GFP-tagged proteins to both termini. Using 3D-SIM we could resolve that in all cilia types, where CEP290 localises to the transition zone, the protein orients along the radius of the transition zone: C- terminus preferentially orienting towards the MTs, while the N-terminus orienting towards the ciliary membrane (Figure 4A, D, G and S7A). This orientation might also be conserved in human cells and mouse as the C- and N- terminal regions of CEP290 were recently shown to bind to the MTs and the membrane, respectively [52, 58].

To further map CEP290 localisation on to the transition zone linkers and understand the radial symmetry of its localisation, we investigated the localisation of differently GFP-tagged CEP290 on the cross-section of transition zones using Stimulated emission depletion (STED) microscopy, which is used to achieve a resolution of ~35 nm in biological samples [59]. We found that CEP290::GFP forms a small ring, suggesting its C-terminus localises to the MT-MT links and the inner tip of the MT-membrane linkers. On the other hand, GFP::CEP290 is radially arranged with 8 or 9 foci in olfactory cilia (Figure 4Av and S7C). The distance between adjacent foci is 99±23 nm suggesting these foci are 9-fold radially symmetric and this terminus localises to the outer tip of the MT-membrane linkers (Figure 4Avi-iv and S7C). Furthermore, in auditory neurons and spermatocytes, the inter-distances between adjacent GFP::CEP290 foci were 100±24 nm and 90±23 nm (Figure S7C) respectively, suggesting the protein also localises in a 9-fold symmetric fashion in those cilia too. Altogether, our data suggests CEP290 orientation pattern is generic in different types of cilia in the fly and is required for the assembly of diverse linkers, such as MT-MT linkers, Y-linkers and hooks, in different ciliated cell types.

To further test this hypothesis we first removed CEP290 using a null mutant [29]. Similar to the CEP290 knockout mouse [52], the fly mutant fails to form a transition zone in neurons, as the distal basal body does not dock (Figure 4B). Therefore, we could not use this mutant to study the role of CEP290 in the assembly of linkers in the transition zone. We then used RNAi to only partially deplete CEP290 (*CEP290RNAi*^{1}: a hairpin was expressed using *Gal4*^{neur} driver, see Table S3 for description of genotypes) in the growing sensory neurons. These flies showed similar behavioural defects to the *Cep290*^{mutant}, as they had impaired ability to both smell (Figure S8A: the defect in ability to smell is similar to a null mutant of Orco, a co-receptor that is essential for fly olfaction [60]), and to walk in a negative-geotaxis assay (Figure S8B). Though most basal bodies dock to the membrane in *CEP290RNAi*^{1} flies, they form defective cilia (for olfactory cilia see Figure S8C, and for auditory cilia see Figure S8D) allowing us to study the linkers in detail. Using TEM we could observe abnormal MT-MT and MT-membrane (Y-) linkers (Figure 4B, E: middle panel). While the defect in the MT-MT linkers is more severe in auditory neurons, the MT-membrane linkers are significantly affected in all neurons (Figure

4B, E). Furthermore, the defect in MT-membrane linkers affects the distance between the MT doublets and the membrane: the MT-membrane distance is reduced in olfactory neurons (Figure 4B-C, see Figure S7B for detailed description of methods to measure the MT-membrane distance), while in auditory neurons the MT doublet-membrane distance becomes variable (Figure 4E-F). These results suggest CEP290 is required to form MT-MT linkers and Y-linkers in all neurons.

We then investigated the role of CEP290 in the formation of the differently shaped linkers (MT-MT and MT-membrane) of the sperm transition zone. In the *Cep290*^{mutant}, unlike in the neurons, the spermatocyte basal body docks to the cell membrane and grows a small defective transition zone, associated with longer basal bodies [29]. In those flies, the MT-MT linkers and the connection between hooks and the membrane are affected, increasing the distance between the hook and membrane (Figure 4H, I). Similar defects are also found in the *CEP290RNAi*^{2} flies (a hairpin was expressed using *Gal4*^{hsp83} driver): we observed lower fertility (Figure S8E*i*, S9A), and similarly to the *Cep290*^{mutant} we observed longer basal bodies (Figure S8E*ii,iii* and S9A), defective axonemes (Figure S8E*iv*) and abnormal linkers (Figure 4H,I: see middle panel). Altogether, our data suggest CEP290 is not only involved in Y-link formation, as previously shown in other organisms [47, 52, 53], but it is also required to establish diverse MT-MT linkers, and hook-membrane linkers, but not to form the sperm hook.

In summary, we observed that CEP290, a conserved core component of the ciliary transition zone, is required to form distinct MT-MT and MT-membrane linkers, which are 9-fold symmetric, in different transition zones, establishing morphologically diverse MT-MT spacing and MT-membrane links in different cell types (for summary see Figure 8B).

SAS6 and ANA2, two core cartwheel components, are required for sperm basal body elongation

As all basal bodies result from the conversion of centrioles, we considered the possibilities that either centrioles are different in different tissues or they diverge only upon conversion to basal body. Therefore, we asked whether the cartwheel and its components, such as SAS6, are already differentially present upon centriole birth in ciliated cell types, or only lost after

centriole to basal body conversion. We first investigated neurons, where we saw the absence of the cartwheel. We thus studied the localisation of the cartwheel´s main structural component, SAS6, during the development of both types of neurons. We found that SAS6 is present during centriole to basal body conversion and in the early phase of ciliogenesis in both basal bodies (Figure 5A, at 24 hrs after pupae formation(APF)), only disappearing later (Figure 5A, for example at 48 hrs APF). Furthermore, we observed the cartwheel is present in the centriole of the differentiating olfactory neurons at 24 hr APF (Figure S10A). These observations suggest that centrioles are born both with a cartwheel and its structural component, SAS6. Therefore, SAS6 might be essential for centriole assembly, but not required later, for basal body function in the ciliated neurons. To test this possibility, we developed precise tools in the neurons to deplete SAS6 before (*SAS6* ^{mutant}) and after centriole assembly (*SAS6RNAi*^{1}: a hairpin expressed using *Gal4*^{Cha19b} driver, see or description of genotypes) and studied its consequences in the olfactory and auditory cilia (Figure 5B*i* and S10B).

SAS6 ^{mutant} fails to form centrioles, hence, no cilium is formed (for fluorescent micrograph see Figure S10B and for TEM see Figure 5B*ii*: middle panel). Furthermore, we wanted to test the functional consequences of this cellular phenotype. As the auditory cilia are also involved in negative-geotaxis walking of the fly [50], we measured the negative-geotaxis walking ability of adult flies (Figure 5B*iii*). Mutant flies were uncoordinated, confirming the role of SAS6 in neuronal centriole biogenesis (Figure 5B*iv,v*). When we removed SAS6 after centriole biogenesis (*SAS6RNAi*^{1}), at a stage when centrioles have converted to basal bodies, we observed that the neuronal basal body and cilia are normal (for fluorescent micrograph see Figure S10B and for TEM see Figure 5B*ii*: right panel). Moreover, the walking behaviour of *SAS6RNAi*^{1} flies was also unaffected (Figure 5B*iv,v*). Therefore, we conclude that SAS6 is only necessary for neuronal centriole assembly, but does not play a role in neuronal basal body and cilia function.

Both cartwheel and its component SAS6 are maintained in spermatocytes, as well as in the early elongating spermatid (Figure 2E and 6A). We asked whether SAS6 could have any other

function beyond its well characterised function in the beginning of centriole assembly. Surprisingly, we observed that SAS6 is partially (~60%) dynamic even after centriole biogenesis, at the spermatocyte basal body, suggesting the centriolar fraction of SAS6 is exchanged with its cytoplasmic pool (Figure 6B). These observations suggest that SAS6 has a post centriole assembly function in this particularly long basal body. To test this hypothesis, we depleted SAS6 before (*SAS6* ^{mutant} and *SAS6RNAi*^{2}: a hairpin was expressed using *Gal4*^{bam} driver) and after (*SAS6RNAi*^{3}: same hairpin was expressed using *Gal4*^{hsp83} driver) spermatocyte centriole assembly and studied its consequences in basal body structure, as well as in the basal body and cilium function in fertility (Figure 6C, S9B and S11). We found that depletion of SAS6 before centriole assembly reduces centriole number and fertility as expected (Figure 6C*i,ii,iii*, S11, and [61]). The knockdown of SAS6 (*SAS6RNAi*^{3}) after centriole biogenesis does not affect centriole number, but remarkably affects its maturation to basal body, reducing both its length and male fertility (Figure 6C*i-iv* and S11).

Our work revealed a new function for SAS6 in basal body elongation. During centriole biogenesis, SAS6 is normally recruited by ANA2/STIL in cultured cells [44, 62], we thus asked whether this novel function of SAS6 is also regulated by ANA2. We observed that ANA2 depletion after centriole biogenesis (*ANA2RNAi*^{1}: a hairpin was expressed using *Gal4*^{hsp83} driver), did not reduce centriole number (Figure 6C*i-iii*), but reduced SAS6 localisation to the basal body and basal body length (Figure 6C*iv-vi*). This phenotype was associated with reduced male fertility (Figure S9C, S11).

We next wanted to further understand this novel function of SAS6 and ANA2. SAS6 and ANA2 normally interact with BLD10/CEP135 during cartwheel assembly [63, 64] to stabilise the cartwheel [16]. Given that BLD10/CEP135 is also a MT-binding molecule that contributes to basal body elongation and male fertility [20], we asked whether SAS6 and/or ANA2 are involved in recruiting BLD10 to the sperm basal body. We observed that depletion of SAS6 or ANA2 after centriole assembly reduces BLD10 at the spermatocyte basal body (Figure 6C). Consistent with previous data by us and others using BLD10 mutants [20], BLD10 depletion after centriole biogenesis also reduces basal body length (Figure 6C) and male fertility (Figure

S9D). Altogether, these results indicate that both SAS6 and ANA2 are involved in recruiting BLD10 after centriole biogenesis, thus playing an underappreciated critical role in basal body elongation in the *Drosophila* sperm.

SAS6 and ANA2 cooperate to trigger ectopic elongation of the neuronal basal body

As neuronal basal bodies are short in length and loose core cartwheel components during ciliogenesis (Figure 1, 2), we wondered whether it would be possible to ectopically induce their elongation as well as retaining the cartwheel.

We first asked whether SAS6 is sufficient to trigger ectopic elongation of this basal body. To ensure that we covered the critical window of time for basal body elongation and cartwheel retention, we first expressed SAS6 ubiquitously in all cells, beyond the time where it normally stops to express in both neuronal types (Figure 7A). We first analysed the length of the distal basal body and saw no effect in its length, even though ectopic SAS6 localised to the basal body (Figure 7B). We reasoned that either ANA2/STIL is more critical than SAS6 to recruit BLD10, or alternatively SAS6 and ANA2 need to be in a complex for their function in recruiting BLD10, as both molecules are known to bind BLD10 independently [63, 64]. Interestingly, only the ectopic expression of both is sufficient to recruit more BLD10 and promote basal body elongation (Figure 7B, C). We further confirmed this result by expressing both proteins specifically in differentiating neurons (Figure S12C). Furthermore, the flies that ectopically express both SAS6 and ANA2 are deficient for smelling and coordination (Figure 7B and S12B, C).

To further understand the molecular basis of the later results, we asked whether SAS6 or/and ANA2 have the intrinsic capacity to ectopically recruit BLD10 in these cells. We thus investigated their localization at ectopic concentration sites that form upon the ectopic expression of these proteins. This event occurs after the basal body starts to nucleate the neuronal cilium (Figure S13A). Importantly, the co-expression of both SAS6 and ANA2 was necessary and sufficient to recruit BLD10 to the ectopic sites (Figure S13B*i*). These ectopic concentrates can also recruit other centrosomal components and Pericentrin´s conserved, centriole-localising PACT domain. However, these ectopic structures were not supernumerary

centrioles, as other core centriolar components, such as ANA1, were not present (Figure S13B*ii*).

Finally, given that *Chlamydomonas* SAS6 can self-oligomerise to form cartwheels and BLD10 facilitates the formation of the cartwheel stalk *in vitro* [65], we wondered whether ubiquitous expression of SAS6 would be sufficient to retain the cartwheel in neurons. We found that though ectopically expressed SAS6 localised to the neuronal basal body, it failed to retain the cartwheel (Figure S12A). We hypothesised that perhaps SAS6 needs ANA2 for its function in retaining the cartwheel in the fly. For this experiment we ensured both SAS6 and ANA2 were always present at the centrioles, which generated some changes in basal body radial symmetry (Figure S12B). Even though both molecules localise to basal bodies and were sufficient to induce elongation as discussed above, the cartwheel was not retained, suggesting that another yet unknown factor regulates cartwheel disappearance in neurons.

In summary, we observed that while SAS6, a core structural component of the cartwheel, has a canonical role in the assembly of all centrioles in the fly, it only contributes to further elongating specific basal bodies (Figure 5, 6). We show that in testes, both SAS6 and its recruiter ANA2 are additionally involved in the elongation of the long sperm basal body and male fertility, through BLD10/CEP135 recruitment. In contrast, SAS6 was not required for basal body maintenance and function in neurons. Importantly, though SAS6-ANA2 mis-expression in the neurons does not retain the cartwheel, it leads to ectopic elongation of the basal bodies, leading to neuronal cilia dysfunction. Altogether, these results show that differential tissue regulation of SAS6 and ANA2/STIL is critical to define basal body length (see Figure 8C for a summary). In conclusion, our results indicate that differential presence of a set of conserved core centriolar components contributes to the formation of morphologically distinct ciliary bases.

Discussion

Cilia can have many different functions, raising interest on the mechanisms of their diversification. Here we investigated whether the ciliary base is diverse in distinct cilia types in *Drosophila melanogaster*. We created a comprehensive high-resolution atlas of the ultrastructure and of the localisation of components in four different types of *Drosophila* ciliary bases using TEM, ET and localisation profiles (3D-SIM) for 15 evolutionarily conserved core ciliary base components. We identified universal aspects of all ciliary bases, revealing a common scaffold, and discovered large diversity in its micron-scale (organisation and length of basal bodies, accessory structures and transition zones) and nano-scale structures (types of MTs (e.g., singlet, doublet or triplet) and presence of cartwheel in the basal body, and shape of linkers in the transition zone) (Figure 1-3 and 8A). We determined that the evolutionary conserved ciliary components thought to be part of a conserved "ciliary base-assembly module", can be differentially regulated in different cell types (Figures 1-3E and summarised in 8A). To understand the origin of ciliary-base diversity, we focused on two conserved components, CEP290 and SAS6, which localise to distinct structures in the transition zone and centriole, respectively. We found that CEP290 is present in most ciliary bases, and participates in the formation of different MT-MT and MT-membrane linkers (Figure 3, 4 and 8B). On other hand, SAS6 along with ANA2, critical centriole assembly components, are differentially present in different cell types (Figure 2E, 8A). They are not present in neuronal basal bodies, and play a critical role in sperm basal elongation by recruiting an elongation factor, BLD10 (Figure 5-6, and 8C). This function is critical for male fertility. Ectopic expression of the SAS6-ANA2 complex in neurons leads to longer basal bodies and sensory behaviour problems (Figure 7, 8C and S12). Our work shows that differential regulation of conserved core ciliary base components contributes to ciliary diversity and underlies normal fly development.

Common scaffold and functions for the *Drosophila* ciliary base

We uncovered common aspects of distinct neuronal and sperm ciliary bases, showing a common scaffold comprising the basal body, PCM, and a transition zone. The basal body is always nine-fold symmetric with the presence of either MT singlets, doublets or triplets, and being composed of at least three MT-binding components: SAS4 and ANA1, which localise at the basal body wall, and BLD10, which links the MTs of the basal body wall to the inner part of the basal body. These results suggest those components are not only needed for centriole assembly, as previously shown [37, 66], but are integral components of the basal body structure (Figure 2E, S3 and S4) and as such may be important for its maintenance.

We also observed that all basal bodies are surrounded by one or more PCM component, comprising PLP, SPD2 and γ-tubulin (Figure 1E, S3 and S4). While γ-tubulin and pericentrin are found at the basal bodies in several ciliated organisms [38-41], SPD2 has been mostly associated with the PCM of centrosomes [27, 34]. Moreover, we observed cytoplasmic MTs in the vicinity of all basal bodies and/or rootlets (Figure S2A, C), whereas the basal foot helps to organise cytoplasmic MTs in muticiliated cells [32]. All together this evidence suggests that the ciliary base has a yet uncharacterised role in MT nucleation, which might be important for its function, for example in transporting proteins from the cytoplasm to the cilium. Further research is required to test these possibilities.

The transition fibres at the tip of the basal bodies are also nine-fold symmetric (irrespectively of the presence of doublets or triplets in the basal body) and likely composed of centriolar distal tip proteins, such as UNC, and/or components of the proximal part of the transition zone, such as CEP290 (Figure 3; [21]). Together with the fact that unc mutants fail to form neuronal cilia and show defects in triplet to doublet transition in spermatocytes [21], our subdomain localisation of UNC (Figure 3E and 8A) suggests that this OFD1-like protein is a component of the interfacing region between distal basal body and transition zone. Further work is required to test this possibility. Moreover, all transition zones are also nine-fold symmetric and composed of MT doublets. We found that MT doublets are always linked amongst themselves in all transition zones and that those MTs are also connected to the membrane by electron-

dense links in most transition zones, with exception of spermatids. CEP290 played a role in forming or maintaining those links.

From this common plan, we: i) identify universal markers of each substructure of the ciliary base; ii) propose new functions of the ciliary base, as it may act as a cytoplasmic MT-organising centre that coordinates the traffic between cell body and cilia; iii) highlight the universality and importance of links between the adjacent MTs and between the MTs and the membrane at the transition zone.

Cellular- and tissue-specific characteristics influencing cilia diversity

Our work revealed that the micron-scale and nano-scale structures of the ciliary base vary in between the cell types and even within a cell, at different time points of the cell´s development. That is the case of the number and length of basal bodies that can form cilia, as well as the presence of accessory structures and the number of MTs (singlets, doublets and triplets).

How is ciliary base diversity generated? It is known that specific transcription factors are associated with certain cilia types, such as FOXJ1 and FD3F that regulate the motility-associated genes in motile ciliated cells [8, 9], and RFX, a regulator of the expression of both rootletin and components of the ciliary shaft [67, 68]. However, other differentially expressed ciliary base components, which we studied here, are not strictly under the regulation of the same transcription factor(s) [8, 67, 68]. Other unknown factors may regulate their activity, such as yet uncharacterised transcription factors, regulation at the post-transcriptional and translational level, and interaction with novel partners in different tissues. Further work is required to address those questions.

Our work suggests that the cellular context, such as tissue specific cell cycle regulation, plays an important role in the observed ciliary base diversity. The number of mature centrioles, which can template cilia, in a given cell depends on which cell cycle stage it is in and the cell cycle regulation[69]. Neurons form cilia in the G0/G1 phase of the cell cycle, when they only have one mature centriole, thus forming one cilium. Male germ cells form four cilia during a very long meiotic G2 phase (in spermatocyte), and they form one cilium after meiosis (in spermatid), when cells have 4 basal bodies and one basal body, respectively (Figure 1, S1 and [20]).

Perhaps because the G2 phase in spermatocytes is very long (assumed to be ~72 hrs), all four centrioles mature and gain the ability to form cilia, migrating to the cell membrane and elongating from approximately 500 to 1400 nm [70]. Further research on cell cycle control of centriole-to-basal body conversion is required to solve this puzzle.

It is also possible that other cell-type specific constraints play a role in ciliary base diversification. For example, while in neurons basal bodies are surrounded by rootlets (Figure 1A, B) that connect them to the cytoplasmic membrane and are important for ciliary base stability [30]; in spermatids, basal bodies are attached to the nuclear envelope, which may provide similar properties (Figure S2C). Rootlets are also found in other ciliated cells, such as mechanosensory neurons in *C. elegans* and respiratory epithelial cells in mouse [31, 32], while the attachment of the ciliary base to the nucleus is also found in sperm cells of many other multicellular organisms [20, 71]. Interestingly, we observed that SAS4, a known component of the basal body wall, also localises to neuronal rootlets (Figure 2A, B, E, and S3D), suggesting that core basal body proteins may gain new functions in specific tissues. Knowledge of specific molecules that interact with the core components in different tissues will be critical to understand how they gain new functions.

Differential regulation of conserved core components underlies ciliary base diversity

We were surprised to observe differences in the MT-membrane linkers amongst all cilia types (Figure 3). Here we show that while CEP290 is implicated both in Y-linker as described for *Chlamydomonas*, *C.elegans* and mouse [47, 52, 53], and in MT-MT link formation, as recently observed in *C. elegans* [54], it is also required to establish a non Y-link between hook and membrane in spermatocytes (Figure 4 and 8B). It is thus likely that CEP290 interacts with other common or tissue-specific transition zone components that are differentially regulated. The fact that the linkers in the transition zone are different, and that the core transition zone components are distinctly distributed (Figure 3, S5, S6), suggests the ciliary gate comprises distinct subdomains in different cilia types, likely regulating the traffic into the cilia in a different manner. For example, five transition zone components in neurons are distributed in two subdomains along the length of transition zone, while in spermatocytes they are

homogeneously distributed in one domain (Figure 3E, 8A). It is possible that these features create barriers with diverse chemical features at the ciliary gate to differentially regulate the traffic of ciliary components. Furthermore, we showed that CEP290, a component of different transition zones, are required to form distinct MT-MT and MT-membrane linkers. However, further studies are needed to know how CEP290 generates diverse structures. We also observed that several core components are regulated differently in different tissues and/or at different stages of differentiation within the same tissues, generating diversity in the ciliary base. Although SAS6 is indispensable for the biogenesis of all basal bodies, it is differentially required for the function of diverse *Drosophila* cilia, being indispensable for the function of sperm but not neuronal cilia. Furthermore, we show that the SAS6-ANA2 complex, known to be necessary for cartwheel assembly, is also required for the elongation of the very long sperm basal bodies and is sufficient to trigger over-elongation of neuronal basal bodies, through BLD10 recruitment, without affecting the 9-fold symmetric arrangement of the MTs (Figure 5-7, 8C, and S11-13). Therefore, differential temporal regulation of core centriole components, such as SAS6 and ANA2, underlies the observed diversity in basal body length. It is possible that SAS6 is also involved in centriole elongation in human cells, as experiments interfering with its expression, or expression of mutant versions led to the formation of abnormal centrioles, which were also small [72]. Although, it is possible that differential regulation of other factors also contributes to basal body length diversity [73, 74], our data provide initial steps towards understanding differential basal body maturation programs. Finally, our results could provide an explanation for apparently contradictory roles and/or localisation of core ciliary base components, such as CEP290 and SAS6, in different model systems/organisms [47, 55, 61, 72].

Evolution of ciliary diversity

We uncovered specific features of the different ciliary bases in *Drosophila*. These results raise many questions regarding how those features came about. When did they arise in evolution? Are they specific to the same cell types in other species? While little is known, certain aspects described here, such as the preferential attachment of the basal body to either rootlets in neurons or to the nucleus in sperm, are present in both chordates and arthropods [20, 75-78].

These findings suggest that at least the preferential attachment of the basal body to different structures in neurons vs. sperm is an ancient diversification in animals. Further research to map the evolutionary origin of tissue specific differences is needed to shed light on the origin and regulation of different ciliary structures and functions.

Conclusion

In summary, we unveiled that the ciliary base is much more diverse than previously thought and that differential regulation of core components contributes to this diversity. The observed different functions of conserved components in different tissues provide a basis to explain complex tissue-specific phenotypes in human ciliopathies, where mutations in core components generate tissue-specific phenotypes [17, 79, 80]. Finally, the diversity documented here combined with the publicly available information on these structures in other organisms (their ultrastructures, proteomes and localisation of components) opens new avenues towards understanding the complexity of cilium biogenesis, function and evolution in a cell type specific context.

Acknowledgements

We thank Tomer Avidor-Reiss, Bénédicte Durand, Timothy Megraw and Jordan Raff for reagents. We thank Bénédicte Durand, Philippe Bastin, Alexander Dammermann, Leonor Saúde, Jagesh Shah, Gaëlle Marteil, Mariana Lince Faria, Sihem Zitouni and MBD Lab members for reviewing the manuscript and providing helpful discussions on the manuscript. We thank the Gurdon Institute Imaging Facility (Cambridge, UK), Bacterial Cell Biology Lab (ITQB, Portugal), IGC Advance Imaging unit (and its Head, Gabriel G. Martins) and IGC Electron Microscopy unit (Ana Laura Sausa, Sara Bonucci and Erin Tranfield) for helping us with image acquisition, and the IGC fly facility for helping us with fly husbandry, and MBD Lab for discussions. SCJ and SW are supported by the FCT (Fundação Portuguesa para a Ciência e Tecnologia) Fellowships SFRH/BPD/87479/2012 and SFRH/BD/52176/2013, respectively.

The laboratory of HM is supported by ERC (ERC-681443-CODECHECK) and FLAD Life Science 2020. MBD and her laboratory are supported by a FCT, an EMBO installation grant and an ERC grant (ERC-261344-CentrioleStructNumb; ERC-683258-CentrioleBirthDeath).

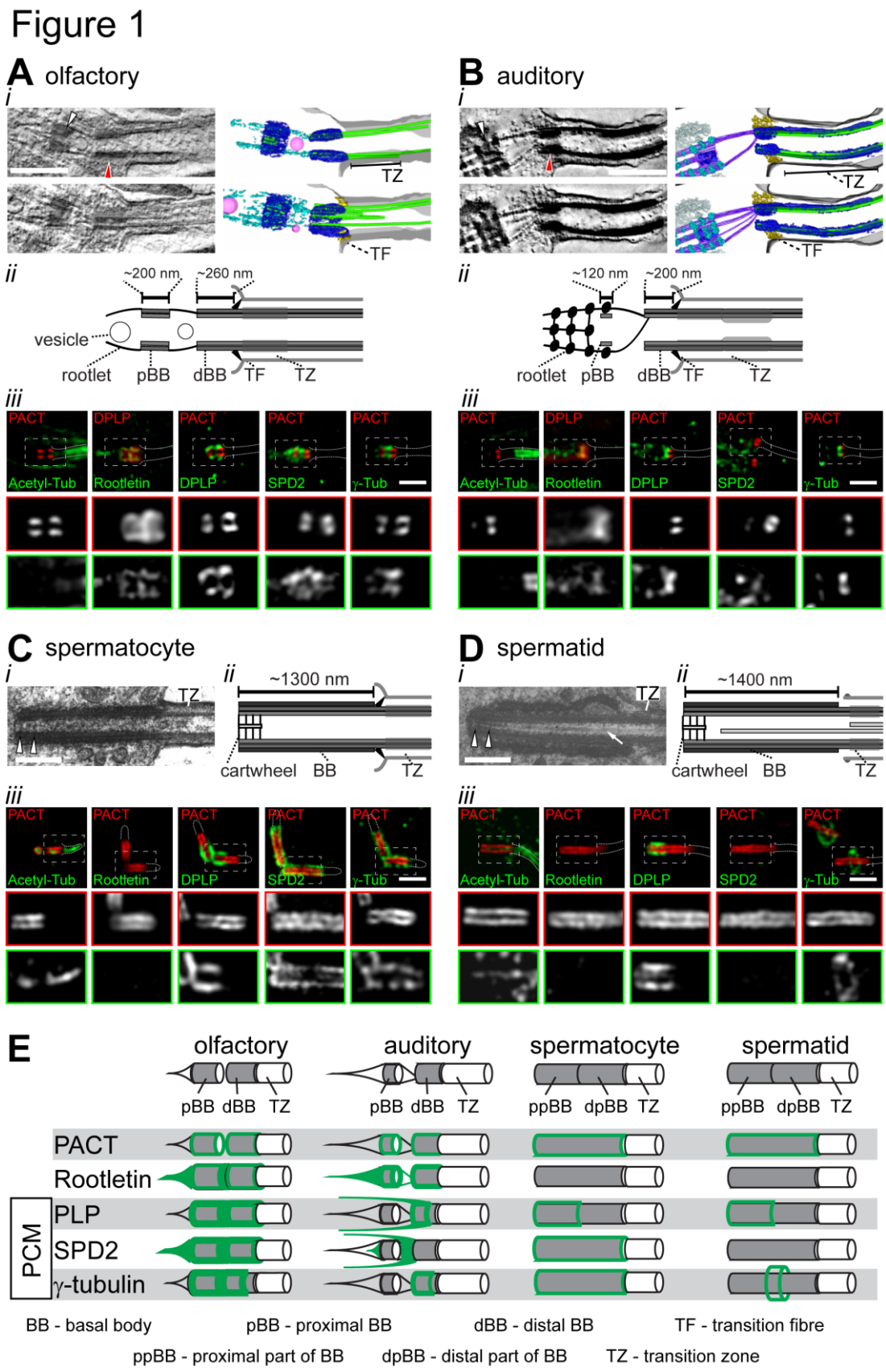

Figure 1: Micron-scale organisational map of the ciliary base shows diverse global organisation. A, B) The structure and composition of the ciliary base varies between

different types of ciliated neurons. i) Left: Longitudinal tomogram stills of the ciliary base in olfactory (A) and auditory (B) neurons showing rootlet, proximal basal bodies (pBB-white arrowhead), distal BB (dBB- red arrowhead), transition fibre (TF) and transition zone (TZ). Right: Schematic model based on the tomogram data showing transition fibre and transition zone. The BB and ciliary microtubules (MT, light green), non-MT electron densities round basal bodies and transition zone (dark blue), the electron densities of rootlet (cyan), vesicles at the ciliary base (magenta), transition fibre (golden yellow) and the cell/ciliary membranes (black) were modelled (also see Figure S2, Movie M1-2). Note that two sections of the tomograms of olfactory (A) and auditory (B) neurons show different structures, such as rootlet, vesicles, transition fibre and transition zone, of the ciliary base. ii) Schemes show longitudinal views of the ciliary base of olfactory (A) and auditory (B) neurons, representing their different regions, along with showing sizes. iii) 3D-Structured-Illumination (SIM) micrographs describe the localisation of acetylated tubulin in the cilia, rootletin (a component of rootlet), and three PCM markers (PLP, SPD2 and γ-tubulin) in both olfactory (A) and auditory (B) neurons. **C, D) The organisation and composition of the sperm ciliary bases changes during their development and differs from the homologous structures in the neurons.** i) Electron micrographs of the longitudinal section of the ciliary base of the spermatocyte (C-i) and early elongating spermatid (D-i*).* Scale bars represent 500 nm. ii) Schemes represent the longitudinal view of the ciliary bases of spermatocyte (C-ii) and spermatid (D-ii), representing their different regions, along with showing sizes. These schemes are drawn based on the data in (i), Figure S5 and [20]. iii) SIM micrographs show acetylated tubulin in the BB and cilia, rootletin and three PCM markers (PLP, SPD2 and γ-tubulin) in spermatocyte (C) and early elongating spermatid (D). Note that PACT, a basal body marker, was used as a reference to determine the relative localization of all components. The regions marked with dotted squares are shown in the insets (x2). All scale bars on electron and SIM micrographs are 500 nm and 1 µm, respectively. All electron micrographs in Ai-Di represent the features observed in ≥3 samples. E) Models represent the localisation patterns of candidate proteins (in green) shown in A-to-D-iii at the defined zones. Schemes represent localisation patterns of proteins based on the quantification shown in Figure S3 and S4. For a detailed description of the antibodies used see Table S2 and the fly genotypes used see Table S1 and S3.

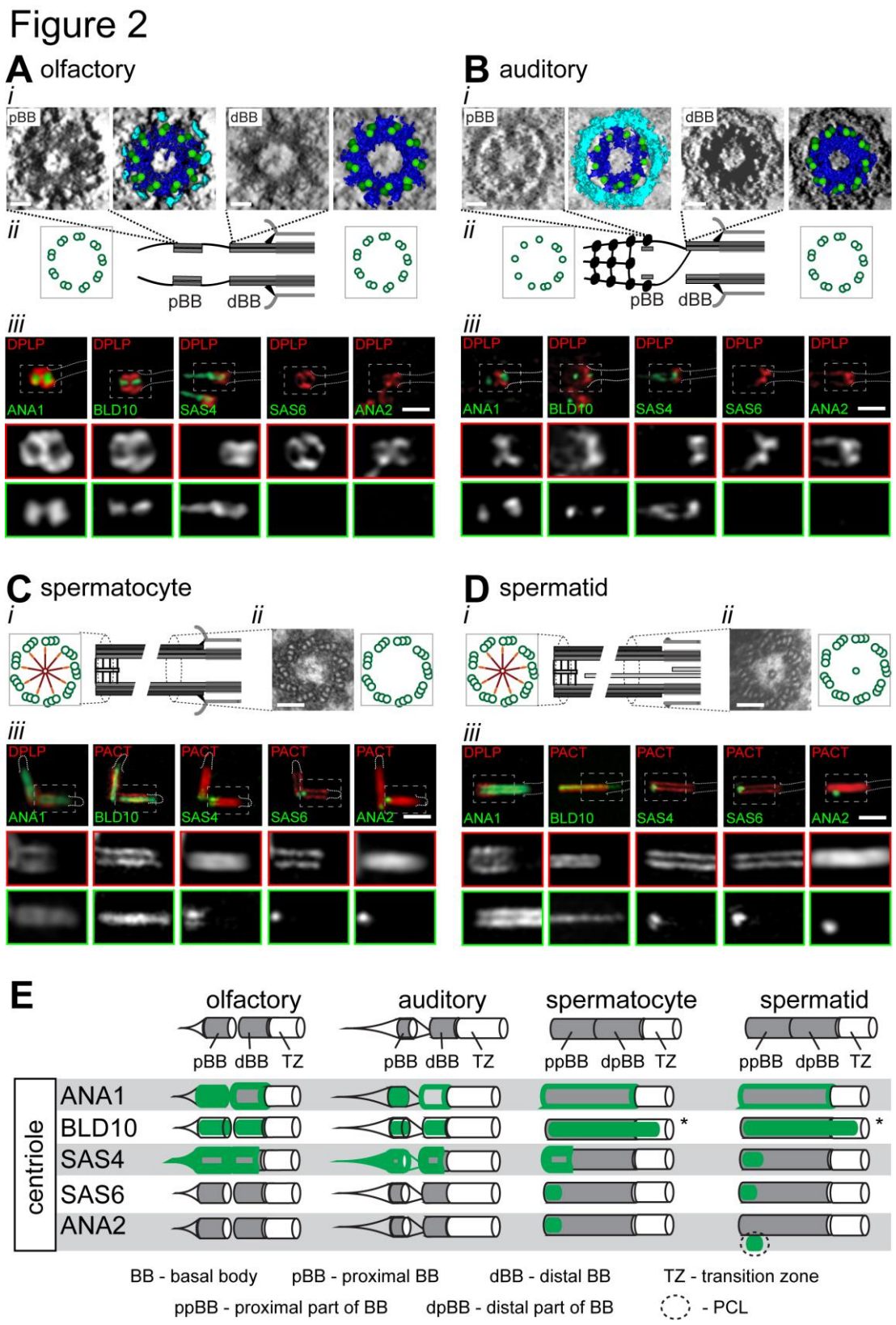

Figure 2: Basal body nanoscale structure and composition vary between cell types. A, B) The MTs and biochemical composition of basal bodies vary between different neurons. i) Left: Cross section tomogram stills showing the proximal part of the proximal basal body (pBB) and distal BB (dBB) of the olfactory (A) and auditory (B) ciliary bases. Right:

Schematic models based on and overlaying the tomogram data. We modelled A- (light green) and B- (dark green) tubules of BB microtubules (MT), the non-MT electron densities round BBs (dark blue), the electron densities of rootlet (cyan) and the cell/ciliary membranes (black). ii) Schemes present the longitudinal view of the BBs (middle) and cross section view of their MT organisations (green) in olfactory (A) and auditory (B) neurons (also see Figure 1, Figure S2, Movie M3-6). iii) SIM images describe the localisation of five centriolar proteins: ANA1, BLD10, SAS4, SAS6 and ANA2. **C, D) Both basal body structure and composition in sperm cells are very different from those in neurons, but do not significantly change during progression from spermatocyte to spermatid.** i) The scheme shows the cross-section view of the proximal part of the sperm BBs that harbour cartwheel based on the data in Figure 1 C-i, D-i and [20]. ii) Electron micrographs (left) and their respective schemes (right) show the MT organisation of the BB in spermatocyte (C) and early elongating spermatid (D). iii) SIM images describe the localisation of five centriolar proteins, such as ANA1, BLD10, SAS4, SAS6 and ANA2. Generally, PLP and PACT were used as references in neurons (A, B) and sperm cells (C, D) respectively, to determine the relative localisation of all components. The regions marked with dotted squares are shown in the insets (x2). All scale bars on electron and SIM micrographs are 100 nm and 1 µm, respectively. All electron micrographs in Ai-Di represent the features observed in ≥3 samples. E) Model representation of the localisation patterns of the proteins (in green) shown in A-D iii at the defined zones. Schemes represent the localisation patterns of proteins based on the quantification shown in Figure S3 and S4. Note that, in the elongating spermatid, ANA2 is lost from the proximal part of the BB and localises on the outer wall of the BB at the proximal centriole-like structure (PCL) (circle with a dotted line). For a detailed description of the antibodies used see Table S2 and the fly genotypes used see Table S1 and S3.

Figure 3

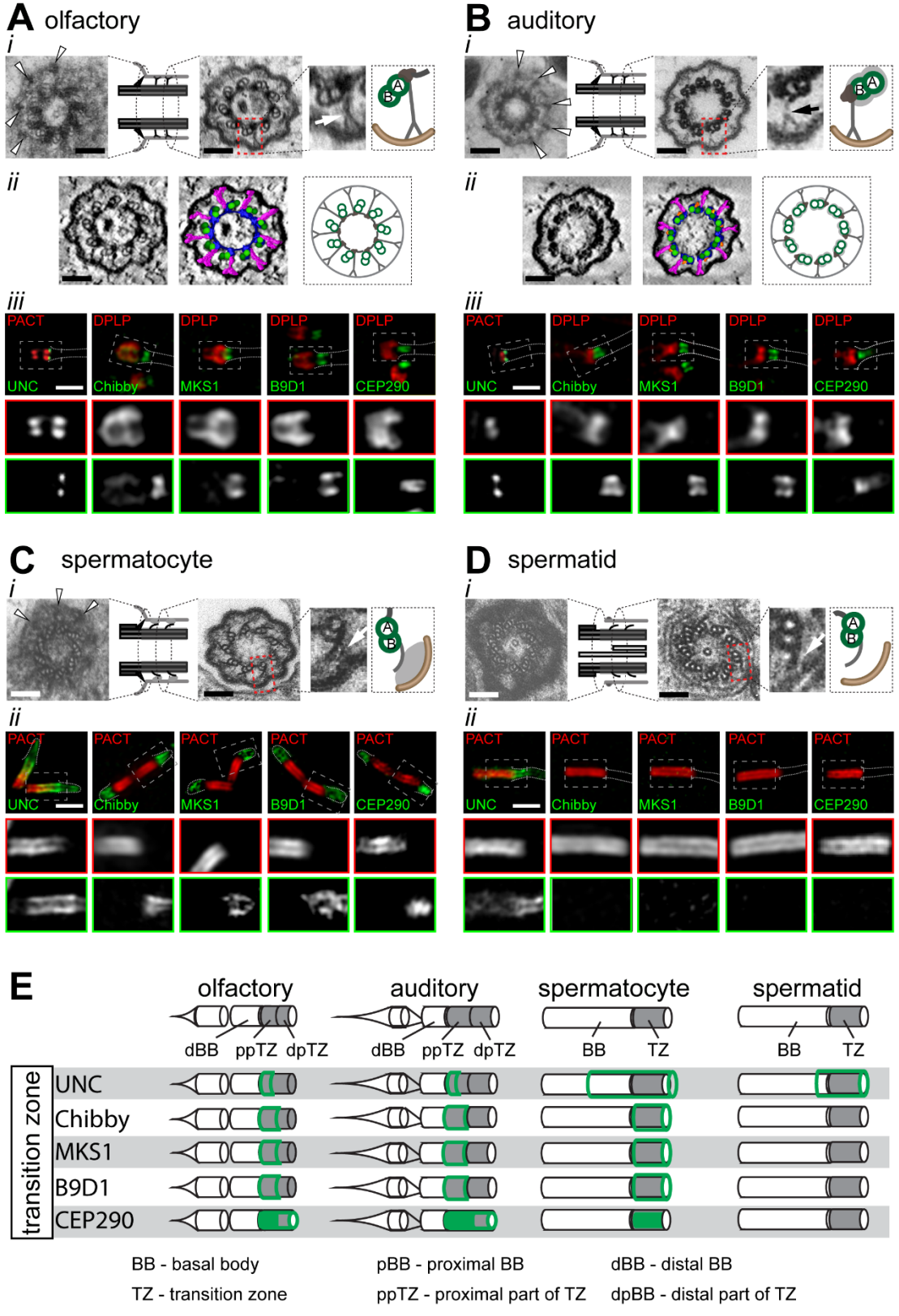

Figure 3: The transition zone nanoscale structure and composition vary in different cilia types A, B) The length, structure and composition of the transition zone are distinct in different types of neurons. i) Electron micrographs of the cross section through the transition

fibre (left) (marked with arrowheads), schemes (middle) presenting a longitudinal view of the transition zones, electron micrographs (right) of the cross section through the transition zone, and electron micrographs and schemes (extreme right) of the marked regions on the cross section electron micrographs of the olfactory (A) and auditory (B) transition zones. In the scheme (in extreme right), microtubules (MT), electron densities around MTs, MT-MT linkers, MT-membrane linkers and membrane are marked in green, light grey, dark brown, dark grey and light brown, respectively. ii) Left: Cross section tomogram stills of the transition zones in olfactory (A) and auditory (B) neurons. Middle: Schematic model based on and overlaying the tomogram data. The A- (light green) and B- (dark green) tubules of transition zone MT, the non-MT electron densities around them (dark blue), the linkers between the doublet MTs and ciliary membrane (MT –membrane linker; magenta) and the cell/ciliary membranes (black) were modelled. Right: Scheme presents the model of cross sections of transition zones based on the tomograms (see Movie M5-6) and electron micrographs. For a detailed description of the variations in the structures along the length of the transition zone see Figure S5. iii) SIM micrographs describe the localisation of five transition zone components, such as UNC, Chibby, MKS1, B9D1 and CEP290. **C, D) Structure and composition of the transition zone in sperm cells change during conversion from spermatocytes to spermatids and are different from the ones observed in neurons.** i) Electron micrographs of the cross section through the distal tip of the basal body(left) showing transition fibres (arrowheads), schemes (middle) presenting a longitudinal view of the transition zones, electron micrographs (right) of the cross section through the transition zone, and electron micrographs and schemes (extreme right) of the marked regions on the cross section electron micrographs of the spermatocyte (C) and spermatid (D) transition zones. Note that in the early elongating spermatid, we studied the region that interfaces basal body and axoneme. iii) SIM images describe the localisation of five transition zone components, such as UNC, Chibby, MKS1, B9D1 and CEP290. Note that PLP and PACT were used as references in neurons (A, B) and sperm cells (C, D), respectively, to determine the relative localization of all components. The regions marked with dotted squares are shown in the insets (x2). All scale bars on electron and SIM micrographs are 100 nm and 1 µm, respectively. All electron micrographs in Ai-Di represent the features observed in ≥3 samples. E) Models represent the localisation patterns of the proteins (in green) shown in A-D iii at the defined zones. Schemes represent the localisation patterns of proteins based on the quantification shown in Figure S6. Notably, the TEM data (Figure S5) was used to estimate the true length of transition zones. For a detailed description of the fly genotypes used see Table S1 and S3.

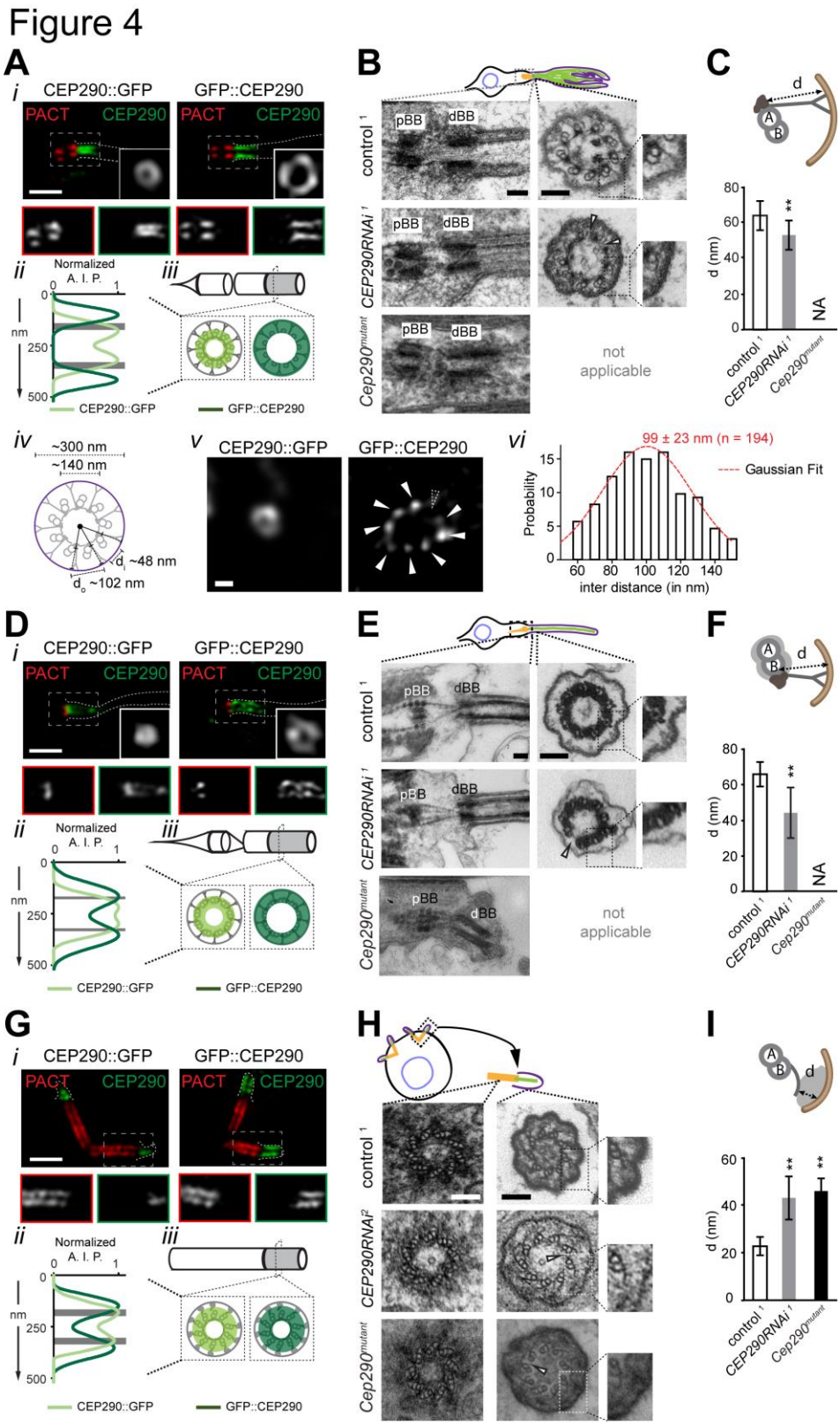

Figure 4: CEP290 is required to form diverse non-MT structures present in different types of Transition zones. A-F) In neurons, CEP290 is required to form MT-MT linkers, and MT –membrane linkers (Y-linkers). A, D) SIM micrographs describe the localisation of ectopically expressed CEP290::GFP (*Gal4^{cha19b}/UAS-CEP290::GFP*) and GFP::CEP290

(*Gal4*^{cha19b}/*UAS-GFP::CEP290*) at the TZs of olfactory (A) and auditory (D) neurons. PLP, a PCM marker, was used as a reference to determine the relative localization of CEP290 in neurons. ii) Normalised average intensity profile (A.I.P.) of the differently tagged CEP290 along the diameter of the TZ in neurons. A.I.P. was calculated using ≥6 samples. The grey marked regions in the plot profile represent the two sides of the walls of the MT based cylinder at the TZ and these values were measured using electron micrographs of the respective cross-sections. iii) Scheme depicts the longitudinal view of the ciliary base in neurons, and localisation patterns of the differently tagged CEP290 alleles in cross sections. A iv-vi) Scheme depicts the cross section view of the ciliary base in olfactory neurons (iv), representative STED micrograph of differently GFP-tagged CEP290 (v), and histogram distribution of the distance between adjacent GFP foci in GFP::CEP290 marked TZ (vi). B, E) Electron micrographs present the longitudinal view of the ciliary base and cross section of the TZ of olfactory (B) and auditory (E) neurons in flies with different genotypes (control^{1}, *CEP290RNAi*^{1} and *Cep290*^{mutant}). Note that *Cep290*^{mutant} flies fail to grow neuronal TZs, therefore, a description of the *Cep290*^{mutant} neuronal TZ is not applicable (NA). C, F) Quantification of the distance between the MT and the ciliary membrane. Since the TZ is not formed in the neurons of *Cep290*^{mutant} flies, these measurements are not applicable (NA) in those samples. **G-I) In spermatocytes, CEP290 is required to establish MT-MT and MT-membrane linkers, but not the hooks.** G-i) SIM micrographs describe the localisation of ectopically expressed CEP290::GFP (*Gal4*^{hsp83}/*UAS-CEP290::GFP*) and GFP::CEP290 (*Gal4*^{hsp83}/*UAS-GFP::CEP290*) at the TZ of spermatocytes. PACT, a basal body marker (region of PLP that targets it to centriole), was used as a reference to determine the relative localization of CEP290 in sperm cells. ii) Normalized A.I.P. of the differently tagged CEP290 along the diameter of the TZ in the spermatocytes. A.I.P. was calculated using ≥6 samples. The grey marked regions in the plot profile represent the two sides of the walls of the MT based cylinder at the TZ and these values were measured using electron micrographs of the cross-sections. iii) Schemes depict the longitudinal view of the ciliary base in spermatocytes, and localisation patterns of the differently tagged CEP290 forms in cross section. H) Electron micrographs show a cross section of the BBs and the TZs of spermatocytes in flies of different genotypes (control^{1}, *CEP290RNAi*^{2} and *Cep290*^{mutant}). I) Quantification of the distance between the hook and the ciliary membrane. For details on the method to measure distance see Figure S9. Scale bars represent 1 µm (in Ai, Di and Gi), 100 nm (in Av) and 200 nm (in B, E and H). The total number of samples measured for each bar in C, F and I is N ≥15. For the MT-membrane distance measurements we analysed ≥3 different olfactory (C), auditory (F) neurons and spermatocytes (I). Error bars indicate ± S. D. (**-p<0.001 is estimated using the Mann-Whitney U-test). For a detailed description of the fly genotypes used see Table S3.

Figure 5

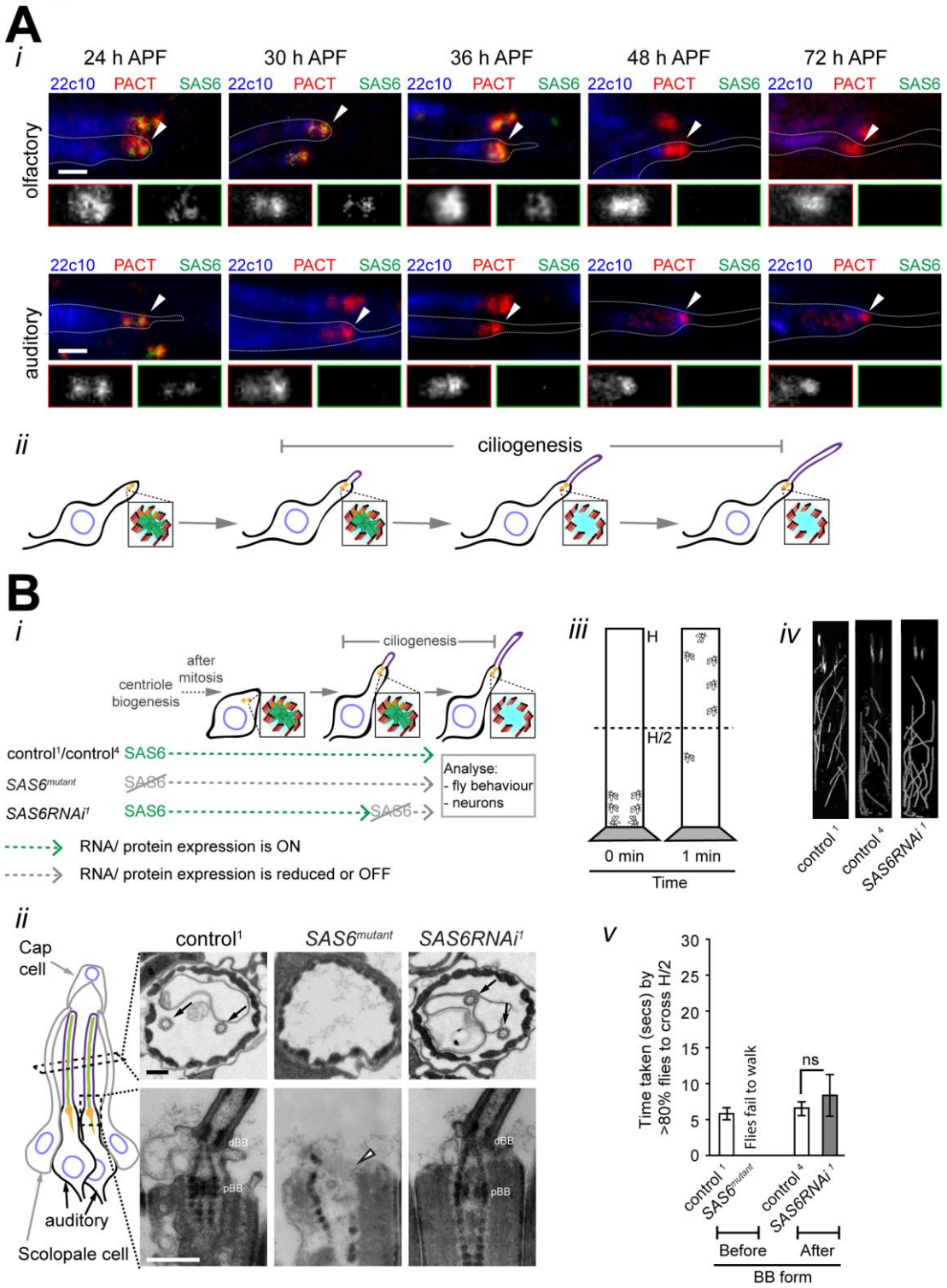

Figure 5: SAS6 is essential for centriole assembly, but not required for basal body function in neurons. A) SAS6 is removed from the basal body during ciliogenesis in neurons. Localisation of endogenous SAS6::GFP at the centrioles/basal bodies during the development of neurons at different hours after pupae formation (APF). As ciliogenesis in olfactory and auditory neurons starts between 24-36 hr APF, and most of the neuronal cilia

are elongated to their full length by 72 hr APF [81], we studied these neurons from 24 hr to 72 hr APF. White arrowheads mark the distal tip of the dendrites, where the basal bodies (BB) dock and grow cilia. PACT (red) and 22c10 (blue) mark the BB and dendrites in the developing neurons, respectively. The scale bars represent 1 µm. We repeated the experiments in A for two times. ii) Scheme depicts the proposed process of SAS6 (thus cartwheel) removal during ciliogenesis in the neurons. **B) SAS6 is required for centriole/basal body assembly; however, it is dispensable for cilia function.** i) Schematic representation of the experimental plans to reduce/remove SAS6 during centriole and cilia biogenesis. Here, we compiled the temporal information regarding the protein expression based on data in Figure 5A and expression profile of the Gal4 promoter in [81]. ii) Left: Schematic representation of a single scolopidium with auditory neurons and supporting cells. Right: Electron micrographs present the cross sections of a single scolopidium and the longitudinal sections through the ciliary base of auditory neurons in flies with different genotypes (control[1], *SAS6*^{mutant} and *SAS6RNAi*[1]). Arrows mark the ciliary axoneme, and empty arrowhead marks the ciliary base without BBs. The scale bars represent 200 nm. We observed similar results in two independent experiments. iii-v) Scheme (iii) describes the negative-geotaxis (bang) assay with the vertical tube used to measure the negative-geotaxis ability of the adult flies. iv) Representative kymographs of the ten flies of respective genotypes followed for first 10 seconds after the bang. v) Quantification of the time taken by ≥ 80% of the flies to successfully climb the half height mark of the tube (18 cm long). The number of flies used for each histogram bar in each experiment is a total of N ≥60; 3 replicate experiments were performed. The error bars indicate ±S. D. (significance in the difference between sample populations were estimated using the Mann-Witney U-test). For a detailed description of the fly genotypes used see Table S3.

Figure 6

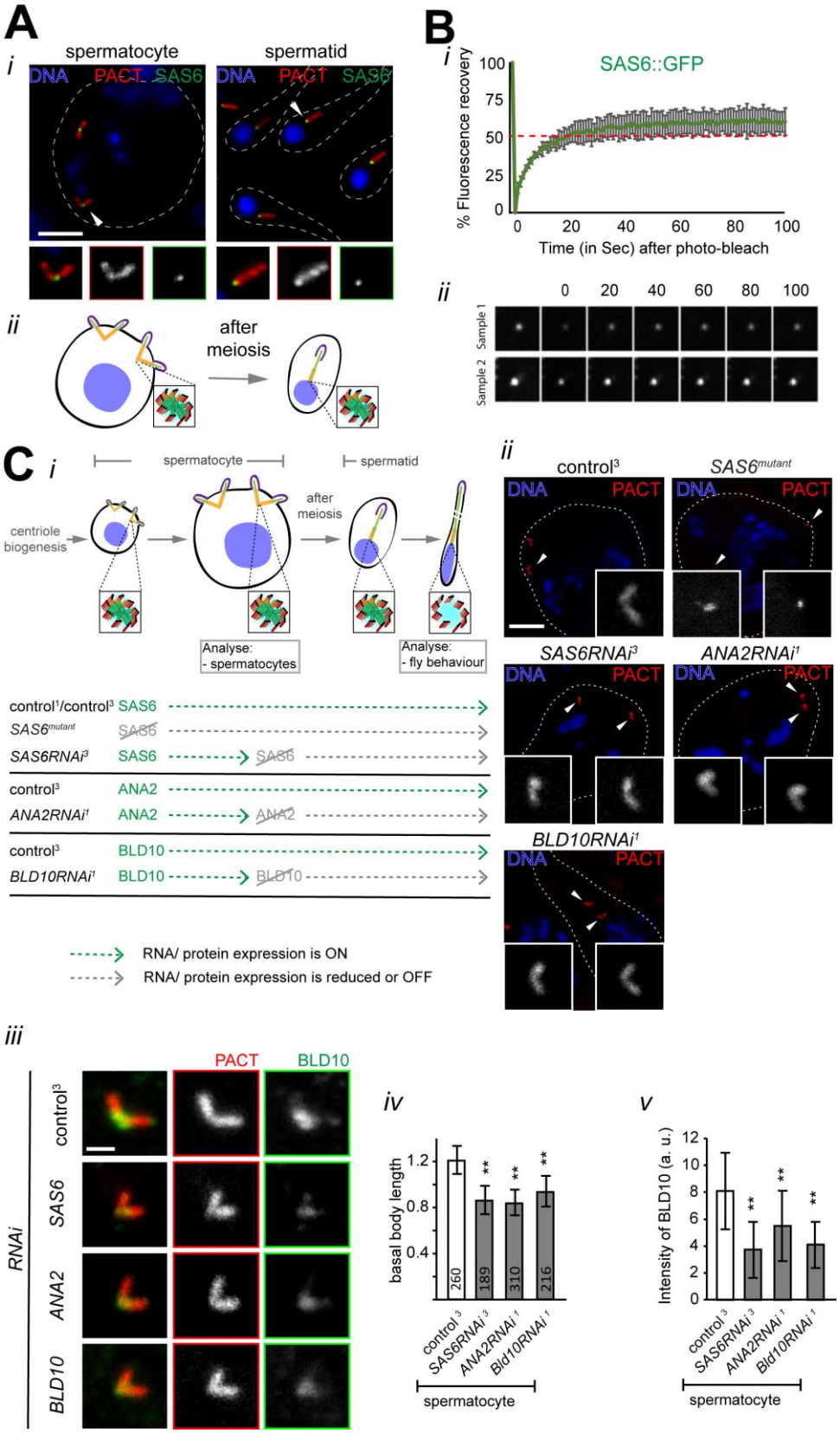

Figure 6: Cartwheel components, SAS6 and ANA2, are both required for BLD10/CEP135 localization to the sperm basal body and BB elongation. A) (i) Localisation of endogenous

SAS6::GFP at the proximal part of basal bodies (BB) (white arrowheads) in spermatocytes and early elongating spermatid (ii). PACT (red) marks the BBs during the development of sperm cells. The scale bar represents 5 µm. We repeated the experiments in A for three times. ii) Scheme depicts the proposed process of cartwheel maintenance during the development of sperm cells based on the SAS6::GFP localisation data and data in Figure 1C, D. B) Fluorescence recovery after photobleaching (FRAP) profile of SAS6::GFP in the spermatocytes (i). The number of samples used is N=6. ii) Micrographs of two representative examples of SAS6::GFP recovery after photobleaching. C) i) Schematic representation of the experimental plans to remove/reduce SAS6 during centriole biogenesis and BB elongation, and to remove/reduce ANA2 and BLD10 during BB elongation. We compiled the temporal information regarding protein expression based on the data in Figure 6A-B and the expression profile of the Gal4´s promoter in [82]. (ii) Representative images of the mature spermatocytes of flies with different genotypes (control[3], *SAS6*^{mutant}, *SAS6RNAi*[3], *ANA2RNAi*[1] and *BLD10RNAi*[1]). RFP::PACT (red) marks BBs and DAPI (blue) stains DNA. Insets show RFP::PACT close to the arrowhead (in grey scale). For quantification of the number of BBs per cell in mature spermatocytes see Figure S8. (iii) Representative images of mature spermatocyte BB of flies with different genotypes (control[3], *SAS6RNAi*[3], *ANA2RNAi*[1] and *BLD10RNAi*[1]). RFP::PACT (red) marks BBs and Anti-BLD10 antibody (green) stains the BB. Scale bars in (ii) and (iii) represent 5 and 1 µm, respectively. Quantification of the BB length (vi) and the total amount of BLD10 at the BBs (v) in mature spermatocytes. For BLD10 quantification, the number of BBs quantified for each genotype is N ≥ 80. We repeated all experiments in C for three times. Sample number is mentioned on the histogram bars. Error bars indicate ±S. D. (**-p<0.001 is estimated using the Mann-Whitney U-test). For a detailed description of the fly genotypes used see Table S3.

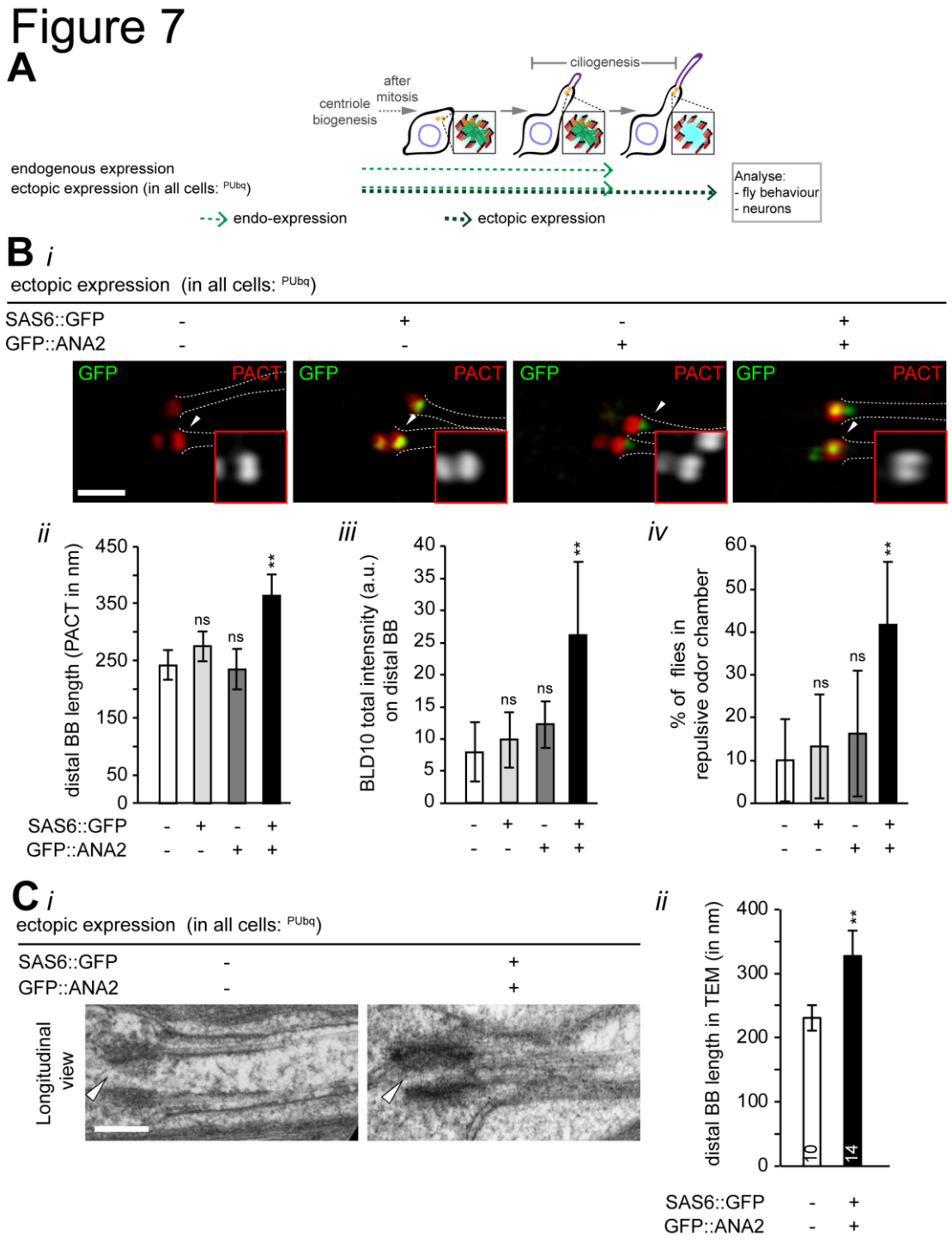

Figure 7: SAS6 and ANA2, two cartwheel proteins, cooperate to elicit an ectopic basal body elongation program in olfactory neurons, leading to odor reception defects. A) Schematic representation of the experimental plans to ubiquitously express candidate proteins (SAS6, ANA2 and co-expression of both proteins) during centriole and cilia biogenesis. Here, we compiled the temporal information regarding the protein expression based on data in Figure 6A and expression profile of the Gal4 promoter in [81]. B) i) Representative SIM images of the longitudinal view of basal bodies in flies with different genotypes. PACT (red) marks the basal bodies (BBs) in the neurons. Insets show PACT (red) close to the arrowhead (in grey

scale). Note that olfactory neurons in control flies or flies expressing only SAS6 or ANA2 have one cilia per cell. Upon ectopic expression of both SAS6 and ANA2, we observed one cilium per cell in the majority of the olfactory neurons (78%), as shown in figure. In the remainder olfactory neurons (not shown), we observed that cells were forming two cilia, each with one basal body. In this study we focused on the largest population of the neurons. Quantification of the distal BB length (ii) and total BLD10 in dBB (iii) in olfactory neurons. The number of distal basal bodies analysed in this experiment (ii) and (iii) is a total of N≥35 and N≥37, respectively. These results were observed in three independent experiments. iv) Quantification of the percentage of the flies found in the repulsive odor chamber. The number of flies used for each histogram bar in each experiment is a total of N≥60; 3 replicate experiments were performed. C) i) Representative electron micrographs show longitudinal sections through the ciliary base through distal BB of olfactory neurons in flies with different genotypes (see also Figure S12B for cross sections). Empty arrow head marks the proximal region of the distal basal body without cartwheel. ii) Quantification of the distal BB length using eletron micrographs in olfactory neurons from at least two different antenna. The TEM results were observed in two independent experiments. Scale bars in B and C represent 1 and 0.2 µm, respectively. The error bars indicate ±S. D. (significance in the difference between sample populations were estimated using the Mann-Witney U-test). ns and ** indicate not significant and $p < 0.001$, respectively. For a detailed description of the fly genotypes used see Table S3.

Figure 8

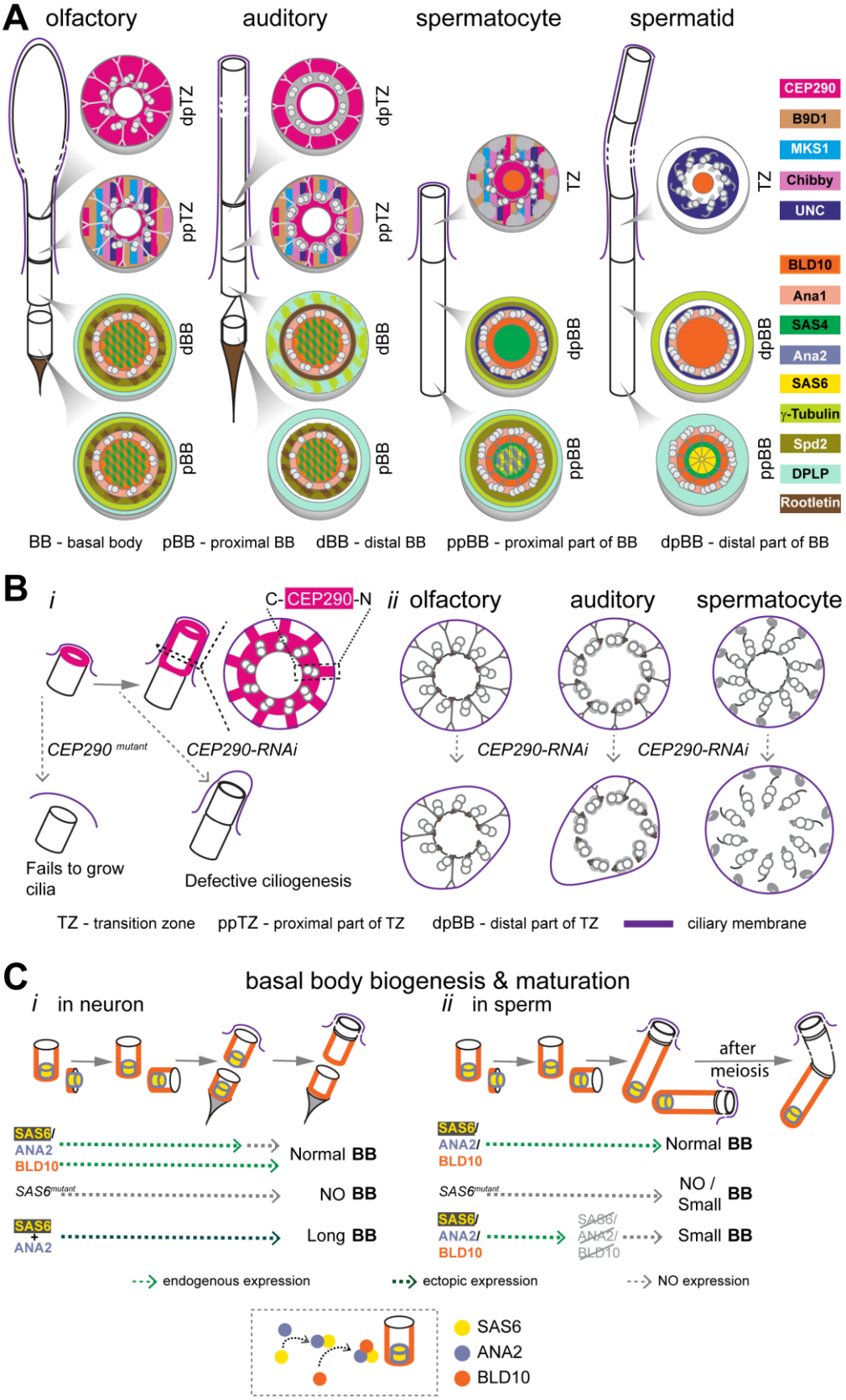

Figure 8: The structure and composition of the ciliary base are distinct in different cell types. A) Scheme representing localisation of different PCM, centriole and transition zone

components in four different zones of the ciliary base in distinct ciliated cells in the adult fly. In neurons: the four zones are- proximal basal body, distal basal body, proximal and distal parts of the transition zone. In sperm cells: the zones are proximal and distal parts of basal bodies and transition zone. In the elongating spermatid we are describing the area distal to the basal body, in the proximal part of the cilia, as a zone of transition between the basal body and axoneme. Note that the tip of the cilia in spermatids has been shown to host many bona fide transition zone proteins (for details, please see [29]). B) Model representation of CEP290 localisation and function in distinct TZ linkers in different ciliated cells. C) Model representation of SAS6, ANA2 and BLD10 localisation and their function in basal body elongation in different ciliated cells, namely neurons and sperm cells. Furthermore, a model presenting the dynamic properties of these three molecules and mechanism of their recruitment at the basal body during its assembly and maturation (in the box marked with dotted lines).

References

1. Bettencourt-Dias, M., Hildebrandt, F., Pellman, D., Woods, G. & Godinho, S.A. Centrosomes and cilia in human disease. *Trends Genet* **27**, 307-315 (2011).
2. Jana, S.C., Marteil, G. & Bettencourt-Dias, M. Mapping molecules to structure: unveiling secrets of centriole and cilia assembly with near-atomic resolution. *Curr Opin Cell Biol* **26**, 96-106 (2014).
3. Carvalho-Santos, Z., Azimzadeh, J., Pereira-Leal, J.B. & Bettencourt-Dias, M. Evolution: Tracing the origins of centrioles, cilia, and flagella. *J Cell Biol* **194**, 165-175 (2011).
4. Ibanez-Tallon, I., Heintz, N. & Omran, H. To beat or not to beat: roles of cilia in development and disease. *Hum Mol Genet* **12 Spec No 1**, R27-35 (2003).
5. Mukhopadhyay, S., Lu, Y., Shaham, S. & Sengupta, P. Sensory signaling-dependent remodeling of olfactory cilia architecture in C. elegans. *Dev Cell* **14**, 762-774 (2008).
6. Silverman, M.A. & Leroux, M.R. Intraflagellar transport and the generation of dynamic, structurally and functionally diverse cilia. *Trends Cell Biol* **19**, 306-316 (2009).
7. Mukhopadhyay, S. *et al.* Distinct IFT mechanisms contribute to the generation of ciliary structural diversity in C. elegans. *The EMBO journal* **26**, 2966-2980 (2007).
8. Newton, F.G. *et al.* Forkhead transcription factor Fd3F cooperates with Rfx to regulate a gene expression program for mechanosensory cilia specialization. *Dev Cell* **22**, 1221-1233 (2012).
9. Yu, X., Ng, C.P., Habacher, H. & Roy, S. Foxj1 transcription factors are master regulators of the motile ciliogenic program. *Nat Genet* **40**, 1445-1453 (2008).
10. Czarnecki, P.G. & Shah, J.V. The ciliary transition zone: from morphology and molecules to medicine. *Trends Cell Biol* **22**, 201-210 (2012).
11. Reiter, J.F., Blacque, O.E. & Leroux, M.R. The base of the cilium: roles for transition fibres and the transition zone in ciliary formation, maintenance and compartmentalization. *EMBO Rep* **13**, 608-618 (2012).
12. Brito, D.A., Gouveia, S.M. & Bettencourt-Dias, M. Deconstructing the centriole: structure and number control. *Curr Opin Cell Biol* **24**, 4-13 (2012).
13. Kobayashi, T. & Dynlacht, B.D. Regulating the transition from centriole to basal body. *J Cell Biol* **193**, 435-444 (2011).
14. Garcia-Gonzalo, F.R. *et al.* A transition zone complex regulates mammalian ciliogenesis and ciliary membrane composition. *Nat Genet* **43**, 776-784 (2011).
15. Roberson, E.C. *et al.* TMEM231, mutated in orofaciodigital and Meckel syndromes, organizes the ciliary transition zone. *J Cell Biol* **209**, 129-142 (2015).

16. Bayless, B.A., Giddings, T.H., Jr., Winey, M. & Pearson, C.G. Bld10/Cep135 stabilizes basal bodies to resist cilia-generated forces. *Mol Biol Cell* **23**, 4820-4832 (2012).
17. Fliegauf, M., Benzing, T. & Omran, H. When cilia go bad: cilia defects and ciliopathies. *Nat Rev Mol Cell Biol* **8**, 880-893 (2007).
18. Jana, S.C., Mendonca, S., Werner, S. & Bettencourt-Dias, M. Methods to Study Centrosomes and Cilia in Drosophila. *Methods in molecular biology* **1454**, 215-236 (2016).
19. Vieillard, J., Duteyrat, J.L., Cortier, E. & Durand, B. Imaging cilia in Drosophila melanogaster. *Methods Cell Biol* **127**, 279-302 (2015).
20. Carvalho-Santos, Z. *et al.* BLD10/CEP135 is a microtubule-associated protein that controls the formation of the flagellum central microtubule pair. *Dev Cell* **23**, 412-424 (2012).
21. Gottardo, M., Callaini, G. & Riparbelli, M.G. The cilium-like region of the Drosophila spermatocyte: an emerging flagellum? *Journal of cell science* **126**, 5441-5452 (2013).
22. Gottardo, M. *et al.* Loss of Centrobin Enables Daughter Centrioles to Form Sensory Cilia in Drosophila. *Curr Biol* **25**, 2319-2324 (2015).
23. Sarpal, R. *et al.* Drosophila KAP interacts with the kinesin II motor subunit KLP64D to assemble chordotonal sensory cilia, but not sperm tails. *Curr Biol* **13**, 1687-1696 (2003).
24. Jana, S.C., Bettencourt-Dias, M., Durand, B. & Megraw, T.L. Drosophila melanogaster as a model for basal body research. *Cilia* **5**, 22 (2016).
25. Jana, S.C., Mendonca, S, Werner, S., Bettencourt-Dias, M. Methods to study centrosomes and cilia in Drosophila. *Methods Cell Biol* (2016).
26. Albert, J.T. & Gopfert, M.C. Hearing in Drosophila. *Curr Opin Neurobiol* **34**, 79-85 (2015).
27. Martinez-Campos, M., Basto, R., Baker, J., Kernan, M. & Raff, J.W. The Drosophila pericentrin-like protein is essential for cilia/flagella function, but appears to be dispensable for mitosis. *J Cell Biol* **165**, 673-683 (2004).
28. Baker, J.D., Adhikarakunnathu, S. & Kernan, M.J. Mechanosensory-defective, male-sterile unc mutants identify a novel basal body protein required for ciliogenesis in Drosophila. *Development* **131**, 3411-3422 (2004).
29. Basiri, M.L. *et al.* A migrating ciliary gate compartmentalizes the site of axoneme assembly in Drosophila spermatids. *Curr Biol* **24**, 2622-2631 (2014).
30. Chen, J.V. *et al.* Rootletin organizes the ciliary rootlet to achieve neuron sensory function in Drosophila. *J Cell Biol* **211**, 435-453 (2015).

31. Doroquez, D.B., Berciu, C., Anderson, J.R., Sengupta, P. & Nicastro, D. A high-resolution morphological and ultrastructural map of anterior sensory cilia and glia in Caenorhabditis elegans. *Elife* **3**, e01948 (2014).
32. Clare, D.K. *et al.* Basal foot MTOC organizes pillar MTs required for coordination of beating cilia. *Nat Commun* **5**, 4888 (2014).
33. Galletta, B.J. *et al.* Drosophila pericentrin requires interaction with calmodulin for its function at centrosomes and neuronal basal bodies but not at sperm basal bodies. *Mol Biol Cell* **25**, 2682-2694 (2014).
34. Dix, C.I. & Raff, J.W. Drosophila Spd-2 recruits PCM to the sperm centriole, but is dispensable for centriole duplication. *Curr Biol* **17**, 1759-1764 (2007).
35. Bouissou, A. *et al.* {gamma}-Tubulin ring complexes regulate microtubule plus end dynamics. *J Cell Biol* **187**, 327-334 (2009).
36. Blachon, S., Khire, A. & Avidor-Reiss, T. The origin of the second centriole in the zygote of Drosophila melanogaster. *Genetics* **197**, 199-205 (2014).
37. Blachon, S. *et al.* A proximal centriole-like structure is present in Drosophila spermatids and can serve as a model to study centriole duplication. *Genetics* **182**, 133-144 (2009).
38. Muhlhans, J., Brandstatter, J.H. & Giessl, A. The centrosomal protein pericentrin identified at the basal body complex of the connecting cilium in mouse photoreceptors. *PloS one* **6**, e26496 (2011).
39. Voronina, V.A. *et al.* Inactivation of Chibby affects function of motile airway cilia. *The Journal of cell biology* **185**, 225-233 (2009).
40. Muresan, V., Joshi, H.C. & Besharse, J.C. Gamma-tubulin in differentiated cell types: localization in the vicinity of basal bodies in retinal photoreceptors and ciliated epithelia. *J Cell Sci* **104 (Pt 4)**, 1229-1237 (1993).
41. Liang, A. *et al.* Gamma-tubulin is permanently associated with basal bodies in ciliates. *European journal of cell biology* **70**, 331-338 (1996).
42. Arikawa, K. & Williams, D.S. Acetylated alpha-tubulin in the connecting cilium of developing rat photoreceptors. *Investigative ophthalmology & visual science* **34**, 2145-2149 (1993).
43. Fu, J. & Glover, D.M. Structured illumination of the interface between centriole and peri-centriolar material. *Open Biol* **2**, 120104 (2012).
44. Dzhindzhev, N.S. *et al.* Plk4 phosphorylates Ana2 to trigger Sas6 recruitment and procentriole formation. *Curr Biol* **24**, 2526-2532 (2014).
45. Guichard, P., Chretien, D., Marco, S. & Tassin, A.M. Procentriole assembly revealed by cryo-electron tomography. *The EMBO journal* **29**, 1565-1572 (2010).
46. Gonzalez, C., Tavosanis, G. & Mollinari, C. Centrosomes and microtubule organisation during Drosophila development. *J Cell Sci* **111 (Pt 18)**, 2697-2706 (1998).

47. Craige, B. *et al.* CEP290 tethers flagellar transition zone microtubules to the membrane and regulates flagellar protein content. *J Cell Biol* **190**, 927-940 (2010).
48. Williams, C.L. *et al.* MKS and NPHP modules cooperate to establish basal body/transition zone membrane associations and ciliary gate function during ciliogenesis. *J Cell Biol* **192**, 1023-1041 (2011).
49. Hagiwara, H., Ohwada, N., Aoki, T., Suzuki, T. & Takata, K. The primary cilia of secretory cells in the human oviduct mucosa. *Medical molecular morphology* **41**, 193-198 (2008).
50. Enjolras, C. *et al.* Drosophila chibby is required for basal body formation and ciliogenesis but not for Wg signaling. *J Cell Biol* **197**, 313-325 (2012).
51. Barker, A.R., Renzaglia, K.S., Fry, K. & Dawe, H.R. Bioinformatic analysis of ciliary transition zone proteins reveals insights into the evolution of ciliopathy networks. *BMC Genomics* **15**, 531 (2014).
52. Rachel, R.A. *et al.* CEP290 alleles in mice disrupt tissue-specific cilia biogenesis and recapitulate features of syndromic ciliopathies. *Hum Mol Genet* **24**, 3775-3791 (2015).
53. Li, C. *et al.* MKS5 and CEP290 Dependent Assembly Pathway of the Ciliary Transition Zone. *PLoS biology* **14**, e1002416 (2016).
54. Schouteden, C., Serwas, D., Palfy, M. & Dammermann, A. The ciliary transition zone functions in cell adhesion but is dispensable for axoneme assembly in C. elegans. *J Cell Biol* **210**, 35-44 (2015).
55. Yang, T.T. *et al.* Superresolution Pattern Recognition Reveals the Architectural Map of the Ciliary Transition Zone. *Sci Rep* **5**, 14096 (2015).
56. Pratt, M.B. *et al.* Drosophila sensory cilia lacking MKS proteins exhibit striking defects in development but only subtle defects in adults. *J Cell Sci* **129**, 3732-3743 (2016).
57. Vieillard, J. *et al.* Transition zone assembly and its contribution to axoneme formation in Drosophila male germ cells. *J Cell Biol* **214**, 875-889 (2016).
58. Drivas, T.G., Holzbaur, E.L. & Bennett, J. Disruption of CEP290 microtubule/membrane-binding domains causes retinal degeneration. *J Clin Invest* **123**, 4525-4539 (2013).
59. Singh, H. *et al.* Visualization and quantification of cardiac mitochondrial protein clusters with STED microscopy. *Mitochondrion* **12**, 230-236 (2012).
60. Benton, R., Sachse, S., Michnick, S.W. & Vosshall, L.B. Atypical membrane topology and heteromeric function of Drosophila odorant receptors in vivo. *PLoS biology* **4**, e20 (2006).
61. Rodrigues-Martins, A. *et al.* DSAS-6 organizes a tube-like centriole precursor, and its absence suggests modularity in centriole assembly. *Curr Biol* **17**, 1465-1472 (2007).

62. Zitouni, S. *et al.* CDK1 Prevents Unscheduled PLK4-STIL Complex Assembly in Centriole Biogenesis. *Curr Biol* **26**, 1127-1137 (2016).
63. Lin, Y.C. *et al.* Human microcephaly protein CEP135 binds to hSAS-6 and CPAP, and is required for centriole assembly. *The EMBO journal* **32**, 1141-1154 (2013).
64. Galletta, B.J. *et al.* A centrosome interactome provides insight into organelle assembly and reveals a non-duplication role for Plk4. *Nat Commun* **7**, 12476 (2016).
65. Guichard, P. *et al.* Cell-free reconstitution reveals centriole cartwheel assembly mechanisms. *Nat Commun* **8**, 14813 (2017).
66. Basto, R. *et al.* Flies without centrioles. *Cell* **125**, 1375-1386 (2006).
67. Laurencon, A. *et al.* Identification of novel regulatory factor X (RFX) target genes by comparative genomics in Drosophila species. *Genome biology* **8**, R195 (2007).
68. Cachero, S. *et al.* The gene regulatory cascade linking proneural specification with differentiation in Drosophila sensory neurons. *PLoS biology* **9**, e1000568 (2011).
69. Kong, D. *et al.* Centriole maturation requires regulated Plk1 activity during two consecutive cell cycles. *J Cell Biol* **206**, 855-865 (2014).
70. Riparbelli, M.G., Colozza, G. & Callaini, G. Procentriole elongation and recruitment of pericentriolar material are downregulated in cyst cells as they enter quiescence. *J Cell Sci* **122**, 3613-3618 (2009).
71. Soley, J.T. A comparative overview of the sperm centriolar complex in mammals and birds: Variations on a theme. *Animal reproduction science* **169**, 14-23 (2016).
72. Hilbert, M. *et al.* SAS-6 engineering reveals interdependence between cartwheel and microtubules in determining centriole architecture. *Nat Cell Biol* **18**, 393-403 (2016).
73. Saurya, S. *et al.* Drosophila Ana1 is required for centrosome assembly and centriole elongation. *Journal of cell science* **129**, 2514-2525 (2016).
74. Franz, A., Roque, H., Saurya, S., Dobbelaere, J. & Raff, J.W. CP110 exhibits novel regulatory activities during centriole assembly in Drosophila. *J Cell Biol* **203**, 785-799 (2013).
75. Abe, S., Asakura, S. & Ukeshima, A. Formation of flagella during interphase in secondary spermatocytes from Xenopus laevis in vitro. *The Journal of experimental zoology* **246**, 65-70 (1988).
76. Burton, P.R. Ultrastructural studies of microtubules and microtubule organizing centers of the vertebrate olfactory neuron. *Microsc Res Tech* **23**, 142-156 (1992).
77. Fox, H. & Hamilton, L. Ultrastructure of diploid and haploid cells of Xenopus laevis larvae. *Journal of embryology and experimental morphology* **26**, 81-98 (1971).
78. Keil, T.A. Sensory cilia in arthropods. *Arthropod Struct Dev* **41**, 515-534 (2012).

79. Martin, C.A. *et al.* Mutations in PLK4, encoding a master regulator of centriole biogenesis, cause microcephaly, growth failure and retinopathy. *Nat Genet* **46**, 1283-1292 (2014).
80. Szymanska, K. *et al.* Founder mutations and genotype-phenotype correlations in Meckel-Gruber syndrome and associated ciliopathies. *Cilia* **1**, 18 (2012).
81. Jana, S.C., Girotra, M. & Ray, K. Heterotrimeric kinesin-II is necessary and sufficient to promote different stepwise assembly of morphologically distinct bipartite cilia in Drosophila antenna. *Mol Biol Cell* **22**, 769-781 (2011).
82. Arama, E., Agapite, J. & Steller, H. Caspase activity and a specific cytochrome C are required for sperm differentiation in Drosophila. *Dev Cell* **4**, 687-697 (2003).

Supplemental Figures

Figure S1

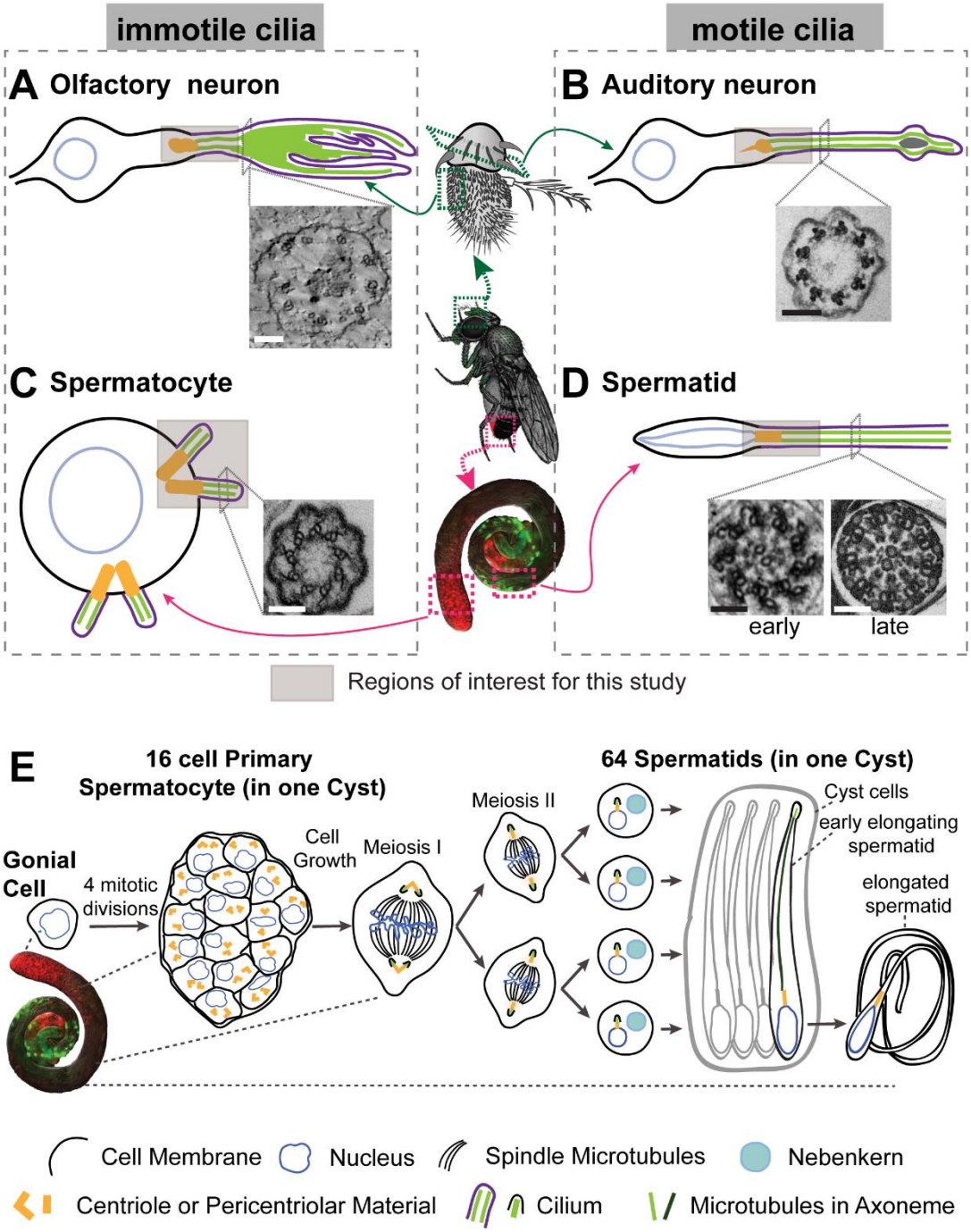

Figure S1: Different ciliated cells present in the adult *Drosophila* studied in this work (related to the Introduction**).** A-B) Large *basiconic* olfactory neurons (A) and auditory neurons (B) located in the marked regions of the third and second segment of the adult antenna, respectively. Schemes show longitudinal views and representative electron micrograph cross-sections of the marked regions. C-D) Primary cilia-like structure in spermatocytes and long

flagella in early elongating spermatid. Schemes show longitudinal views and representative electron micrograph cross-sections of the marked regions. Scale bars on all electron micrographs represent 100 nm. E) The scheme represents basal body (BB) elongation and diverse cilia assembly during *Drosophila* spermatogenesis. A stem cell after division gives rise to a gonial cell that in turn undergoes four rounds of incomplete mitotic divisions to produce a 16-cell cyst of primary spermatocytes. Primary spermatocytes go through a long G2 phase when four centrioles elongate equally and migrate to the cell membrane where each centriole/basal body grows a cilium. Each spermatocyte then undergoes two consecutive meiotic divisions without both DNA replication and centriole duplication. As a result, each early spermatid harbours one basal body that nucleates the sperm flagellum.

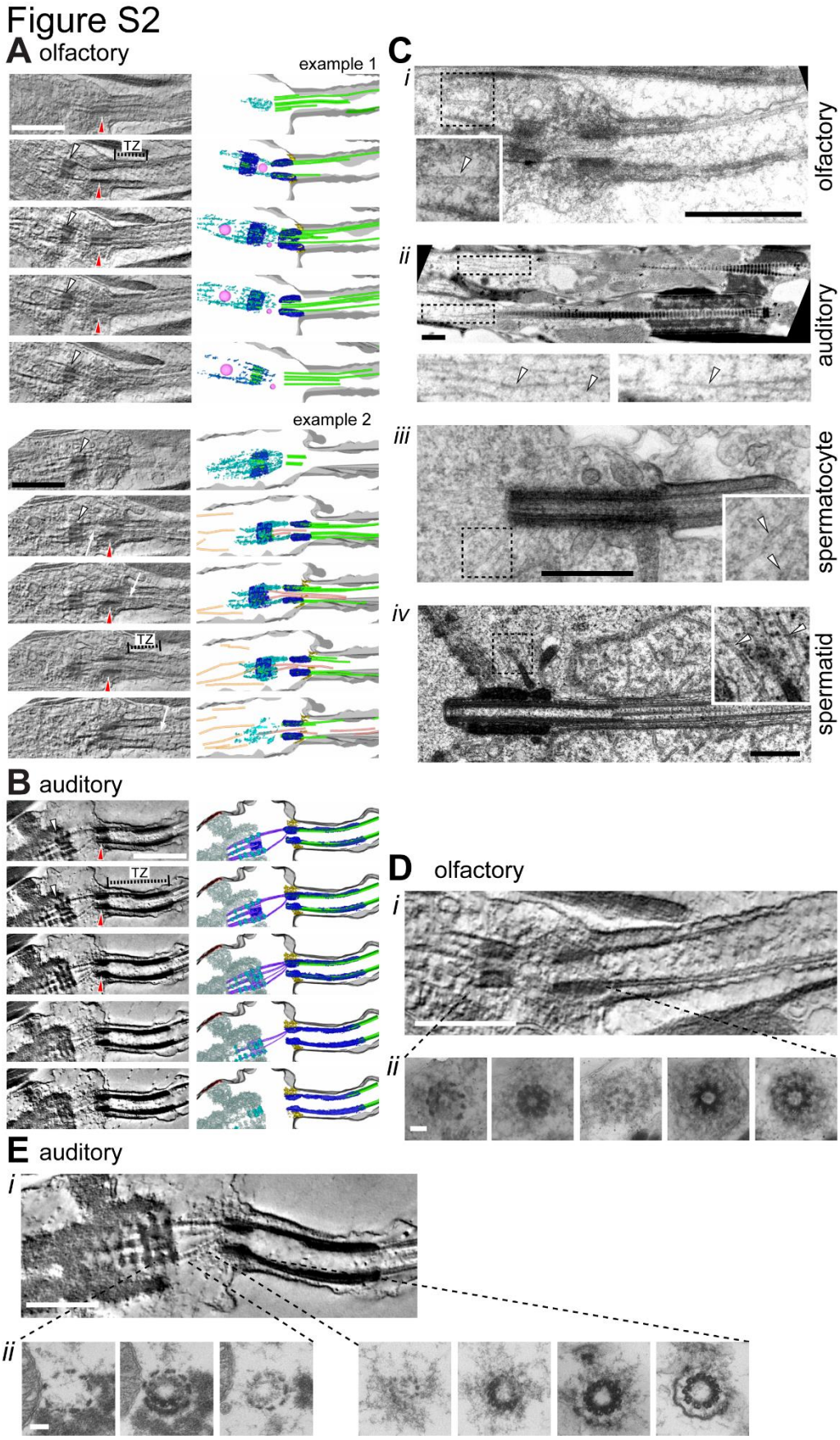

Figure S2 (related Figure 1): Different ciliary bases show both similar and variable elements (related to Figure 1 and 2**)**. A) Left: Longitudinal tomogram stills of the ciliary base

in olfactory neurons showing a proximal basal body (pBB-white arrowhead), a distal BB (dBB-red arrowhead) and the transition zone (TZ). Right: Schematic model based on and overlaying the tomogram data. Model of the BB and ciliary microtubules (light green), cytoplasmic MTs (orange) that nucleate from the BBs, MTs that nucleate from the proximal BB and extend into the cilia (brown), non-MT electron densities around BBs (dark blue), the electron densities of rootlet (cyan), vesicles at the ciliary base (magenta), connections between dBB and cell membrane (golden) and the cell/ciliary membranes (black) (see also Figure 1 and Movie M1). Based on the features at the ciliary base, olfactory neurons can be divided into two types: Type-1) where singlet MT is absent in the lumen of both the BB and TZ (example 1) and Type-2) where one or more singlet MTs (cyan) are present in the lumen of the BBs and TZ (example 2). ~70% of the olfactory neurons are of Type-1, while ~30% of them are of Type-2 (quantification not shown). B) Longitudinal tomogram stills of the ciliary base in auditory neurons showing pBB (white arrowhead), dBB (red arrowhead) and TZ. Right: Schematic model based on and overlaying the tomogram data. For auditory neurons, we modelled all the objects described in A, electron density around the MTs in TZ (dark blue), and the rootlet striations (magenta). Note that in the example 2 of olfactory cilia (A) we observed singlet microtubules (white arrows) that are bent in olfactory neurons, and the connections between the distal BB and the cell membrane are less obvious in single sections of both types of neurons, justifying the importance of collecting and analysing tomograms to model these ciliary bases. Scale bars in A and B indicate 500nm. C) Electron micrographs of different types of ciliary bases showing cytoplasmic MTs around the BB and rootlets. The regions marked with dotted squares on the micrographs are presented in the insets. D, E) Representative electron micrographs show longitudinal sections (i) and sets of serial cross sections (CS) of the marked regions (ii) of the BBs in olfactory (D) and auditory neurons (E). Note that the cartwheel is absent in all neuronal BBs. All electron micrographs in C-E represent the features that were observed in ≥3 samples. Scale bars on the longitudinal (i) and cross (ii) section micrographs are 500 nm and 100 nm, respectively.

Figure S3

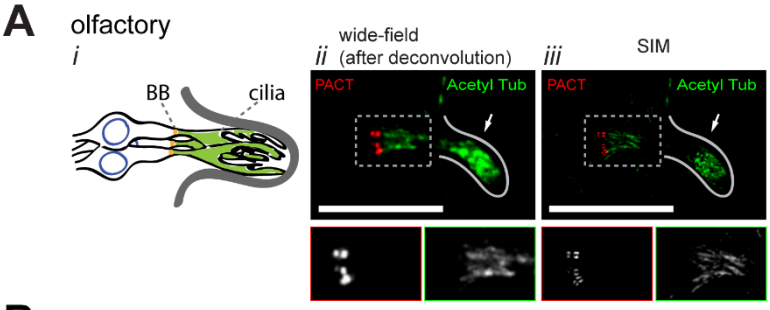

B olfactory

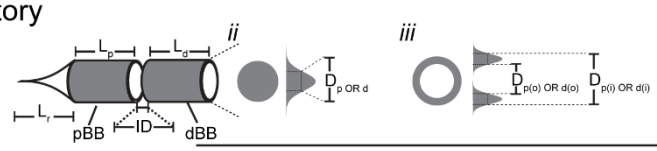

iv

	L_r	L_p	D_p	$D_{p(i)}$	$D_{p(o)}$	ID	L_d	D_d	$D_{d(i)}$	$D_{d(o)}$
PACT	---	226±32	---	82±28	321±20	138±25	253±20	---	125±10	333±36
Rootletin	1389±96	257±28	---	326±20	380±15	---	285±21	---	290±28	481±30
PLP	---	245±45	---	280±20	485±46	114±20	247±15	---	290±27	550±61
Spd2	776±104	238±41	---	316±45	457±38	---	268±45	---	335±16	445±38
γ-tubulin	---	193±36	---	197±56	372±25	---	200±53	---	311±20	588±49
Ana1	---	265±17	340±25	---	---	104±13	272±23	---	35±20	374±15
BLD10	---	246±19	184±11	---	---	88±30	253±25	178±16	---	---
SAS4	1396±114	218±25	199±17	---	---	---	240±16	196±21	---	---
SAS6	---	---	---	---	---	---	---	---	---	---
Ana2	---	---	---	---	---	---	---	---	---	---

C auditory

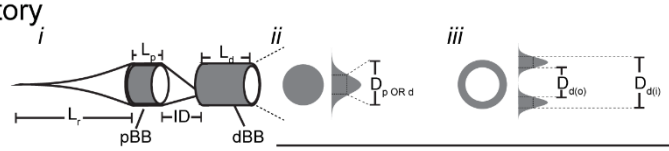

iv

	L_r	L_p	D_p	ID	L_d	D_d	$D_{d(i)}$	$D_{d(o)}$
PACT	---	120±10	135±41	182±45	207±12	---	143±20	306±29
Rootletin	2938±95	---	---	---	380±05	---	140±10	---
PLP	1769±96	---	---	---	---	---	76±14	419±21
Spd2	330±104	---	---	298±33	---	---	---	---
γ-tubulin	---	---	---	---	152±24	---	147±23	365±10
Ana1	---	180±10	213±21	298±33	263±26	---	30±19	308±15
BLD10	---	127±09	161±25	261±27	193±12	165±10	---	---
SAS4	1119±82	---	---	---	180±25	152±11	---	---
SAS6	---	---	---	---	---	---	---	---
Ana2	---	---	---	---	---	---	---	---

D

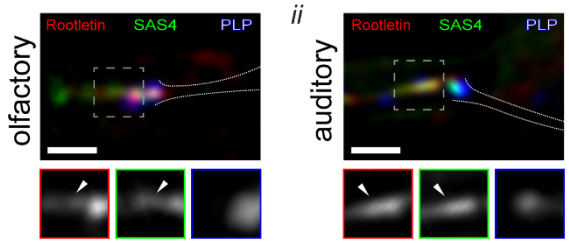

Figure S3 (related Figure 2): Quantification of the localisation patterns of rootlet, pericentriolar material (PCM) and centriolar components in different types of neurons

obtained using 3D-SIM (related to Figure 1 and 2**).** A) i) A scheme of a set of three olfactory neurons innervating *sensillum basiconica* showing BBs and cilia. Representative wild field pictures (ii) and SIM pictures (iii) showing acetylated α-tubulin and PACT, a basal body marker, in a set of three olfactory neurons. The scale bars indicate 10 µm. B, C) i) Scheme shows the olfactory (A) and auditory (B) ciliary bases with proximal (pBB) and distal (dBB) basal bodies. ii-iii) Schemes show the method of the quantification of the proteins and different parameters. iv) The length (with ±S.D.), diameter (with ±S.D.) and other variables of the defined zones are mentioned in the table. All the values mentioned in the table are in nanometer (nm). The number of samples used for each quantified value is N ≥16. The schemes (in left) representing the localisation patterns of the proteins are drawn based on the quantification shown in the right. D) Representative wild field pictures of olfactory (i) and auditory (ii) cilia showing rootletin (red), SAS4 (green) and DPLP (blue), a PCM marker. Arrow heads marks the rootlet region at the ciliary base. The scale bars indicate 1 µm.

Figure S4

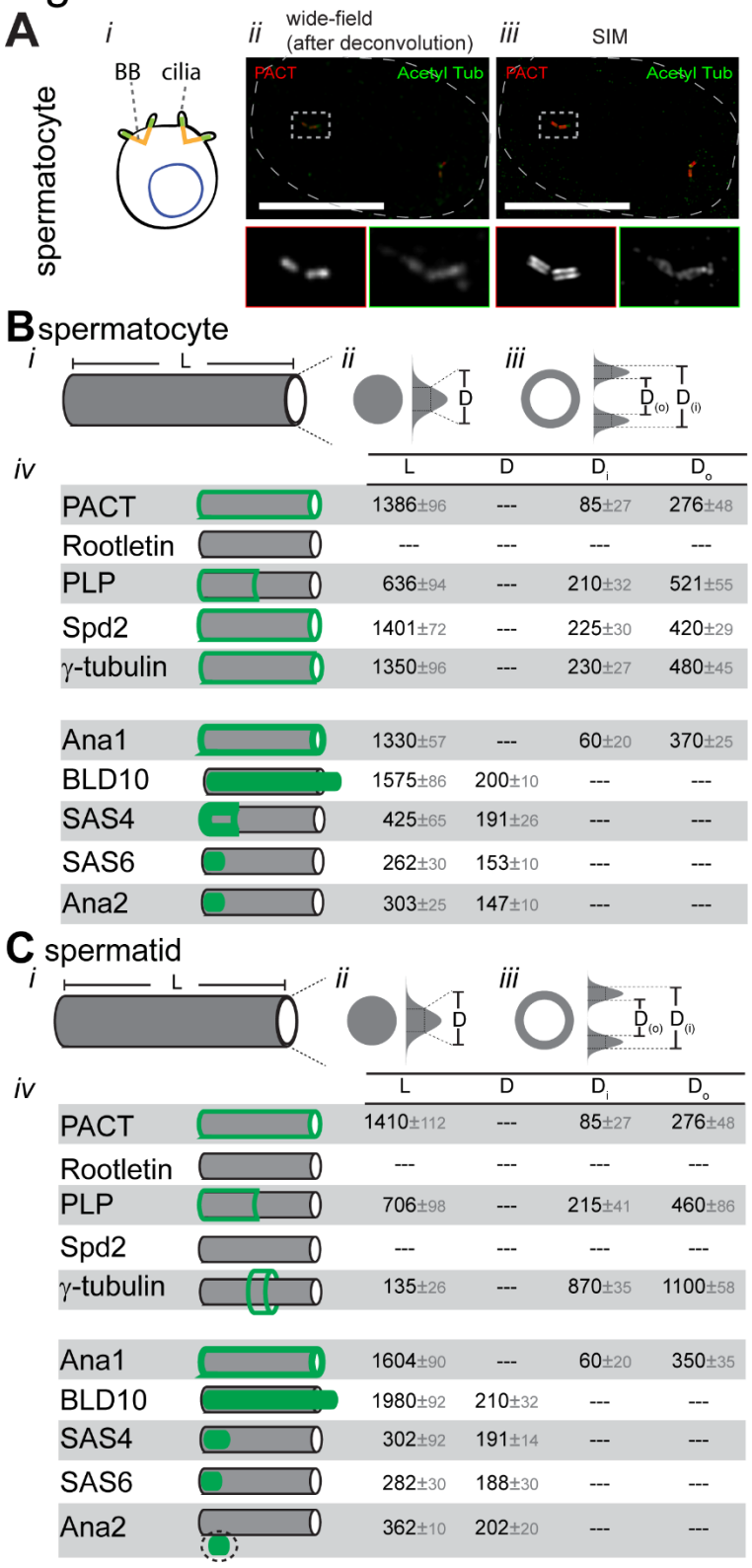

Figure S4 (related Figure 2): Quantification of the localisation patterns of rootlet, pericentriolar material (PCM) and centriolar components in sperm cells obtained using 3D-SIM (related to Figure 1 and 2**).** A) i) Scheme of a spermatocyte showing BB and primary cilia. Representative wild field pictures (ii) and SIM pictures (iii) showing acetylated α-tubulin

and PACT, a basal body marker, in a spermatocyte. The scale bars indicate 10 µm. C, D) i) Scheme shows the BB in spermatocyte (C) and spermatid (D). Schemes show the method of the quantification of the proteins and different parameters (ii, iii). iv) The length (with ±S.D.), diameter (with ±S.D.) and other variables of the defined zones are mentioned in the table. All the values mentioned are in nanometer (nm). The number of samples used for each quantified value is N ≥16. The schemes (in left) representing the localisation patterns of the proteins are drawn based on the quantification shown in the right.

Figure S5

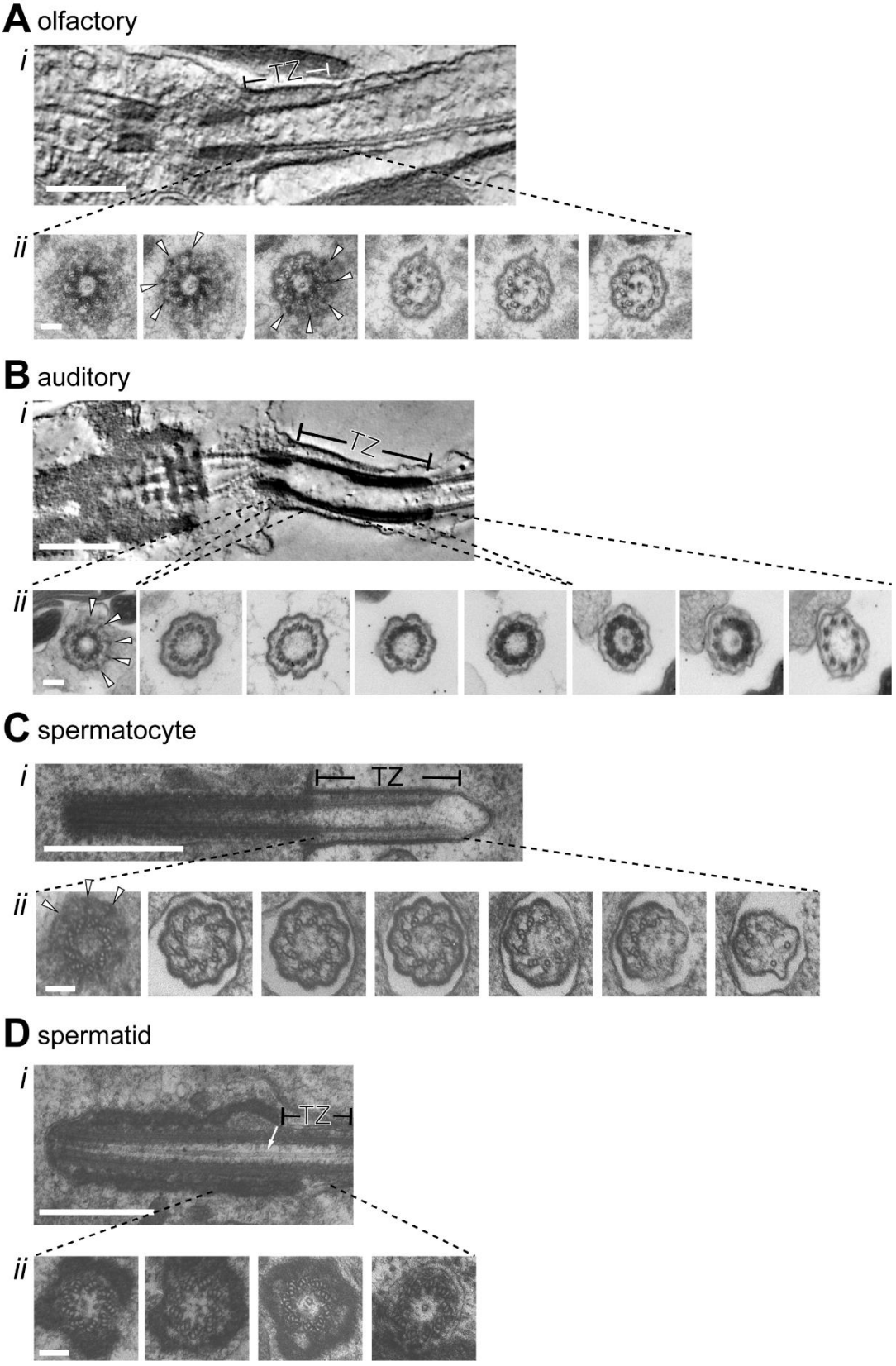

Figure S5 (related Figure 3): Both length and non-MT based structures of the transition zone vary between different cell types (related to Figure 3**).** Representative electron micrographs show longitudinal sections (i) and sets of serial cross sections (CS) (ii) of the

marked regions in the transition zone of olfactory neurons (A), auditory neurons (B), spermatocyte (C) and early elongating spermatid (D). For the cross-section series analysis, 70 nm serial sections were collected. Arrowheads mark the transition fibre (similar to distal appendage) that connect the distal tip of the basal body to the ciliary membrane. The white arrow marks the single MT in the lumen of the spermatid BB in D. The CS images in A, C and D are from serial sections of the transition zone of olfactory, spermatocyte and spermatid, respectively. The CS images in B were compiled from three different sets of serial sections. Notably, here the area that is distal to the basal body and shows electron density on and around the MTs in longitudinal sections of ciliary bases is considered transition zone (marked as TZ in the figure). The region distal to the transition zone is considered ciliary shaft (axoneme). All electron micrographs here represent the features that were observed in ≥3 samples. Scale bars on the longitudinal (i) and cross (ii) section micrographs are 500 nm and 100 nm, respectively.

Figure S6

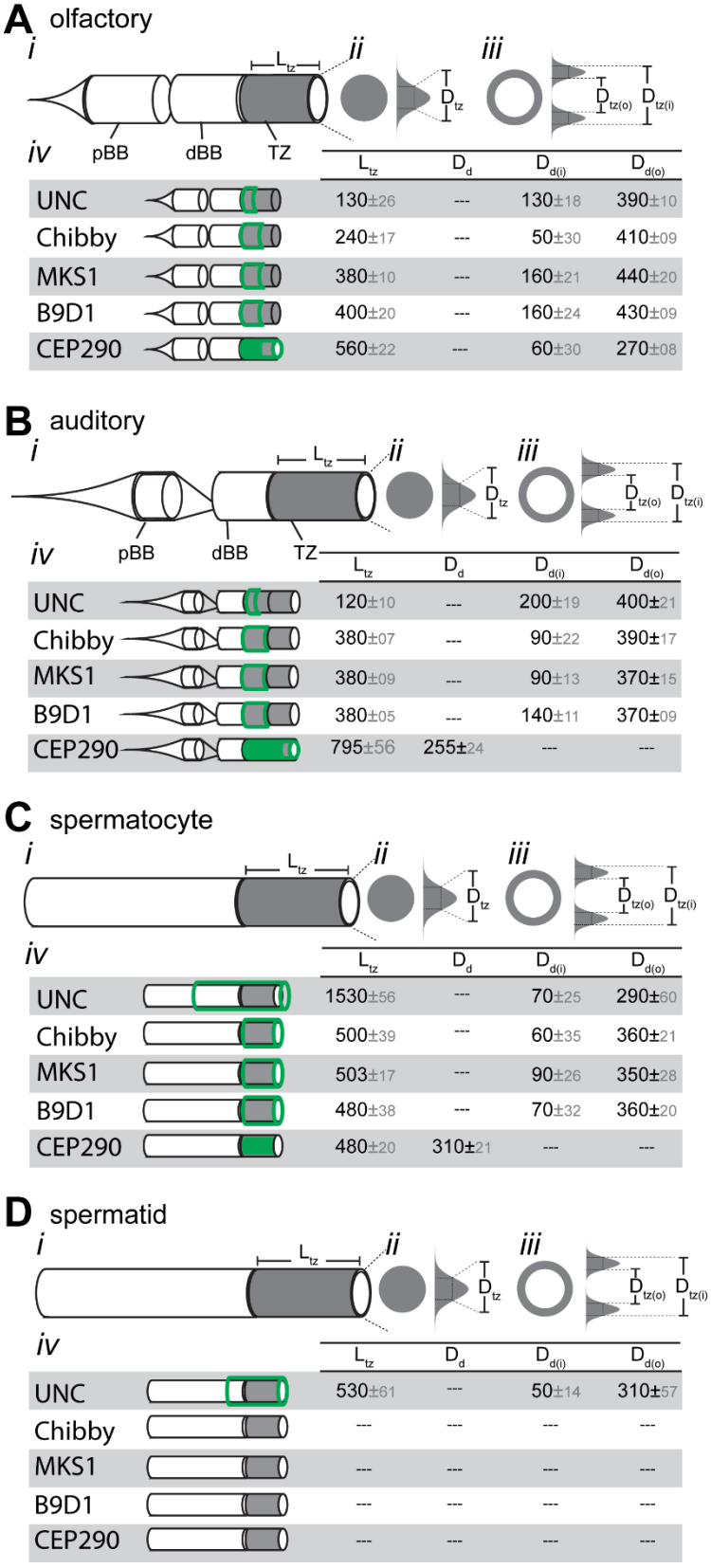

	L_{tz}	D_d	$D_{d(i)}$	$D_{d(o)}$
A olfactory				
UNC	130±26	---	130±18	390±10
Chibby	240±17	---	50±30	410±09
MKS1	380±10	---	160±21	440±20
B9D1	400±20	---	160±24	430±09
CEP290	560±22	---	60±30	270±08
B auditory				
UNC	120±10	---	200±19	400±21
Chibby	380±07	---	90±22	390±17
MKS1	380±09	---	90±13	370±15
B9D1	380±05	---	140±11	370±09
CEP290	795±56	255±24	---	---
C spermatocyte				
UNC	1530±56	---	70±25	290±60
Chibby	500±39	---	60±35	360±21
MKS1	503±17	---	90±26	350±28
B9D1	480±38	---	70±32	360±20
CEP290	480±20	310±21	---	---
D spermatid				
UNC	530±61	---	50±14	310±57
Chibby	---	---	---	---
MKS1	---	---	---	---
B9D1	---	---	---	---
CEP290	---	---	---	---

Figure S6 (related Figure 3): Quantification of the localisation pattern of transition zone proteins in different ciliated cells obtained using 3D-SIM (related to Figure 3**).** List of the

transition zone (TZ) proteins present in olfactory neurons (A), auditory neurons (B), spermatocyte (C) and early elongating spermatid (D). The schemes show BBs and TZs (i) and the method to quantitate proteins and different parameters (ii, iii). The length (with ±S.D.), diameter (with ±S.D.) and other variables of the defined zones are mentioned in the table. All the values mentioned in the table are in nanometer (nm). The number of samples for each quantified value is N ≥16. The schemes (in left) represent the localisation pattern of the proteins (drawn based on the quantitation shown on the right).

Figure S7

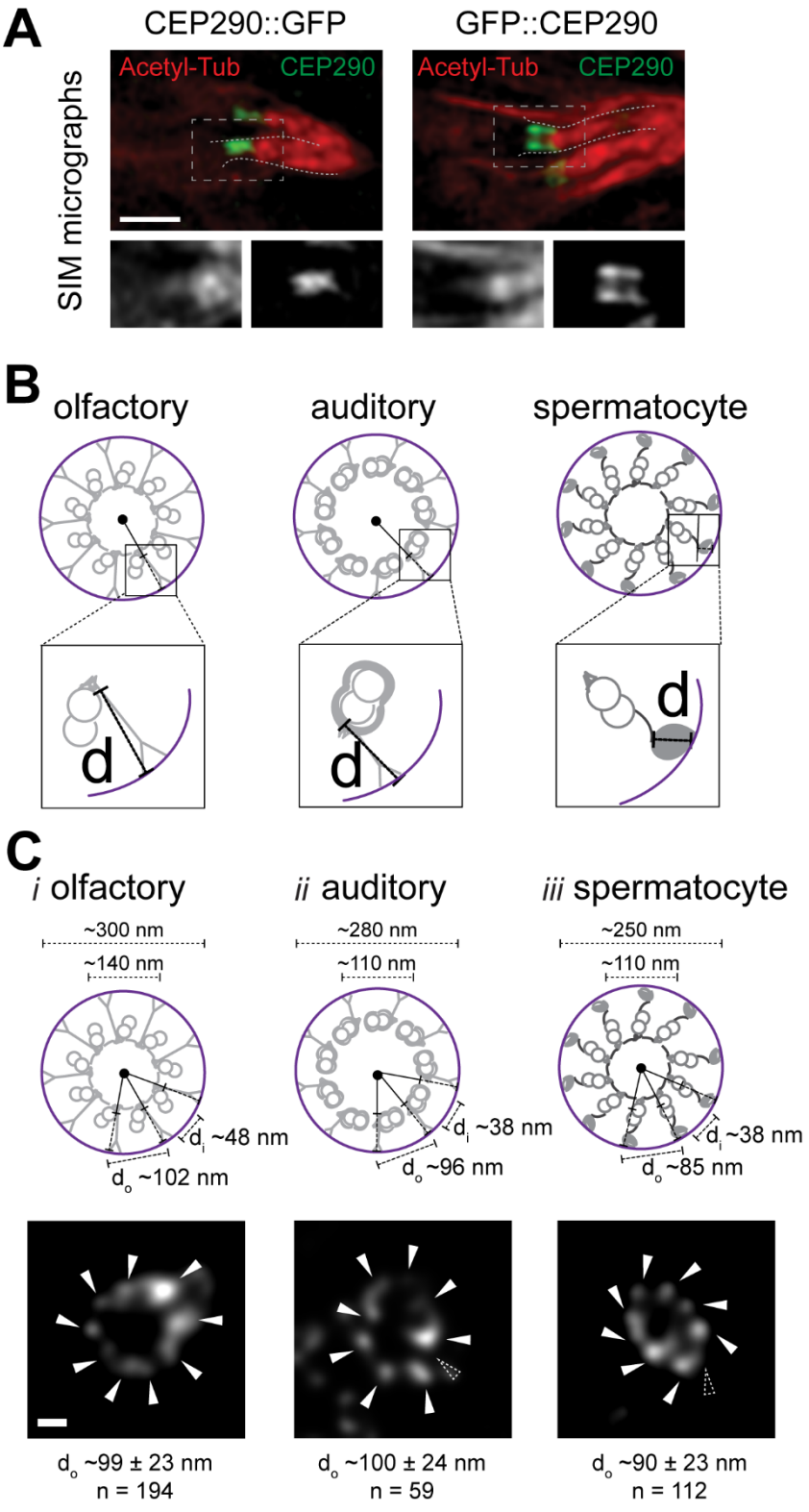

Figure S7 (related to Figure 4): Localisation analysis of GFP tagged CEP290 proteins at the TZ of neurons (related to Figure 6**).** A) Representative SIM images of the ciliary bases of olfactory neurons marked using acetylated α-tubulin (red) and ectopically expressed

CEP290::GFP (*Gal4^{cha19b}/UAS-CEP290::GFP*) or GFP::CEP290 (*Gal4^{cha19b}/UAS-GFP::CEP290*). SIM analysis shows that CEP290::GFP localises towards the lumen and on the MTs and GFP::CEP290 localises towards the ciliary membrane in the transition zone of olfactory neurons. B) Schemes show the method of measuring the distance (d) between the MT or the hook and ciliary membrane at the TZ of different ciliated cells. C) (i) Schemes show the methods of measuring the inter-distance between the outer (d_o) and inner (d_i) tips of the adjacent MT-membrane linkers. Representative STED micrographs of GFP::CEP290 in the cross-section of the transition zones of the olfactory (i), auditory (ii) and spermatocyte (iii) cilia. While the white arrowheads mark the resolved GFP foci, empty arrowheads (with dotted border) indicate the position of postulated missing foci. Scale bars in A and C represent 1 µm and 100 nm, respectively.

Figure S8

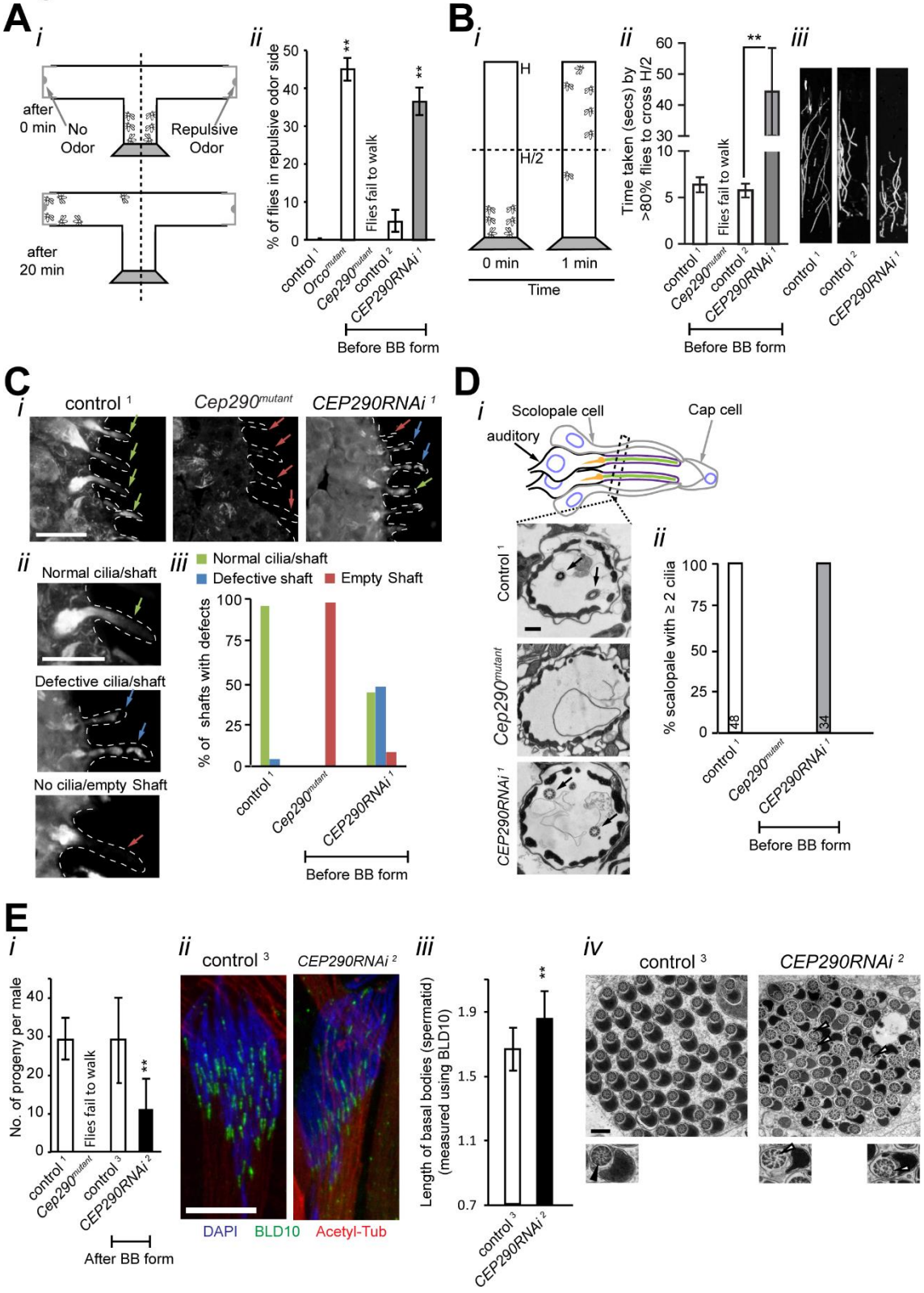

Figure S8 (related to Figure 4): CEP290 is required to form cilia in all ciliated cells in the fly (related to Figure 6**). A-D) CEP290 is required for olfactory and auditory cilia assembly, its loss affecting both smelling and negative-geotaxis walking behaviour,**

respectively, in adult flies. A) CEP290 is required for smelling in adult flies. i) The scheme shows the odour repulsion test using the T-tube to measure the ability of adult flies to detect a repulsive odour (Benzaldehyde). ii) Quantification of the percentage of flies that are in the compartment with repulsive odor. The total number of adult flies used for each histogram bar is N ≥60; 3 replicate experiments were performed. A null mutant of Orco, a co-receptor essential for olfaction, was used as a positive control. Control 1-2 are negative controls (see Table S1 and S3). B) i) Scheme depicts the bang assay and the vertical tube used to test the negative-geotaxis walking ability of adult flies in this assay. ii) Quantification of the time taken by ≥ 80% of the flies to successfully climb the half height mark of the tube (18 cm long). The total number of samples used for each histogram bar is N ≥60 adult flies; 3 replicate experiments were performed. iii) Representative kymographs of ten flies with respective genotypes followed for the first 10 seconds after the bang. We repeated all experiments in A, B for three times. C) i) Representative pictures of the olfactory cilia in flies with different genotypes (control[1], *Cep290*^{mutant} and *CEP290RNAi*^{1}). ii) Representative images of the different types of olfactory shafts that harbour normal, defective or no cilia. iii) Quantification of the ciliary defects observed in flies with different genotypes. Scale bars represent 10 µm. D) i) Representative electron micrographs of the cross section of the scolopale in the second antennal segment of flies with different genotypes. Scale bars represent 500 nm. ii) Quantification of the percentage of scolopale with two or more cilia in the flies with different genotypes. **E) CEP290 is required to regulate the BB length and flagella assembly in sperm cells thus affecting the male fertility.** i) Quantification of the number of progeny produced per male with different genotypes. The total number of males used for each histogram bar is N ≥10. We repeated the male fertility experiments twice. ii) Representative pictures of the BBs in the spermatids marked using BLD10, a centriolar protein, in flies with different genotypes. DNA, BB and sperm flagella are marked by DAPI (blue), BLD10 (green) and acetylated tubulin (red), respectively. Scale bars represent 10 µm. iii) Quantification of the length of BBs marked using BLD10 as shown in (ii). The number of BBs quantified for each genotype is N ≥ 90. We repeated this experiment for three times. iv) Representative cross-section micrographs show the axoneme bundle of the elongating flagella in control[3] and *CEP290RNAi*^{2} flies. Note that while the 9+2 arrangement of the MTs was normal in control[3] flies, the MT arrangement was defective in *CEP290RNAi*^{2} flies (see insets). Scale bars represent 500 nm. For a detailed list of genotypes of different flies, including negative controls see Table S1 and S3. Error bars indicate ± S. D. (*-$p<0.01$ and **-$p<0.001$ estimated using the Mann-Witney U-test).

Figure S9

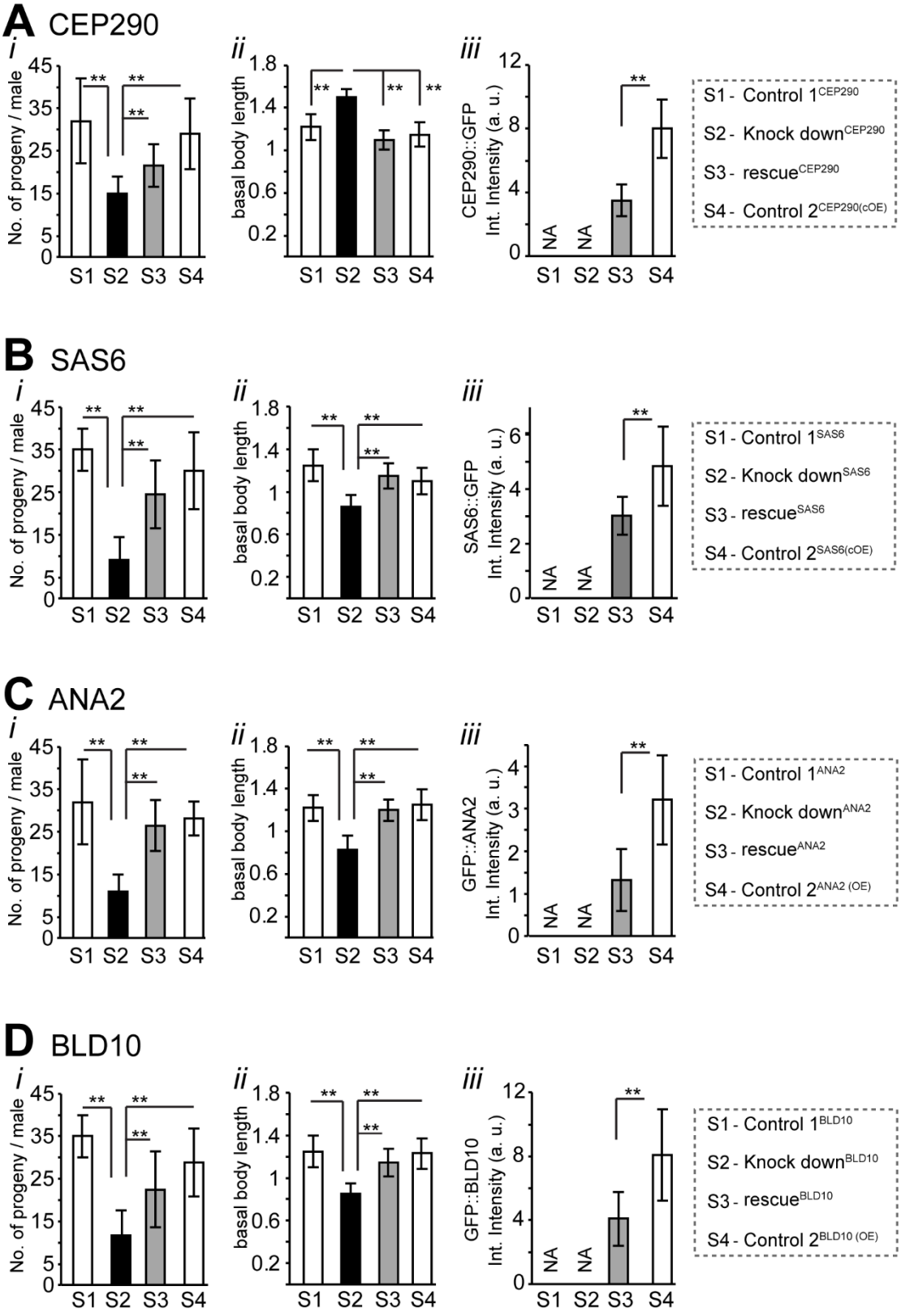

Figure S9 (related to Figure 4-6): Controls for the specificity of the RNAi tools used in this manuscript. Quantification of the number of progeny produced per male (i), length of the

BBs (ii) and total GFP intensity of the candidate protein at the BB. CEP290 (A), SAS6 (B), ANA2 (C) and BLD10 (D). Here, for each candidate (X) gene S1, S2, S3 and S4 represent the flies with ectopic-expression of UAS-mCD8GFP (Control 1), RNAi (knock down), UAS-X-GFP in RNAi background (rescue) and UAS-X-GFP in wild type background (Control 2). While for A-Di the total number of males used for each histogram bar is N ≥10, for A-Dii and iii, the number of BBs quantified for each genotype is N≥120 and ≥60, respectively. We repeated all experiments described in this figure twice. NA indicates not applicable. For a detailed list of genotypes see Table S1 and S3. Error bars indicate ± S. D. (**-p<0.001 estimated using the Mann-Witney U-test). Note that we rescued the knock down phenotypes of all candidate molecules (SAS6, ANA2, CEP290, and BLD10) both for basal body length (ii) and male fertility (i). We further quantified the protein depletion (iii) in RNAi experiments in sperm cells for all candidates. Altogether, this analysis shows the specificity of the tools we used.

Figure S10

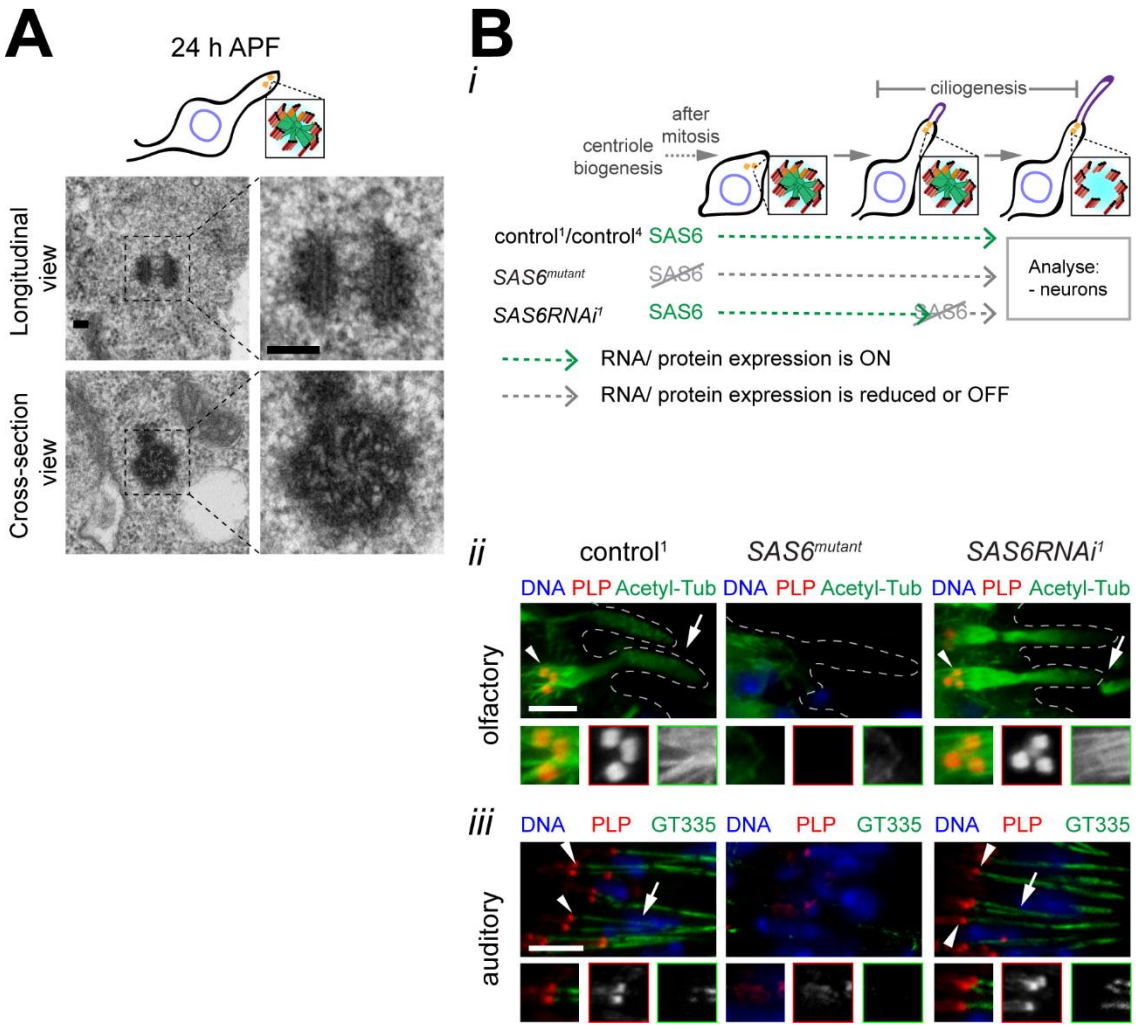

Figure S10: SAS6 is essential for centriole assembly in neurons, but is not required for neuronal cilia function. A) Representative electron micrographs show longitudinal and cross sections through the centrioles in olfactory neurons (before ciliogenesis: at 24 h APF) in wild type flies. Note that those centrioles are close to the cell membrane and have a cartwheel. **B)** i) Schematic representation of the experimental setting used to reduce/remove SAS6 during centriole and cilia biogenesis in neurons. ii) Representative images show olfactory and auditory neurons in flies with different genotypes. Cilia in olfactory and auditory neurons were studied using anti-acetylated tubulin (green) and anti-glutamylated tubulin (green) antibody, respectively. PLP (red, centrosomes) and DAPI (blue, DNA). Arrowheads mark BBs and arrows mark cilia. Scale bars represent 5 µm. We repeated all experiments in B for three times.

Figure S11

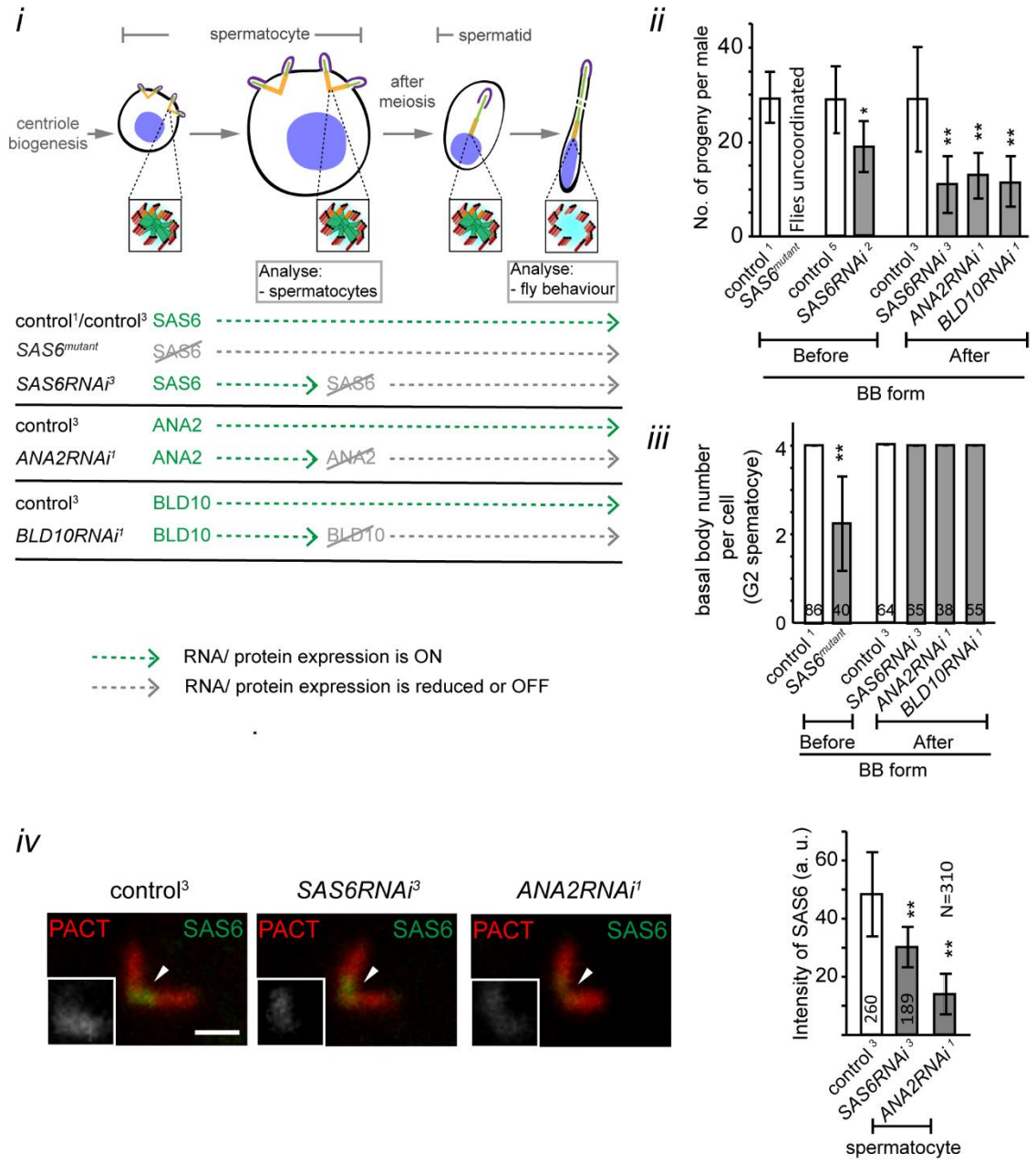

Figure S11: Both SAS6 and ANA2 are required for BB elongation in sperm cells, being important for male fertility. i) Schematic representation of the experimental setting used to reduce/remove SAS6 before and after centriole biogenesis in sperm cells. ii) Quantification of the number of progeny produced per male with different genotypes. The total number of males used for each histogram bar is N ≥10 (the experiment was repeated twice). iii) Quantification of the number of BBs per cell in mature spermatocytes. iv) Representative images of mature BB spermatocyte of flies with different genotypes (control^{3}, *SAS6RNAi*^{3} and *ANA2RNAi*^{1}). RFP::PACT (red) marks BBs and Anti-SAS6 antibody (green) stains the proximal part of the centriole. Insets show SAS6 (green) close to the arrowhead (in grey scale). Scale bars in (iv)

represent 1 µm. Graph shows quantification of the total amount of SAS6 at the BBs in mature spermatocytes of the different genotypes. We repeated all experiments in iv for three times. Sample number is mentioned on the histogram bar in iii and iv. For a detailed list of fly genotypes see Table S1 and S3. Error bars indicate ± S. D. (*-$p<0.01$ and **-$p<0.001$ estimated using the Mann-Witney U-test).

Figure S12

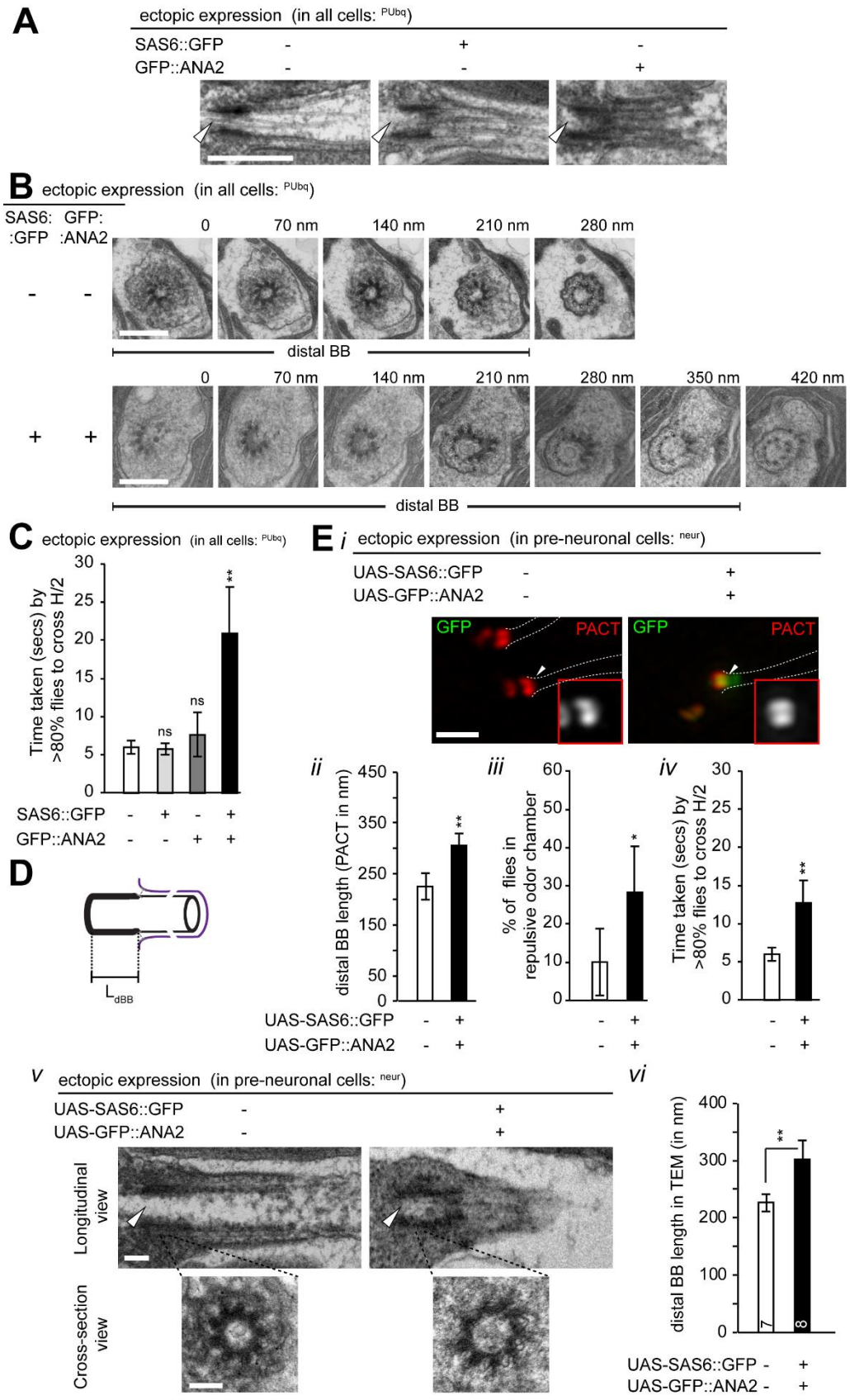

Figure S12: SAS6 and ANA2 cooperate to elicit ectopic basal body elongation in sensory neurons, leading to defects in sensory behaviour. A) Representative electron

micrographs of longitudinal sections through the ciliary base of olfactory neurons in flies with different genotypes. Empty arrow head marks the proximal region of the distal basal body without cartwheel. B) Representative electron micrographs of cross sections through the distal BB of olfactory neurons in flies with either no ectopic expression or the simultaneous ectopic expression of both SAS6 and ANA2. C) Quantification of the time taken by ≥80% of the flies to successfully climb the half way mark of the tube (18 cm long). The number of flies used for each histogram bar in each experiment is a total of N=60; 3 replicate experiments were performed. D) Schemes show the method of measuring the length of distal basal body (L_{BB}). E) Representative SIM images present the longitudinal view of the basal bodies in flies with different genotypes. PACT (red) marks the basal bodies (BBs) in the neurons. Insets show PACT (red) close to the arrowhead (in grey scale). Quantification of basal body length (ii), olfactory reception (iii) and negative-geotaxis (iv) behaviour in flies with either no ectopic expression or ectopic expression of both SAS6 and ANA2 using a driver that only expresses in pre-neuronal cells. The number of distal basal bodies analysed in this experiment (ii) is a total of N≥45. The SIM results (Ei and ii) were observed in three independent experiments. The number of flies used for each histogram bar in each experiment (in iii and iv) is a total of N=60; 3 replicate experiments were performed. Note that upon ectopic expression of both SAS6 and ANA2 in pre-neuronal cells, we observed one cilium per cell, in most of the olfactory neurons (98%), as shown in figure and as observed in controls. In the remainder olfactory neurons (not shown), we observed that cells were forming two cilia, each with one basal body. (v) Representative electron micrographs show longitudinal sections through the ciliary base and cross sections through the distal BB of olfactory neurons in flies with different genotypes. The empty arrow head marks the proximal region of the distal basal body without cartwheel. The representative electron micrographs of the cross sections of distal basal bodies present the features (including 9-fold symmetric doublet MTs) of N≥10 neurons for each genotype. vi) Quantification of the distal BB length using electron micrographs in olfactory neurons. The TEM results (A, B and Ev) were observed in two independent experiments. Scale bars in A, B, E*i*, and E*v* represent 0.5, 0.2, 1 and 0.1 µm, respectively. Error bars indicate ±S. D. (significance in the difference between sample populations were estimated using the Mann-Witney U-test). ** and * indicate $p < 0.001$ and $p < 0.01$, respectively. For a detailed description of the fly genotypes used see Table S3.

Figure S13

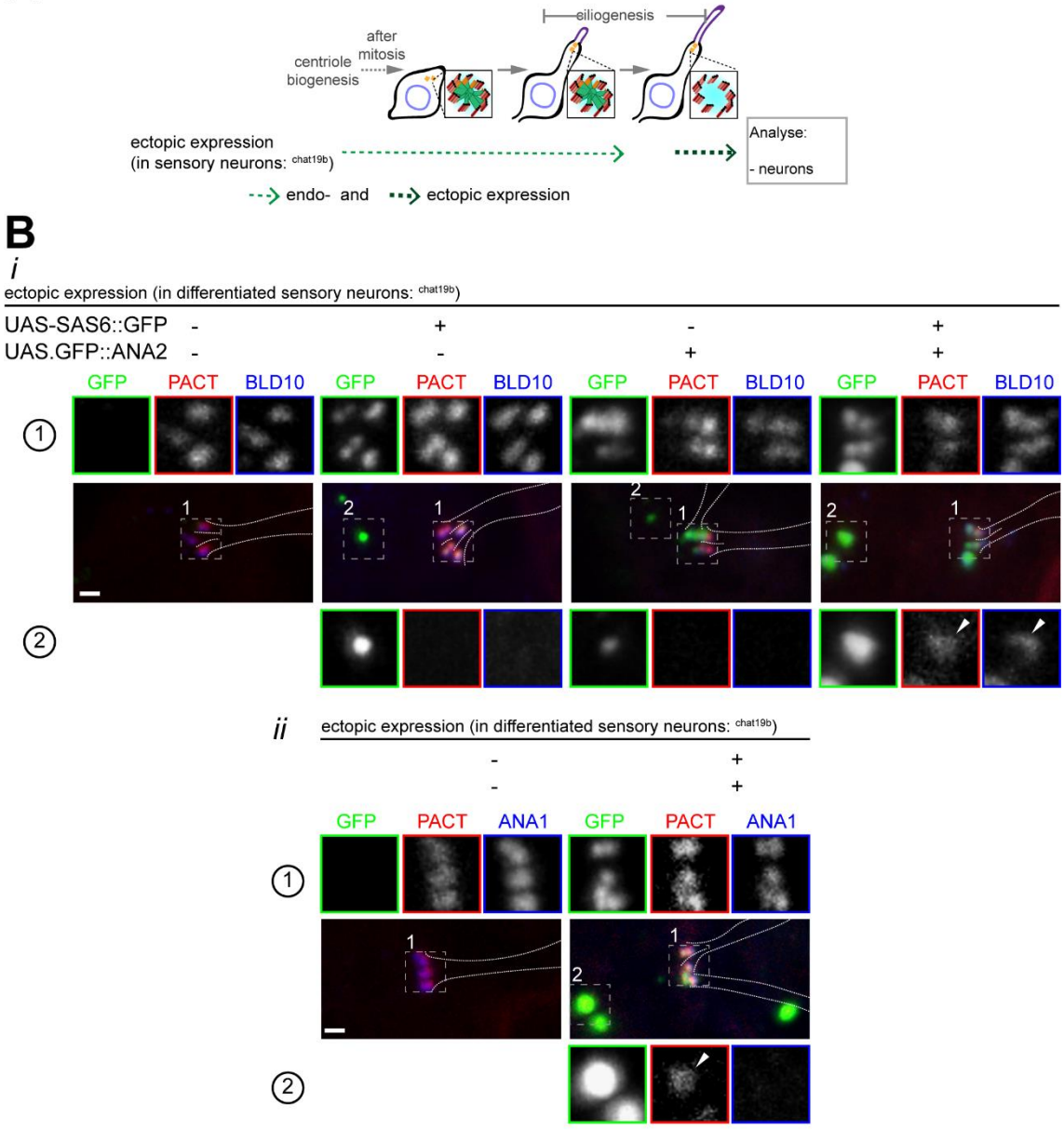

Figure S13: SAS6 and ANA2 recruit BLD10/CEP135. A) Schematic representation of the experimental setting used to ectopically express SAS6 and ANA2 after basal body docking in the neurons. B) Representative images of neuronal BBs and cell bodies of flies with different genotypes. We analysed RFP::PACT (red) that marks BBs and some centrosomal components, such as Anti-BLD10 and -ANA1 antibodies (blue). Insets marked 1 show the region around the BBs, while insets marked 2 show cell bodies with accumulation of GFP (either SAS6 or ANA2 or both of them). Scale bars represent 1 µm, respectively.

Movie Legends

Movie M1: Structures of the ciliary base in olfactory neurons (related to Figure 1**)**. The movie shows a reconstructed tomogram (built by stitching three serial tomograms) segmenting both the basal bodies, rootlet, transition zone and proximal part of the ciliary shaft in the longitudinal view. The BB and ciliary microtubules (light green), cytoplasmic MTs (orange) that nucleate from the BBs, MTs that nucleate from the proximal BB and extend into the cilia (brown), non-MT electron densities around BBs (dark blue), the electron densities of rootlet (cyan), vesicles at the ciliary base (magenta), connections between dBB and cell membrane (golden) and the cell/ciliary membranes (black) were modelled. The electron densities (dark blue) around the basal bodies are removed between frame number 94 and 136 to better visualise the MTs of the basal bodies. Also, note that electron densities around the MTs in the transition zone are not modelled in this move. Furthermore, the tomogram shows the longitudinal view of the ciliary base of two olfactory neurons that are adjacent to each other (for snapshots of different z- slices with labels see also Figure 1A*i* and S2A).

Movie M2: Structures of the auditory ciliary base (related to Figure 1**)**. The movie shows a reconstructed tomogram highlighting the basal bodies, rootlet, transition zone and proximal part of the ciliary shaft in the longitudinal view. We modelled the BB and ciliary microtubules (light green), non-MT electron densities around BBs (dark blue), the electron densities of rootlet (cyan), thin fibres of the rootlets (violet), connections between the electron densities around rootlet and cell membrane (red), connections between dBB and cell membrane (golden) and the cell/ciliary membranes (black) (see also Figure 1 and S2B). The electron densities (dark blue and cyan) around the basal bodies are removed between frame number 93 and 135 to better visualise the MTs of the distal basal body and electron density (dark blue) around proximal basal body. Note that though we were successful in modelling the distal BB, we were unable to model the MTs in the proximal BB in this tomogram (for snapshots of different z- slices with labels see also Figure 1B*i* and S2B).

Movie M3: The proximal basal body of olfactory neurons is composed of radially symmetric nine MT doublets (related to Figure 2**)**. The movie shows the reconstructed tomogram highlighting the MT doublets, electron densities around the MTs and the rootlet in the cross-sectional view. The A- (light green) and B- (dark green) tubule of the MT doublets, non-MT electron densities around the MT doublets (dark blue) and the electron densities of rootlet (cyan) were modelled. Note that we did not observe any cartwheel-like structures at the proximal part of the basal body in this tomogram.

Movie M4: Nine radially symmetric MT doublets are found in the olfactory distal basal body (related to Figure 2**)**. The movie shows the reconstructed tomogram segmenting the MT doublets, electron densities around the MTs in the cross-sectional view. We modelled the A-tubule of the MT doublets (light green), B-tubule of the MT doublets (dark green), non-MT electron densities around the MT doublets (dark blue) and the cell/ciliary membranes (black). In this tomogram, we did not find any cartwheel-like structures at the proximal part of the basal body.

Movie M5: The proximal basal body of auditory neurons is composed of a mixture of nine MT singlets and doublets (related to Figure 2**)**. The movie shows the tomogram segmenting the MT singlets and doublets, electron densities around the MTs and the rootlet in the cross-sectional view. The A- (light green) and B- (dark green) tubule of the MT doublets, non-MT electron densities around the MT doublets (dark blue) and the electron densities of rootlet (cyan) were modelled. Though we could not model the proximal BB in this longitudinal tomogram, we found a proper proximal basal body that was composed of a mixture of nine MT singlets and doublets. Interestingly, all MTs are encapsulated with highly electron dense materials. Moreover, we did not observe any cartwheel-like structures in this basal body in this tomogram.

Movie M6: Nano-structures in the distal basal body of auditory neurons are nine-fold symmetric (related to Figure 2**)**. The movie shows the reconstructed tomogram highlighting the MT doublets, electron densities around the MTs in the cross-sectional view. We modelled the A- (light green) and B- (dark green) tubule of the MT doublets, non-MT electron densities around the MT doublets (dark blue) and the cell/ciliary membranes (black). We did not observe any cartwheel-like structures at the proximal part of the basal body in this tomogram.

Movie M7: Nine-fold symmetric nano-structures are found in the olfactory transition zone (related to Figure 3**)**. The movie shows the tomogram segmenting the MT doublets, electron densities around the MTs, the linker between the doublets (MT-MT linkers) and the linkers connecting the MT doublets and ciliary membrane (MT-membrane linkers) in the cross-sectional view. We modelled the A- (light green) and B- (dark green) tubule of the MT doublets, non-MT electron densities around the MT doublets and the MT-MT linkers (dark blue), the MT-ciliary membrane linkers (magenta) and the cell/ciliary membranes (black). The tomogram shows that the MT-MT linkers (dark blue) and MT-membrane linkers (magenta) are nine-fold symmetric, and the MT-membrane linkers (magenta) connect the electron densities around the A-tubules and ciliary membrane.

Movie M8: The transition zone of auditory neurons is composed of nine radially symmetric MT doublets and nano-structures (related to Figure 3**)**. The movie shows the reconstructed tomogram marking the MT doublets, electron densities around the MTs, the linker between the doublets (MT-MT linkers) and the linkers connecting the MT doublets and ciliary membrane (MT-membrane linkers) in the cross-sectional view. The A-tubule of the MT doublets (light green), B-tubule of the MT doublets (dark green), non-MT electron densities around the MT doublets and MT-MT linkers (dark blue), electron density between A- and B-tubule of the doublets (orange), the MT-ciliary membrane (magenta) and the cell/ciliary membranes (black) were modelled. We observed that the MT-MT linkers (dark blue) and MT-membrane linkers (magenta) are nine-fold symmetric, and the electron densities around the B-tubules and ciliary membrane are connected by the MT-membrane linkers (magenta).

Material and Methods

Drosophila stocks and culturing

All the fly stocks used in this study are described in Table S1 and listed in the Flybase (www.flybase.org). They were reared at 25 ºC on standard corn meal media [1]. To generate transgenes, CEP290-GFP and GFP-CEP290 were cloned into a Gateway pUASp attB vector (DGRC, USA). cDNA of CEP290 was prepared from the mRNA extract of adult w^{1118} fly heads. These transgenes were generated using random insertion transgenesis system. For insertions of both transgenes (p*UASp-CEP290-GFP* and p*UASp- GFP-CEP290*), one integration in the fly genome was chosen. All flies were reared according to standard procedures and maintained at 25ºC. Please see Table S1 for information on other flies used in this study.

Immunostaining, imaging and image analysis

For sensory neurons: 1-day old adult *Drosophila* heads were dissected, sectioned in a cryo-microtome (Leica, Germany) and fixed following standardised protocols. 10-15 µm sections were laid on a poly-D-Lysine coated cover glasses or slides and fixed in 4% formaldehyde solution for 30 minutes at room temperature. Then, sections were stained using different primary antibodies (see Table S2 for detailed list) and secondary antibodies (Abcam, USA) following the published method [1, 2]. Stained sections were mounted in Vectashield mounting media (Vector Laboratories) and they were examined in microscopes. Given that *Drosophila* has different types of olfactory and auditory neurons, we always imaged the cilia innervating sensilla type B2/3 in the adult third antennal segment and chordotonal neurons in the adult second antennal segment, respectively. While the olfactory cilia innervating sensillum type

B2/3 is required to sense general food odours, the auditory neurons in the antennal second segment are essential for hearing and negative-geotaxis walking [3-5].

For sperm cells: Testes from adult flies were dissected in testes buffer, transferred to poly-L-lysine glass slides and snap frozen in liquid nitrogen as previously described [1]. Then, testes were stained using different primary antibodies (see Table S2 for detailed list) and secondary antibodies (Abcam, USA) following the published method [1]. Samples were mounted in Vectashield mounting media (Vector Laboratories) and they were examined in microscopes. Given that *Drosophila* has different stages of spermatocytes and spermatid, we focused on the mature, large G2 spermatocytes and early elongating spermatids, respectively.

For Super-resolution imaging, samples were collected on poly-L-lysine coated high precision coverslips. All structured-illumination images (SIM) were collected using either Deltavision OMX V3 (GE Healthcare Life Sciences, USA) or Elyra Super-Resolution Microscope (Zeiss, Germany) and Stimulated emission depletion (STED) images were collected using Abberior confocal STED microscope (Abberior, Germany) with QUAN scanner. In this study, an oil-immersion Plan-Apo 1.4NA DIC-grade objective and the 640/775nm combination of lasers was used. The doughnut profile (2D STED) is generated by phase modulation on a spatial light modulator (Abberior easySTED module). Detectors are avalanche photodiodes which were gated to reject the confocal baseline signal. Confocal images were collected using Leica TCS SP 5X (Leica Microsystems, Germany). While all SIM images collected using Elyra were reconstructed in Zen Blue software (Zeiss, Germany), STED images were deconvolved using Huygens Software (SVI, Netherlands). All images are then processed in ImageJ (USA) and Adobe Photoshop (Adobe Systems, USA). Also, note that we determined the direction and the boundary of the cilia (marked in dotted lines in SIM micrographs) based on the background fluorescence of one of the two fluorophores in the respective raw epifluorescence micrographs.

Transmission Electron Microscopy and serial section analysis

Antenna and testes samples were dissected, fixed, processed for chemical fixation, mounted and polymerised in resin following the published method [1, 6]. Serial thin sections (60–80 nm) were cut in a Leica Reichert Ultracut S ultramicrotome, (Leica Microsystems, Germany) collected on formvar-coated copper slot grids, and stained with 2% uranyl acetate and Reynolds lead citrate (Hayat, 1989, for detail description of the protocol, see [1]). Samples were examined and photographed at 120 kV using a Hitachi 7650 electron microscope. Finally, the images were processed in ImageJ (USA) and Adobe Photoshop (Adobe Systems, USA).

Electron Tomography and Image Analysis

Serial sections (130–150 nm) were collected onto formvar-coated copper slot grids. The sections were layered with 10 nm diameter colloidal gold particles (concentration of 1:50 µL) for 3 min on each side and washed three times. Sections were then stained with 2% uranyl acetate and Reynolds lead citrate. Single axis tilt series of basal bodies and cilia were collected at **±** 55°tilt angles with 1° increments, at 100 kV using a Hitachi 7650 electron microscope. The IMOD package 4.7.13 was used for tomogram generation and 3D modelling [7]. In IMOD, tilt series were aligned using a fiducial model based on the position of gold particles. Volumes were reconstructed using Filtered Back Projection. In 3dmod, contours were created for each object. The microtubules were identified both in the Zap and Slicer window. The electron densities were modelled using isosurfaces. We modelled only those structures that were observed in ≥3 samples (in serial sections and tomograms). The colours selected for each object were kept for all the different 3D models to allow the comparison of structures. Images from the tomogram and 3D model were collected as tiff files for each sample and recorded as an uncompressed movie at 5fps using ImageJ.

Fluorescence Recovery After Photo-bleaching (FRAP) assay

FRAP experiments were performed on an Andor Spinning-disk microscope (Nikon, Germany) equipped with a 63x 1.4 NA objective lens. For analysis of the FRAP data, two pre-bleach time-lapse images were acquired using 20% of 488nm laser power at 1-second interval. Then a rectangular ROI covering the entire centriole was bleached employing 80% laser power for 2 seconds. The post-bleach fluorescence recovery was recorded in a series of time-lapse images acquired every 1 second at 20% laser illumination for a period of 2 minutes. The data was normalised to the fluorescence before bleaching. Fluorescence recovery was quantified as Percent recovery of fluorescence, as shown below:

$$\% \text{ Fluorescence Recovery} = (F_t - F_a) * 100/(F_b - F_a)$$

F_b and F_a indicate intensities before and after photo-bleaching, while Ft is the fluorescence intensity recovered at time t. The sum of intensities of all pixels in the ROI was used for calculations.

Negative-geotaxis (bang) assay

2-4 days old adult flies were counted, collected and placed into standard vials containing food. 10 flies were transferred to a long cylinder (with a cap on top of it- see Figure 5 and S8), and there they were kept undisturbed for 10 minutes to acclimate to the environment. The cylinder was sharply tapped down on the surface of the bench three times, ensuring that the taps were

hard enough to knock down all the flies to the bottom of the cylinder. The movement of the flies was recorded for 1 minute, excluding the tapping of the cylinder. This process was repeated for two more times. For the analysis of negative-geotaxis assay, the time taken by ≥ 80% of the flies to successfully climb the half height mark of the tube (18 cm long) were counted. For each genotype, ≥60 flies were analysed. The Mann-Witney U-test was performed on different groups of flies comparing the mean percentage of flies that climbed more than half of the height of the cylinder.

Odor Repulsion (T-maze) Assay

Ten 2-4 days old flies were transferred to a T-shape tube (see Figure S8), where they were kept undisturbed for 10 minutes to acclimate to the environment. The caps of left and right arms were quickly replaced with new caps with ´NO odor´ and ´benzaldehyde´ (a repulsive odor), respectively. After 20 minutes, the number of flies in both control and odor arm were counted. This process was repeated for two more times in fresh tubes. For the analysis of odor repulsion assay, a percentage of the flies that were in the odor arm after 20 minutes were counted. For each genotype, ≥60 flies were analysed. The Mann-Witney U-test was performed on different groups of flies.

Male fertility tests

Fertility tests were performed by crossing single males with three wild-type females during 3 days. The progeny per tube was scored and averaged for 10–20 males for each genotype.

Statistical Methods

We used the Mann-Whitney tests for all statistical analysis, and most of the experiments were independently repeated for three times. For the quantifications using TEM images, we independently repeated the experiments for two times. All error bars in the histogram bars present standard deviations (S. D.). ns, * and ** indicate not significant, $p<0.01$ and $p<0.001$, respectively. For details about the number of samples used for each genotype of flies see the respective figure legends.

Supplemental Tables

Table S1: Information about the flies used in this study.

Genotypes of the flies	References	Comments
yw; Ubq-GFP::PACT; +	[8]	Marks centrioles/basal bodies
w^{1118}; Ubq-RFP::PACT;+	[6]	Marks centrioles/basal bodies
w^{1118}; +; Ubq-RFP::PACT	this study	Marks centrioles/basal bodies
w^{1118}; Endo-Rootletin::GFP;+	[9]	Note that all flies that are tagged as “Endo” in this list are P-element insertions of transgenes with the specific genomic DNA (with the endogenous promoter and the given gene), and the coding sequence for GFP
w^{1118}; Endo-Ana1::GFP;+	[10]	
w^{1118}; Endo-BLD10::GFP;+	[10]	
w^{1118}; Endo-SAS4::GFP;+	[10]	
w^{1118}; Endo-SAS6::GFP;+	[10]	
w^{1118}; Endo-UNC::GFP;+	[11]	
w^{1118}; Endo-Chibby::GFP;+	[4]	
w^{1118}; Endo-MKS1::GFP;+	[12]	
w^{1118}; Endo-B9D1::GFP;+	[12]	
w^{1118}; Endo-CEP290::GFP;+	[12]	
w^{1118}; +, $Cep290^{mecH}$/TM6Tb	[12]	Cep290 mutant
w^{1118}; +; PBacCG15524 ^{c02901}/TM6Tb	[13, 14]	SAS6 mutant
w^{1118}; +; Df(3R)$Excel^{6213}$/TM6Tb	[13]	Deficiency stock fails to complement SAS6 mutant phenotype
w^{1118}; +; $neur^{Gal4}$/MKRs	[15]	BDSC Stock, ID 6393

w^{1118}; cha19b^{Gal4}/CyO;+	[16]	BDSC Stock, ID 6798
w^{1118}; hsp83^{Gal4}/CyO;+	[17]	
w^{1118}; bam^{Gal4}/CyO;+	[18]	
W^{1118}; UASp-CEP290::GFP;+	this study	
W^{1118}; +; UASp-GFP::CEP290	this study	
w^{1118}; UAS-CEP290RNAi; +	[19]	VDRC stock, ID 47442
w^{1118}; +; UAS-SAS6RNAi	[19]	VDRC stock, ID 25073
w^{1118}; +; UAS-Ana2RNAi	[19]	VDRC stock, ID 44358
w^{1118}; +; UAS-BLD10RNAi	[19]	VDRC stock, ID 14194
w^{1118}; UAS-mCD8::GFP;+	[20]	BDSC Stock, ID 32186
w^{1118}; +; UAS-mCD8::GFP	[20]	BDSC Stock, ID 32185
w^{1118}; Ubq-SAS6::GFP;+	[21]	
yw; Ubq-GFP::ANA2; +	[21]	
w^{1118}; UAS-SAS6::GFP;+	this study	
w^{1118}; +; UAS-GFP::ANA2	this study	Gift from J. Raff
w^{1118}; UAS-BLD10::GFP;+	[6]	

Table S2: List of antibodies used in this study.

Name	References	Comments
Anti-Acetylated α-tubulin	[5]	Dilution used 1:500
Anti- Glutamylated tubulin	[22]	Dilution used 1:500
Anti-PLP (pericentrin-like protein)	[23]	Dilution used 1:500
Anti-SPD2	[13]	Dilution used 1:500
Anti-γ-tubulin	[13]	Dilution used 1:50
Anti-Ana2	this study	Dilution used 1:250

Anti-SAS6	[13]	Dilution used 1:250
Anti-BLD10	[24]	Dilution used 1:2000
Anti-22c10	[25]	Dilution used 1:50
Anti-Rootletin	[26]	Dilution used 1:100
Anti-GFP	[27]	Dilution used 1:100 (for STED)

Table S3: Description of the genotypes of the flies that were used in this study.

Genotype of the fly	**Abbreviated Name**	**Used in the Figure**
w^{1118}; Endo-Rootletin::GFP	Rootletin (in neurons)	Figure 1A & B
w^{1118}; Endo-Rootletin::GFP;Ubq-RFP::PACT	Rootletin (in sperm cells)	Figure 1C & D
w^{1118}; Endo-Ana1::GFP;+	Ana1 (in neurons)	Figure 2A & B
w^{1118}; Endo-BLD10::GFP;+	BLD10 (in neurons)	Figure 2A & B
w^{1118}; Endo-SAS4::GFP;+	SAS4 (in neurons)	Figure 2A & B
w^{1118}; Endo-SAS6::GFP;+	SAS6 (in neurons)	Figure 2A & B
w^{1118}; Endo-Ana1::GFP; Ubq-RFP::PACT	Ana1 (in sperm cells)	Figure 2C & D
w^{1118}; Endo-BLD10::GFP; Ubq-RFP::PACT	BLD10 (in sperm cells)	Figure 2C & D
w^{1118}; Endo-SAS4::GFP; Ubq-RFP::PACT	SAS4 (in sperm cells)	Figure 2C & D
w^{1118}; Endo-SAS6::GFP; Ubq-RFP::PACT	SAS6 (in sperm cells)	Figure 2C & D
w^{1118}; Endo-UNC::GFP;+	UNC (in neurons)	Figure 3A & B
w^{1118}; Endo-Chibby::GFP;+	Chibby (in neurons)	Figure 3A & B
w^{1118}; Endo-MKS1::GFP;+	MKS1 (in neurons)	Figure 3A & B
w^{1118}; Endo-B9D1::GFP;+	B9D1 (in neurons)	Figure 3A & B
w^{1118}; Endo-CEP290::GFP;+	CEP290 (in neurons)	Figure 3A & B
w^{1118}; Endo-UNC::GFP; Ubq-RFP::PACT	UNC (in sperm cells)	Figure 3C & D
w^{1118}; Endo-Chibby::GFP; Ubq-RFP::PACT	Chibby (in sperm cells)	Figure 3C & D
w^{1118}; Endo-MKS1::GFP; Ubq-RFP::PACT	MKS1 (in sperm cells)	Figure 3C & D
w^{1118}; Endo-B9D1::GFP; Ubq-RFP::PACT	B9D1 (in sperm cells)	Figure 3C & D
w^{1118}; Endo-CEP290::GFP; Ubq-RFP::PACT	CEP290 (in sperm cells)	Figure 3C & D

w^{1118}; +; $Cep290^{mecH}$	$Cep290^{mutant}$	Figure 4 & S8
w^{1118}; +/+; $neur^{Gal4}$/ UAS-mCherryRNAi	$control^{2}$	Figure S8A-D
w^{1118}; UAS-CEP290RNAi/+; $neur^{Gal4}$/+	$CEP290RNAI^{1}$	Figure 4 & S8A-D
w^{1118}; $hsp83^{Gal4}$/UAS-CEP290RNAi;+	$CEP290RNAi^{2}$	Figure 4 & S8E
w^{1118}; $cha19b^{Gal4}$/ UASp-CEP290::GFP;+	CEP290::GFP	Figure 4A, D & S7A
w^{1118}; $cha19b^{Gal4}$/+; UASp-GFP::CEP290/+	GFP::CEP290	Figure 4A, D & S7A, C
w^{1118}; $hsp83^{Gal4}$/ UASp-CEP290::GFP;+	CEP290::GFP	Figure 4G
w^{1118}; $hsp83^{Gal4}$/+; UASp-GFP::CEP290/+	GFP::CEP290	Figure 4G & S7C
w^{1118}; Endo-SAS6::GFP; Ubq-RFP::PACT		Figure 5A, 6A
w^{1118}; +; +	$control^{1}$	Figure 4-6, & S1-11
w^{1118}; +; CG15524 ^{c02901}/Df	$SAS6^{mutant}$	Figure 5B, 6C & S10
w^{1118}; $cha19b^{Gal4}$/+; UAS-mCherryRNAi/+	$control^{4}$	Figure 5B & S10B
w^{1118}; $cha19b^{Gal4}$/+; UAS-SAS6RNAi/+	$SAS6RNAi^{1}$	Figure 5B & S10B
w^{1118}; Ubq-SAS6::GFP	SAS6::GFP	Figure 6B
w^{1118}; bam^{Gal4}/+; UAS-mCherryRNAi/+	$control^{5}$	Figure S11
w^{1118}; bam^{Gal4}/+; UAS-SAS6RNAi/+	$SAS6RNAi^{2}$	Figure S11
w^{1118}; $hsp83^{Gal4}$/+; UAS-mCherryRNAi/+	$control^{3}$	Figure 6C & S9, 11
w^{1118}; $hsp83^{Gal4}$/+; UAS-SAS6RNAi/+	$SAS6RNAi^{3}$	Figure 6C, S11
w^{1118}; $hsp83^{Gal4}$/UAS-ANA2RNAi;+	$Ana2RNAi^{1}$	Figure 6C, S11
w^{1118}; $hsp83^{Gal4}$/UAS-BLD10RNAi;+	$BLD10RNAi^{1}$	Figure 6C, S11
w^{1118}; $hsp83^{Gal4}$/ Ubq-RFP::PACT; UAS-mCherryRNAi/UAS-mCD8::GFP	$Control\ 1^{CEP290}$	Figure S9A
w^{1118}; $hsp83^{Gal4}$/ UAS-CEP290RNAi; Ubq-RFP::PACT/UAS-mCD8::GFP	$Knock\ down^{CEP290}$	Figure S9A
w^{1118}; $hsp83^{Gal4}$/ UAS-CEP290RNAi; Ubq-RFP::PACT/UAS-CEP290::GFP	$rescue^{CEP290}$	Figure S9A
w^{1118}; $hsp83^{Gal4}$/ Ubq-RFP::PACT; UAS-mCherryRNAi/UAS-CEP290::GFP	$Control\ 2^{CEP290\ (OE)}$	Figure S9A
w^{1118}; $hsp83^{Gal4}$/ UAS-mCD8::GFP; UAS-mCherryRNAi/ Ubq-RFP::PACT	$Control\ 1^{SAS6}$	Figure S9B
w^{1118}; $hsp83^{Gal4}$/ UAS-mCD8::GFP; UAS-SAS6RNAi/Ubq-RFP::PACT	$Knock\ down^{SAS6}$	Figure S9B
w^{1118}; $hsp83^{Gal4}$/ UAS-SAS6::GFP; UAS-SAS6RNAi/Ubq-RFP::PACT	$Rescue^{SAS6}$	Figure S9B

w^{1118}; $hsp83^{Gal4}$/ UAS-SAS6::GFP; UAS-mCherryRNAi/ Ubq-RFP::PACT	Control $2^{SAS6\ (OE)}$	Figure S9B
w^{1118}; $hsp83^{Gal4}$/ Ubq-RFP::PACT; UAS-mCherryRNAi/UAS-Mcd8::GFP	Control 1^{ANA2}	Figure S9C
w^{1118}; $hsp83^{Gal4}$/ Ubq-RFP::PACT; UAS-ANA2RNAi/UAS- mCD8::GFP	Knock $down^{ANA2}$	Figure S9C
w^{1118}; $hsp83^{Gal4}$/ Ubq-RFP::PACT; UAS-ANA2RNAi/UAS-ANA2::GFP	$Rescue^{ANA2}$	Figure S9C
w^{1118}; $hsp83^{Gal4}$/ Ubq-RFP::PACT; UAS-mCherryRNAi/UAS-ANA2::GFP	Control $2^{ANA2\ (OE)}$	Figure S9C
w^{1118}; $hsp83^{Gal4}$/ UAS-mCD8::GFP; UAS-mCherryRNAi/ Ubq-RFP::PACT	Control 1^{BLD10}	Figure S9D
w^{1118}; $hsp83^{Gal4}$/ UAS-mCD8::GFP; UAS-BLD10RNAi/Ubq-RFP::PACT	Knock $down^{BLD10}$	Figure S9D
w^{1118}; $hsp83^{Gal4}$/ UAS-BLD10::GFP; UAS-BLD10RNAi/Ubq-RFP::PACT	$Rescue^{BLD10}$	Figure S9D
w^{1118}; $hsp83^{Gal4}$/ UAS-BLD10::GFP; UAS-mCherryRNAi/ Ubq-RFP::PACT	Control $2^{BLD10\ (OE)}$	Figure S9D
w^{1118}; +/+; Ubq-RFP::PACT /+	Ectopic expression (-, -)	Figure 7 & S12A-C
w^{1118}; Ubq-SAS6::GFP /+; Ubq-RFP::PACT /+	Ectopic expression (+, -)	Figure 7 & S12A, C
w^{1118}; Ubq- GFP::ANA2 /CyO; Ubq-RFP::PACT /+	Ectopic expression (-, +)	Figure 7 & S12A, C
w^{1118}; Ubq- GFP::ANA2 / Ubq-SAS6::GFP; Ubq-RFP::PACT /+	Ectopic expression (+, +)	Figure 7 & S12A-C
w^{1118}; Ubq-RFP::PACT /+; $neur^{Gal4}$/+	Ectopic expression (-, -)	Figure S12D
w^{1118}; Ubq-RFP::PACT / UAS-SAS6::GFP; $neur^{Gal4}$/ UAS- GFP::ANA2	Ectopic expression (+, +)	Figure S12D
w^{1118}; $cha19b^{Gal4}$/+; Ubq-RFP::PACT /+	Ectopic expression (-, -)	Figure S13
w^{1118}; $cha19b^{Gal4}$/ UAS-SAS6::GFP; Ubq-RFP::PACT /+	Ectopic expression (+, -)	Figure S13
w^{1118}; $cha19b^{Gal4}$/+; Ubq-RFP::PACT / UAS-GFP::ANA2	Ectopic expression (-, +)	Figure S13
w^{1118}; $cha19b^{Gal4}$/ UAS-SAS6::GFP; Ubq-RFP::PACT / UAS- GFP::ANA2	Ectopic expression (+, +)	Figure S13

1

References for Supplemental Information:

1. Jana, S.C., Mendonca, S., Werner, S. & Bettencourt-Dias, M. Methods to Study Centrosomes and Cilia in Drosophila. *Methods in molecular biology* **1454**, 215-236 (2016).
2. Vieillard, J., Duteyrat, J.L., Cortier, E. & Durand, B. Imaging cilia in Drosophila melanogaster. *Methods Cell Biol* **127**, 279-302 (2015).
3. Albert, J.T. & Gopfert, M.C. Hearing in Drosophila. *Curr Opin Neurobiol* **34**, 79-85 (2015).
4. Enjolras, C. *et al.* Drosophila chibby is required for basal body formation and ciliogenesis but not for Wg signaling. *J Cell Biol* **197**, 313-325 (2012).
5. Jana, S.C., Girotra, M. & Ray, K. Heterotrimeric kinesin-II is necessary and sufficient to promote different stepwise assembly of morphologically distinct bipartite cilia in Drosophila antenna. *Mol Biol Cell* **22**, 769-781 (2011).
6. Carvalho-Santos, Z. *et al.* BLD10/CEP135 is a microtubule-associated protein that controls the formation of the flagellum central microtubule pair. *Dev Cell* **23**, 412-424 (2012).
7. Mastronarde, D.N. Dual-axis tomography: an approach with alignment methods that preserve resolution. *Journal of structural biology* **120**, 343-352 (1997).
8. Martinez-Campos, M., Basto, R., Baker, J., Kernan, M. & Raff, J.W. The Drosophila pericentrin-like protein is essential for cilia/flagella function, but appears to be dispensable for mitosis. *J Cell Biol* **165**, 673-683 (2004).
9. Laurencon, A. *et al.* Identification of novel regulatory factor X (RFX) target genes by comparative genomics in Drosophila species. *Genome biology* **8**, R195 (2007).
10. Blachon, S. *et al.* A proximal centriole-like structure is present in Drosophila spermatids and can serve as a model to study centriole duplication. *Genetics* **182**, 133-144 (2009).
11. Baker, J.D., Adhikarakunnathu, S. & Kernan, M.J. Mechanosensory-defective, male-sterile unc mutants identify a novel basal body protein required for ciliogenesis in Drosophila. *Development* **131**, 3411-3422 (2004).
12. Basiri, M.L. *et al.* A migrating ciliary gate compartmentalizes the site of axoneme assembly in Drosophila spermatids. *Curr Biol* **24**, 2622-2631 (2014).
13. Rodrigues-Martins, A. *et al.* DSAS-6 organizes a tube-like centriole precursor, and its absence suggests modularity in centriole assembly. *Curr Biol* **17**, 1465-1472 (2007).
14. Thibault, S.T. *et al.* A complementary transposon tool kit for Drosophila melanogaster using P and piggyBac. *Nat Genet* **36**, 283-287 (2004).

15. Jhaveri, D., Sen, A., Reddy, G.V. & Rodrigues, V. Sense organ identity in the Drosophila antenna is specified by the expression of the proneural gene atonal. *Mechanisms of development* **99**, 101-111 (2000).
16. Salvaterra, P.M. & Kitamoto, T. Drosophila cholinergic neurons and processes visualized with Gal4/UAS-GFP. *Brain research. Gene expression patterns* **1**, 73-82 (2001).
17. Arama, E., Agapite, J. & Steller, H. Caspase activity and a specific cytochrome C are required for sperm differentiation in Drosophila. *Dev Cell* **4**, 687-697 (2003).
18. Chen, D. & McKearin, D.M. A discrete transcriptional silencer in the bam gene determines asymmetric division of the Drosophila germline stem cell. *Development* **130**, 1159-1170 (2003).
19. Dietzl, G. *et al.* A genome-wide transgenic RNAi library for conditional gene inactivation in Drosophila. *Nature* **448**, 151-156 (2007).
20. Pfeiffer, B.D. *et al.* Refinement of tools for targeted gene expression in Drosophila. *Genetics* **186**, 735-755 (2010).
21. Stevens, N.R., Roque, H. & Raff, J.W. DSas-6 and Ana2 coassemble into tubules to promote centriole duplication and engagement. *Dev Cell* **19**, 913-919 (2010).
22. Bobinnec, Y., Marcaillou, C. & Debec, A. Microtubule polyglutamylation in Drosophila melanogaster brain and testis. *European journal of cell biology* **78**, 671-674 (1999).
23. Fu, J. & Glover, D.M. Structured illumination of the interface between centriole and peri-centriolar material. *Open Biol* **2**, 120104 (2012).
24. Mottier-Pavie, V. & Megraw, T.L. Drosophila bld10 is a centriolar protein that regulates centriole, basal body, and motile cilium assembly. *Mol Biol Cell* **20**, 2605-2614 (2009).
25. Hummel, T., Krukkert, K., Roos, J., Davis, G. & Klambt, C. Drosophila Futsch/22C10 is a MAP1B-like protein required for dendritic and axonal development. *Neuron* **26**, 357-370 (2000).
26. Chen, J.V. *et al.* Rootletin organizes the ciliary rootlet to achieve neuron sensory function in Drosophila. *J Cell Biol* **211**, 435-453 (2015).
27. Luo, W. & Sehgal, A. Regulation of circadian behavioral output via a MicroRNA-JAK/STAT circuit. *Cell* **148**, 765-779 (2012).